DEUTSCHES ELEKTRONEN-SYNCHROTRON
Ein Forschungszentrum der Helmholtz-Gemeinschaft

DESY-THESIS-2017-046
December 2017

Micro-Channel Cooling for Silicon Detectors

by

N.Flaschel

ISSN 1435-8085

NOTKESTRASSE 85 - 22607 HAMBURG

DESY	DESY
Zentralbibliothek	Bibliothek
Notkestrae 85	Platanenallee 6
22607 Hamburg	15738 Zeuthen
Germany	Germany

Micro-channel Cooling For Silicon Detectors

Dissertation

zur Erlangung des Doktorgrades
an der Fakultät für Mathematik,
Informatik und Naturwissenschaften
Fachbereich Physik
der Universität Hamburg
vorgelegt von

Nils Flaschel

DESY / Hamburg University

Hamburg

2017

Gutachter/in der Dissertation:	Dr. Kerstin Tackmann
	Prof. Dr. Caren Hagner
	Dr. Ingrid-Maria Gregor

Datum der Disputation: 7.11.2017

Aus dieser Dissertation hervorgegangene Veröffentlichungen: (Publications resulting from this thesis:)

"Thermal and hydrodynamic studies for micro-channel cooling for large area silicon sensors in high energy physics experiments", N. Flaschel, D. Ariza , S. Díez, I.-M. Gregor, K. Tackmann, M. Gerboles, X. Jorda, R. Mas, D. Quirion, M. Ullan, *Nuclear Instruments and Methods in Physics Research, Section A: Accelerators, Spectrometers, Detectors and Associated Equipment*, vol. 863:26-34, (2017), https://doi.org/10.1016/j.nima.2017.05.003

Eidesstattliche Erklärung

Hiermit erkläre ich an Eides statt, dass ich die vorliegende Dissertationsschrift selbst verfasst und keine anderen als die angegebenen Quellen und Hilfsmittel benutzt habe. Die eingereichte schriftliche Fassung entspricht der auf dem elektronischen Speichermedium. Die Dissertation wurde in der vorgelegten oder einer ähnlichen Form nicht schon einmal in einem früheren Promotionsverfahren angenommen oder als ungenügend beurteilt.

Nils Flaschel Hamburg, 7.8.2017

Declaration on oath

I hereby declare, on oath, that I have written the present dissertation by my own and have not used other than the acknowledged resources and aids.

Nils Flaschel Hamburg, 7.8.2017

Abstract

Silicon tracking detectors employed in high-energy physics are located very close to the interaction points of the colliding particle beams. The high energetic radiation emerging from the interaction induces defects into the silicon, downgrading the efficiency to collect the charges created by passing particles and increasing the noise while data taking. Cooling the sensors to low temperatures can help to prevent defects and maintain a high efficiency and lower noise level.

In order to maximize the LHC's discovery potential, the collider and its detectors will be upgraded to a higher luminosity around 2024. The conditions inside the detector will become harsher demanding that the technology must adapt to the new situation.

Radiation damage is already an issue in the current ATLAS detector and therefore a huge number of parameters are constantly monitored and evaluated to ensure optimal operation. To provide the best possible settings the behavior of the sensors inside the ATLAS Inner Detector is predicted using simulations. In this work several parameters in the simulation including the depletion voltage and the crosstalk between sensor strips of the SCT detector are analyzed and compared with data.

The main part of this work concerns the investigation of a novel cooling system based on micro-channels etched into silicon in a generic research and development project at DESY and IMB-CNM. A channel layout is designed providing a homogeneous flow distribution across a large surface area and tested in a computational fluid simulation before its production. Two different fabrication techniques, anodic and eutectic bonding, are used to test prototypes with differing mechanical and thermal properties. Hydromechanical and thermal measurements are performed to fully characterize the flow inside the device and the thermal properties of the prototype in air and in a vacuum. The thermal behavior is analyzed by means of local measurements with thermal resistors and infrared cameras. A test facility is developed and constructed in order to realize the measurements. The results of the simulations and the experimentally gained results are compared and contrasted.

Zusammenfassung

in der Hochenergiephysik verwendete Silizium-Spurendetektoren befinden sich üblicherweise sehr nah am Kollisionspunkt der Teilchenstrahlen. Die Wechselwirkung mit der entstehenden hochenergetischen Strahlung führt zu Defekte im Silizium. Diese führen zu einer Verminderung der Fähigkeit durch passierende Teilchen entstandene Ladungsträger zu sammeln und auSSerdem zu einem Anstieg des Rauschens während der Datennahme. Das Kühlen der Sensoren auf niedrige Temperaturen kann der Defektbildung entgegenwirken und zum Erhalt der Effizienz und zu einem niedrigen Rauschpegel führen.
Um das Entdeckungspotential des LHC zu maximieren, werden der Beschleuniger und dessen Detektoren gegen 2024 für eine höhere Luminosität aufgerüstet. Die Gegebenheiten im Detektor werden noch drastischer und bedürfen einer Anpassung der Technologie an die neuen Umstände.
Strahlenschäden sind bereits im aktuellen ATLAS Detektor ein ernstes Problem, weshalb eine groSSe Zahl von Parametern kontinuierlich beobachtet werden, um einen optimalen Betrieb zu gewährleisten. Das Verhalten der Sensoren im ATLAS Inner Detector werden mit Simulationen prognostiziert. In dieser Arbeit werden wichtige Parameter wie die Depletion Spannung und der Crosstalk zwischen Sensorstrips des SCT Detektors analysiert und mit Daten verglichen.
Der Hauptteil der vorliegenden Arbeit behandelt die Untersuchung eines neuartigen Kühlungssystems basierend auf in Silizium geätzte Mikrokanäle in einem generischen Forschungs-, und Entwicklungsprojekt am DESY und am IMB-CNM. Ein Mikrokanaldesign, das eine homogene Flüssigkeitsverteilung über eine groSSe Fläche bietet wird erstellt und in einer Fluidsimulation getestet bevor ein Prototyp produziert wird. Zwei verschiedene Produktionsweisen, Anodic und Eutectic Bonding werden zur Herstellung verwendet, um Prototypen mit verschiedenen mechanischen und thermischen Eigenschaften zu untersuchen. Hydrodynamische und thermische Messungen werden durchgeführt, um die Strömung durch die Struktur und die thermischen Eigenschaften des Prototypen vollständig zu charakterisieren. Die thermischen Messungen werden mit temperaturempfindlichen Widerständen und Infrarotkameras durchgeführt. Ein Teststand wird entwickelt und aufgebaut, um die Messungen durchzuführen. AnschlieSSend werden die Ergebnisse der Simulation und die des Experiments miteinander verglichen.

Contents

Chapter 1

Introduction

The development and manufacture of electronic components has grown to be one of the most significant global industries. Today, requirements on the dimensions of integrated circuits are pushing the limits of manufacturing further and further. At the same time the resulting power densities are increasing, providing a new challenge to the cooling systems.

In most particle physics detectors silicon sensors are used to observe the trajectory of passing particles. The emerging high energetic radiation downgrades the efficiency of the sensor to collect charges created by passing particles, due to defects induced into the silicon. The shot noise also increases during data taking due to increased leakage currents. In silicon sensors and high performance processors the feedback loop between temperature and leakage current can lead to a thermal runaway. Moreover, the electronics to read out the sensor and process the data are usually attached to the sensors and the heat flow coming from the electronics influences the sensor performance. This can be avoided or restricted by cooling the sensor.

The efficiency of the cooling system must be optimized to cope with the decreasing critical temperature at which thermal runaway appears due to radiation damage caused by the vast amount of high energetic particles passing through the silicon. Down-scaling of cooling pipes shows a highly beneficial behavior due to the increased surface to volume ratio.

The first cooling of electronics via micro-channel flows was accomplished in 1981 by Tuckerman and Pease [1]. Many approaches were pursued to understand and improve the mass flow and the heat transfer through micro-channel devices. The technology has been utilized in many different fields with various requirements on the dimensions, the coolant or the channel layout.

It is necessary to give a general motivation for technological research and development, to justify the presented work. Large and cost intensive experiments like the Large Hadron Collider (LHC) must constantly push the technological boundaries to realize their ambition. The planned upgrade of the LHC and its detectors represents a major challenge in terms of innovative technology. Costs can be reduced by developing new methods and materials outside everyday use and at the same time collaborating and networking between different fields of science and various groups in the same field can be enhanced.

The presented work transfers micro-channel cooling to high energy physics (HEP) applications as part of a generic research and development project. As the work was carried out in the ATLAS group the requirements on the cooling of a silicon sensor for the ATLAS upgrade for the High Luminosity LHC were used as the baseline. In the past few years micro-channel cooling has gained more and more attention in HEP, and a number of experiments have started investigating and using it. In particular, the opportunity to embed the channels into silicon offers a big advantage. Sensors in the innermost parts of HEP detectors are mostly based on silicon and are used to measure charged particle trajectories. The effect of thermal noise and the leakage currents induced by radiation damage have to be suppressed by cooling the sensor to very low temperatures. At the same time, mechanical stress due to different coefficients of thermal expansion (CTE) between the sensor and other detector parts have to be reduced as much as possible.
This is where micro-channel cooling comes into play. The cooling system can be integrated directly into the active sensor, easing the restrictions for the surrounding material regarding thermal characteristics of the mechanical structure. As shown by other groups, it holds the potential to save material [2], cool small [3] and large areas [2] and can be operated with singlephase [2] and multiphase coolants [4].
This work presents a proof of concept of developing and testing a large area micro-channel embedded heat sink based on a 4 inch silicon wafer by DESY and IMB-CNM with the additional requirement of a homogeneous cooling across the actively cooled wafer surface. To accomplish that, a pilot plant was built to perform hydrodynamic and thermal studies of the device in air and in a vacuum. After first computational fluid dynamics (CFD) simulations, a channel design providing a homogeneous flow distribution was specified. The prototype was produced in various different forms at IMB-CNM.
A hydrodynamic and thermal characterization of the prototype was carried out and in parallel, most tests were reproduced in a simulation. The results are compared with those of the experiment, including a detailed description of the simulation environment and properties.

This introduction is followed by a chapter about the Standard Model (SM) which is the underlying theory in experimental particle physics. The fundamentals of the physics and theory behind it are covered, as well as the motivation for the construction of large scale experiments. Semiconductor sensors and silicon detectors are described in chapter 3, and their impact and relevance to the LHC and ATLAS in chapter 4 and chapter 5, respectively. The upgrade plans for the High-Luminosity LHC (HL-LHC) are covered in chapter 6.
Chapter 7 covers the work on the ATLAS simulation, where the effect of charge trapping in the silicon sensors of the Semiconductor Tracker and the crosstalk between the strips responsible for collecting the charge is investigated.
This is followed by the basics of fluid dynamics and heat transfer in chapter 8 as an introduction to the channel layout design and prototype production described in chapter 9, the simulated and

experimentally obtained results of the micro-channel prototype tests are described in chapter 10 and chapter 11, respectively.

Chapter 2

Standard Model of particle physics and beyond

Over centuries of striving to understand the functional principle at the scale of elementary particles, numerous particles and interactions were gathered during the search and summarized in a gauge quantum field theory called the Standard Model (SM). The SM [5] [6] [7] describes the elementary particles, the fundamental interactions - the weak, the strong and the electromagnetic - and the Higgs mechanism. Combining quantum mechanics, electromagnetism and special relativity led to the first successful description of the electromagnetic interaction in a quantum field theory - treating the particles as exited states of an underlying quantized field - and laid the foundations of the SM.
The SM as a field theory is built up on the product of the U(1) symmetry for the electromagnetic interactions, a SU(2) symmetry for the weak interaction and a SU(3) symmetry for the strong interaction. The product U(1)×SU(2)×SU(3) is the underlying symmetry group of the SM, and is broken by the Higgs mechanism explained at a later point in this chapter.

The interactions are arising by exchanging spin-one gauge bosons between spin-half fermions, which are divided into quarks and leptons. Every fermion also has an anti-fermion associated with it with the same mass but opposite signs for its electric charge.
An overview of the particles of the SM is shown in figure 2.1. There are four gauge bosons acting as force carriers. The interaction mediated by the gluon is the strong interaction and the particles - the quarks - coupling to the gluon carry a color charge like the gluon. The $W^{\pm}$ and the Z^0 are the bosons associated with the weak interaction, and all fermions are interacting via the weak force. The photon mediates the electromagnetic force and interacts with all fermions and the $W^{\pm}$ but not with the neutrinos. At energies above 100 GeV the weak and the electromagnetic force can be unified into the electroweak interaction. The Higgs boson is the excitation of the Higgs field - proposed by François Englert, Peter Higgs and Robert Brout [9] [10]. The field is responsible for the mass of particles in the SM. Finally in 2012 the ATLAS and CMS collaborations announced the discovery of a new particle, which behaves as the Higgs boson in the SM within the present experimental un-

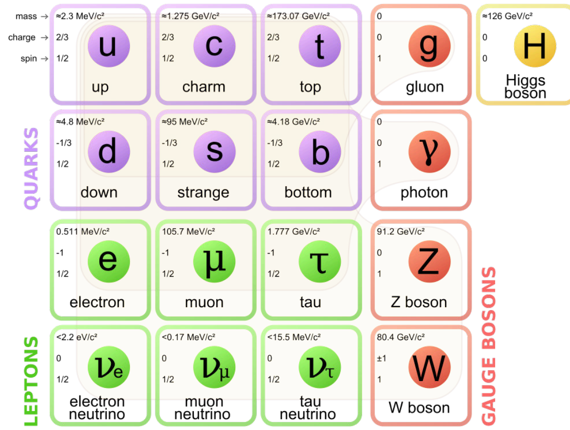

Figure 2.1: Table of Standard Model particles: 12 fundamental fermions and 4 fundamental bosons [8].

Table 2.1: Table of the basic properties of the leptons [8].

Lepton	Mass	Mean lifetime	Electric charge
e^-	0.51 MeV	4.6×10^{26} yr	-1 e
μ^-	105.66 MeV	2.197×10^{-6} s	-1 e
τ^-	1776.82 MeV	2.903×10^{-17} s	-1 e

certainties. The forth force is the gravitation, whose supposed mediator, the graviton, has not been discovered yet.

The listed particles are assumed to make up the largest fraction of visible matter of our universe. In the following, each group, the quarks, the leptons, the gauge bosons and the Higgs boson are treated in more detail. Furthermore, this chapter will outline the basics of the dynamic theories, quantum electrodynamics, quantum chromodynamics, the weak interactions and conclude with a section about the motivation to look for physics beyond the SM.

2.1 Leptons

There are six leptons, divided into three generations: the electron e and electron neutrino ν_e, the muon μ and muon neutrino ν_μ and the tauon τ and tau neutrino ν_τ. Table 2.1 shows the basic properties, the mass, mean lifetime and electric charge of the electron, the muon and the tau of which only the electron and its antiparticle, the positron, are stable. Leptons and antileptons can only be created or annihilated in pairs of the same flavor which is known as the *conservation of lepton number* in the SM.

There is good evidence that the SM is not complete. In the SM the neutrinos are massless, but neutrino measurements show an oscillation, which indicates a finite neutrino mass. Oscillation

Table 2.2: The masses of the u, d, s and b quarks are given in a short distance scheme at a scale of $\mu \approx 2$ GeV. The c and b quark masses are running masses and the t quark mass comes from direct measurements in the minimal subtraction scheme [8].

Quark	Mass	Electric charge
Up u	2.3 MeV	$2/3\ e$
Down d	4.8 MeV	$-1/3\ e$
Charmed c	1.3 GeV	$2/3\ e$
Strange s	95 MeV	$-1/3\ e$
Top t	173.2 GeV	$2/3\ e$
Bottom b	4.18 GeV	$-1/3\ e$

means that the neutrinos can change their flavor, for example from ν_e to ν_μ. Evidences came for example from measurements of neutrinos from the sun and the analysis of the cosmic microwave background (CMB).

2.2 Quarks and bound quarks

There are six quarks in three generations, the up quark u and down quark d, the charm quark c and strange quark s, and the top quark t and bottom quark b. The quark type is also referred to as flavor. Their main features, the electric charge and the mass, are presented in table 2.2. The flavor of the quark can change through the weak interaction.

However, all quarks appear in compound states like in the form of a proton or a neutron. This is due to the fact that the coupling of the strong force is increasing at larger distances, leading to the confinement of quarks and gluons within hadrons. States of quark-antiquark pairs are mesons and state of three bound quarks are baryons both being hadrons, of which only the proton is stable.

Cross section measurements revealed a discrepancy between the observed

$$R = \frac{\sigma(e^+e^- \to \text{strongly interacting particles})}{\sigma(e^+e^- \to \mu^+\mu^-)} \tag{2.1}$$

and its naively expected value. The naively expected ratio of the cross section of e^+e^- decaying to strongly interacting particles and the cross section of e^+e^- to $\mu^+\mu^-$ was by a factor 3 too small [7]. To resolve this problem, a color charge was ascribed to every flavor. With three different color states R = 11/3 is in perfect agreement with the observations.

2.3 Gauge bosons

The gluon g, which mediates the strong interaction, the photon γ mediating the electromagnetic interaction and the W and Z bosons mediating the weak force are the four gauge bosons in the SM. The strength stated in terms of coupling strength of the forces is very different in nature and range [11].

2.4 Higgs boson

In addition to the gauge bosons and the fermions the Higgs boson is part of the Standard Model and was discovered only recently (2012) at the LHC with a mass of around 125 GeV [12]. The underlying Brout-Englert-Higgs mechanism describes a spontaneous $\mathrm{U}(1)_Y \times \mathrm{S}(1)_L$ gauge symmetry breaking by a two component scalar-field. This mechanism with its nonzero ground state in vacuum accounts for the masses of the Z and W boson as well as for the mass of the leptons and quarks. The production cross sections and decay branching fractions of the Higgs boson are predicted as a function of its mass, which can be measured. Measurements of both ATLAS and CMS show the compatibility with the Higgs boson predicted by the SM within the present uncertainties [13].

2.5 Interaction in the SM

2.5.1 Quantum electrodynamics

Quantum electrodynamics (QED) is a quantized theory and was used as skeleton for the quantization of the other dynamic theories. All processes in QED are based on one elementary process shown in figure 2.2, namely any charged fermion emitting or absorbing a photon. Every process in QED can be expressed as a combination of that primitive process [6]. Processes in QED can have a higher order. With each order a number of additional possibilities has to be taken into account. Due to the fact that higher orders of the process contribute less and less, properties can be calculated using perturbation theory.

Quantum electrodynamics has a coupling constant associated with it. Despite its name, the coupling constant is not constant but is changing with the distance between the interacting particles or the energy scale of the process. The strength of the coupling in QED is influenced by charge screening, which is the mechanism of virtual loops of e^+e^- pairs screening the charge at larger distances. Hence, the coupling decreases with decreasing distances.

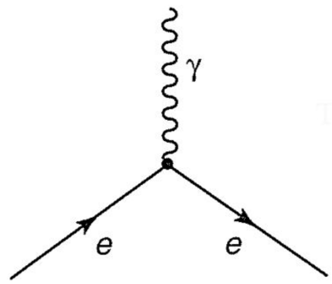

Figure 2.2: Fundamental process in QED. A charged particle emits (or absorbs) a photon [6].

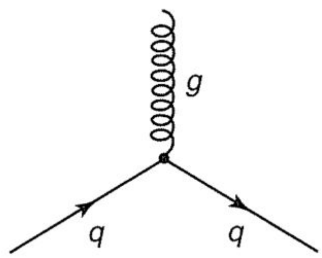

Figure 2.3: One fundamental process in QCD. A quark emits (or absorbs) a gluon [6].

2.5.2 Quantum chromodynamics

Instead of electric charge, quantum chromodynamics (QCD) uses the concept of a color charge. One of the elementary processes in QCD involves a gluon instead of a photon. Figure 2.3 shows the process of a quark emitting a gluon [6].

The concept of a color charge for each quark in addition to an electric charge represents a big difference to QED. The gluon carries color too - actually color and anticolor - and therefore couples to itself. The number of additional possibilities due to three different color charges makes QCD a lot more complicated to calculate than QED. The additional primitive vertices are shown in figure 2.4.

In QCD the process of charge screening causing a change of the coupling constant is influenced

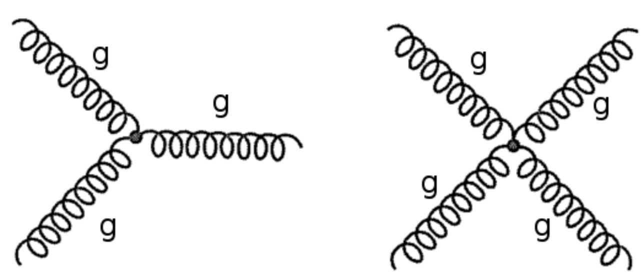

Figure 2.4: Additional fundamental processes in QCD. Direct gluon-gluon couplings [6].

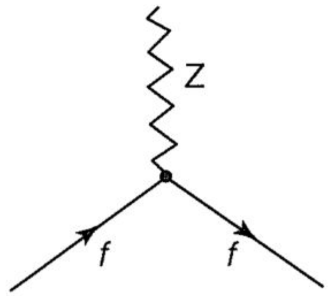

Figure 2.5: Fundamental process in neutral weak interactions. Any lepton f emits a Z [6].

by the gluon-gluon loops. The dependence of the coupling on the distance between the interacting particles changes to the opposite. It gets larger at smaller distances.
This different behavior of the coupling constants increases the complexity of QCD. With a bigger coupling constant, processes with more vertices have to be taken into account and the usually used perturbation theory to add the corrections in form of a small perturbation of the system can not be applied anymore [6].
Many different resonances from exited proton and neutron states appear in photon-nucleon and pion-nucleon scattering. The concept of isospin was introduced to strongly-interacting particles to classify hadron states of light quarks (u and d quark).

2.5.3 Weak interaction

All leptons and quarks interact via the weak interaction, which can be divided in two kinds: the charged weak interaction, mediated by the $W^{\pm}$ bosons and the neutral weak interaction, mediated by the Z boson. Again there is a fundamental process for each of the two interactions.
Every neutral current interaction is a version or a combination of versions of the one shown in figure 2.5 [6], where f can be any lepton or quark. Hence, electron scattering can also happen with a Z boson exchange instead of exchanging a photon. This behavior was indeed confirmed through collision experiments ($e^+ \, e^- \rightarrow \mu^+ \, \mu^-$) at DESY in Hamburg, and therefore the Coulomb law had to be slightly corrected due to the Z boson contribution shown in figure 2.6 [7].

Charged weak interactions differ from QED, QCD and neutral weak processes. It is the only interaction where the particle changes the flavor. The fundamental process involving leptons is shown in figure 2.7, where any charged lepton converts into the corresponding neutrino by emitting (absorbing) a W^- (W^+).
The fundamental process involving quarks looks the same as with leptons, converting a quark into another quark without changing the color. A quark with charge -1/3 (d,s or b) converts into a corresponding quark with charge +2/3 (u,c or t). The process is shown in figure 2.8 and can be combined with the process shown in figure 2.7 to describe for example the beta decay ($n \rightarrow p^+$ + e^- + $\bar{\nu}_e$).

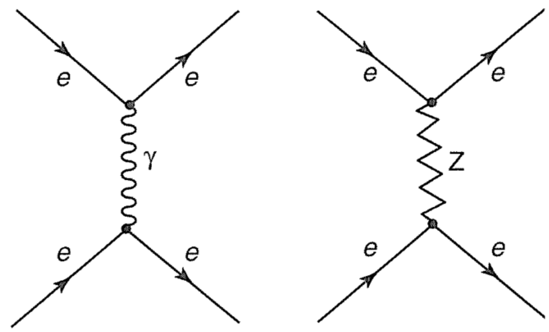

Figure 2.6: The photon and Z contribution in electron scattering processes [6].

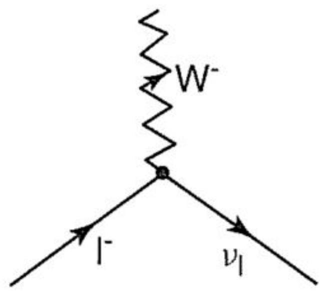

Figure 2.7: Fundamental process in charged weak interactions involving leptons [6].

Like the gluon-gluon coupling in QCD the W boson can couple to itself and the charged W boson also to the photon.
A lepton coming in can change via a weak interaction and only into a lepton of the same generation, with an exception due to neutrino oscillations, which happens on a much larger length scale.

Although the SM is extremely well tested and its description of the behavior of particles match the observed one very well [8], there are open questions which can not be answered by the theory.

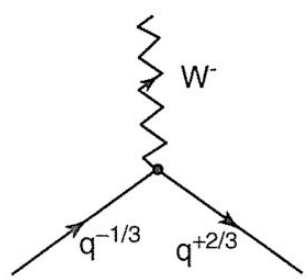

Figure 2.8: Fundamental process in charged weak interactions involving quarks. A quark (d,s or b) converts to a corresponding quark (u,c or t) [6].

2.6 Beyond the standard model

The goal of ongoing and future particle collider experiments is to further test the SM with more precise measurements, and to discover possible new physics beyond the SM.
A difference from the expected rotation velocity of galaxies was observed already around 1933 and led to the assumption that a different form of matter is present in a much larger amount than luminous baryonic matter. Today the dark matter is estimated to make up around 25% of our universe. In addition, the discovery that the expansion rate of the universe is actually accelerating instead of slowing down led to the theory of dark energy which is supposed to make up around 69% of our universe [5].
Nowadays, evidences for the existence of dark energy are coming from CMB measurements. An additional electrically neutral form of matter had to be present in large amounts to explain the fast formation of gravitational wells needed to form galaxies and other structures. The particles assumed as candidates for dark matter are usually referred to as weakly interacting massive particles (WIMPs) [14].

Another phenomenon indicating physics beyond the SM is the matter antimatter asymmetry in the observable universe. Although the amount of matter and antimatter is assumed to be the same after the big bang, there is almost no antimatter present today.
Because no significant number of antimatter was observed, and the final states of the annihilation of matter and antimatter are mainly photons, the asymmetry is given by the ratio between the number of baryons and photons. The ratio can for example be measured by analyzing the fluctuations in the CMB, which were caused by oscillations in the baryon-photon plasma [15].

Chapter 3

Introduction to semiconductor sensors

The investigation of nuclear physics, elementary particle physics, astro particle physics and the interactions between particles need detectors. For many experiments measuring the trajectory of the particle is essential. Important parameters can be deduced like the charge, the origin of the particle or the momentum if the detector is placed in a magnetic field. These tracking detectors are often made of silicon and are very thin to absorb only a fraction of the particle's energy. To understand why silicon is used for this specific purpose in detectors and what processes occur in the silicon crystal this section will give the theoretical background [16].

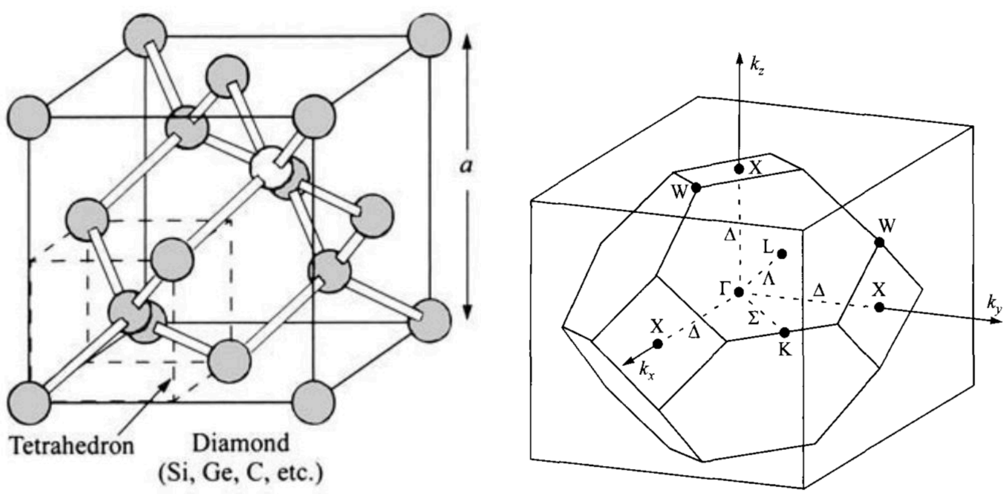

(a) Primitive cell of the diamond lattice (b) Wigner-Seitz cell of the reciprocal diamond lattice

Figure 3.1: The primitive cell of silicon with the lattice constant a shown in figure a) and the Wigner-Seitz cell (first Brillouin zone) of the reciprocal lattice shown in figure b).

3.1 Crystal structure of silicon

Silicon is a crystal with a diamond lattice (shown in figure 3.1 a), where the primitive cell describes the fundamental cell with the lattice constant a, which is repeated throughout the solid. The lattice of a crystal is treated in terms of its reciprocal structure and the primitive cell in the reciprocal lattice is called Wigner-Seitz cell or first Brillouin zone, as shown in figure 3.1 b). This illustration is primarily useful for calculations including the wave vector k, which is related to the momentum of the electrons in the lattice.
Silicon as a semiconductor is characterized by its conductivity or rather its resistance. These properties depend on the band structure of the material.
Theoretical studies of semiconductors showed the existence of forbidden energy ranges in which energy bands can not exist. The bands below this forbidden gap are the valence bands, and the bands above the gap are the conduction bands. The separation between the highest valence band and the lowest conduction band is the bandgap and denoted as E_g. This quantity is one of the most

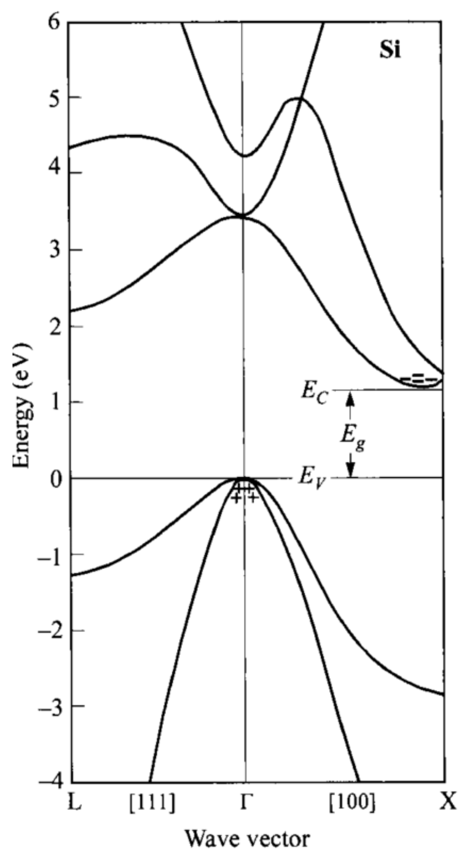

Figure 3.2: The band structure of silicon along the high symmetry points in the Brillouin zone with E_g the bandgap and -, + representing electrons and holes in the conduction and valence band. The minimum of the lowest conduction band and the maximum of the highest valence band are not vertically aligned, forming an indirect gap.

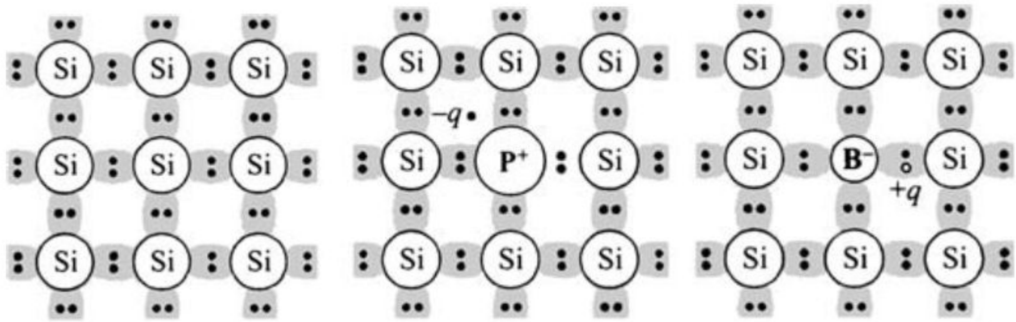

(a) No impurities (b) n-type with donors (c) p-type with acceptors

Figure 3.3: Representation of the bonds between the silicon atoms of the crystal lattice. Silicon without impurities in a), silicon with a phosphor atom as electron donor b) and silicon with a boron impurity as electron acceptor c).

important properties of a semiconductor.
The band structure of silicon is shown in figure 3.2 with - or + signs representing the electrons and the holes in the conduction and valence bands. The bandgap of silicon is $E_g = 1.14\,\mathrm{eV}$ at room temperature and decreasing with increasing temperature.
A charge carrier in the semiconductor has a lifetime which depends on the probability of recombination. The recombination process describes a carrier jumping from the conduction band to the valence band by emitting a photon or passing the energy to another free carrier, but it is also possible that the carrier is recombined non-radiatively in a bulk trap. A trap represents a local anomaly in the energy gap, which can lead to a recombination.

3.2 Doping silicon and the pn-junction

A way to change the resistance of a semiconductor is by replacing atoms in the crystal lattice by other atoms with different properties like more or fewer valence electrons, which is referred to as doping. The doping concentration directly affects the space charge in the semiconductor.
Figure 3.3 shows a representation of the bonds between the silicon atoms of the crystal lattice. The four electrons of a silicon atom are equally shared with the other lattice members in impurity free silicon (figure 3.3 a). When an atom with more valence electrons than silicon is placed in the lattice (figure 3.3 b), a free electron is donated to the conduction band of the lattice and the silicon is called n-type. A p-type silicon has substitutionary atoms with fewer electrons than silicon and a hole is created in the valence band of the silicon lattice. The number of donors or acceptors is directly affecting the Fermi energy level E_F representing the highest level of occupied states at 0 K.
The occupancy of the conduction band at an energy (E) can be described by the Fermi-Dirac distri-

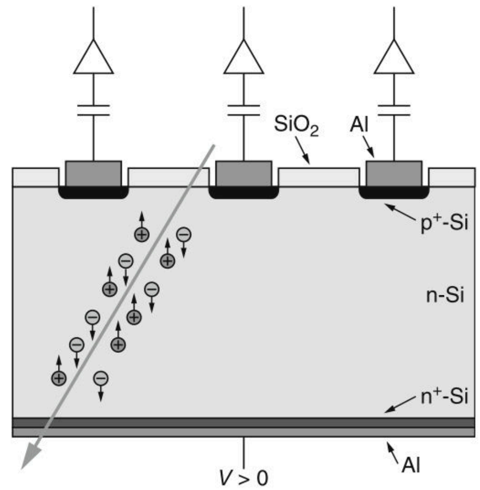

Figure 3.4: Scheme of a p in n silicon strip detector. An ionizing particle creates free charge carriers, which drift to the Aluminum electrodes.

bution

$$F(E) = \frac{1}{1 + \exp(\frac{E - E_F}{kT})}. \tag{3.1}$$

The number of free charge carriers in a typical intrinsic silicon sensor in high energy physics is by many orders of magnitudes higher than the free charge carriers produced by an minimal ionizing particle passing through ($\approx 4.3 \cdot 10^8$ $e^- h^+$-pairs compared to $\approx 3.2 \cdot 10^4$ $e^- h^+$-pairs).
In order to create a region with less free charge carriers pn-junctions are used. When a p-type region and a n-type region are brought into contact electrons move to the lower Fermi levels and holes to the higher. At the border of the pn-junction combination and diffusion of the charge carriers creat a space charge layer and an electric field preventing further diffusion, so that the diffusion flow and the field current are compensating each other. This effect suppresses the leakage current in the sensor formed by electron-hole creation in the electric field.
When in addition a bias voltage is applied to the doped semiconductor the concentration of electrons and holes can be increased above their equilibrium value. The depth which becomes carrier free depends on the field strength and the applied voltage. The voltage needed to stretch the carrier free region across the full sensor thickness is referred to as the depletion voltage V_d.

3.3 Principles of silicon sensors

When a charged particle with enough energy passes through a semiconducting material it creates pairs of electrons and holes, known as impact ionization. This is the fundamental process used in semiconductor sensors utilized in particle detectors. The charges of the electrons or holes are then collected at an anode or cathode and processed as a signal. The number of charge carriers

arriving at the corresponding electrode depends on the concentration of traps induced by radiation and the resulting decrease in free carriers. This property is reflected in the measurement of the charge collection efficiency of a sensor.
In order to measure the location of an impact ionization the sensor is segmented in one or more dimensions. So called strip detectors are segmented in one dimension with parallel electrode strips along the sensor. Figure 3.4 shows the scheme of a p in n strip detector as a cut through the sensor vertical to the strips. In the presented case the electrodes (strips and backplane) are made of Aluminum. Pixel sensors are segmented in two dimensions into blocks which are connected to electronic chips.
Every signal from a semiconductor device is affected by noise, which can be separated in thermal noise, flicker noise and shot noise. The noise in general is a fluctuation of the current which is used as signal. Thermal noise appears due to the random thermal motion of the carriers in the lattice, flicker noise is caused by surface effects and shot noise by the discreteness of the carriers.

3.4 Radiation damage

Radiation is causing two different kinds of defects in the sensor, bulk damage and surface damage. The first one represents the main problem for the sensors and the latter one is more problematic for the electronics.
Bulk damages in silicon are mainly caused by displacing a primary knock on atom (PKA) out of the crystal lattice. The PKA as well as the cavity can migrate through the material and form point defects with impurity atoms already present in the silicon. Depending on the energy of the recoiled PKA it causes numerous further displacements and ionizations along its path forming a PKA cascade with clusters of defects at the end of each PKA path.
The bulk defects induced to the silicon have three main effects, depending on their depth in the band structure. Firstly, the effective doping concentration can changes due to charged defects contributing to the space charge. As a consequence the depletion voltage will increase and can exceed the limit for a save sensor operation. This happens when the defect is located away from the Fermi energy. Secondly, due to radiation induced traps in the silicon a part of the free charge carriers produced by ionizing particles will not be collected at the electrodes and lead to an decreased signal size, which happens when the defect is located inside the bandgap but not too close to the Fermi energy. Lastly, the effect of generation and recombination of free charge carriers increases the noise level due to increased leakage currents. At the same time the leakage currents cause a heating of the sensor. Higher temperatures introduce higher currents and are increasing the power dissipation and thus again the temperature. This mechanism is leading to an effect called thermal runaway. It is avoided by cooling the sensor and the critical temperature at which thermal runaway happens decreases with irradiation of the sensor. This occurs when the defect is located close to the Fermi energy.
The scale of the energy loss due to atomic displacements by particles passing through the silicon is

described by the Non Ionizing Energy Loss (NIEL) hypothesis [17]. The bulk damages are assumed to scale linearly with the energy deposited in the material due to displacements. The radiation level is usually given in the unit 1 MeV equivalent neutrons (n_{eq}) per m^2

Another effect caused by irradiation over a longer time is the type inversion, which is a space charge sign turnaround, transforming a n-type section into a p-type section. By exposing the sensor to a higher temperature the level of defects can be decreased due to the mobility of the defects at certain temperatures, which is called annealing.

Chapter 4

LHC

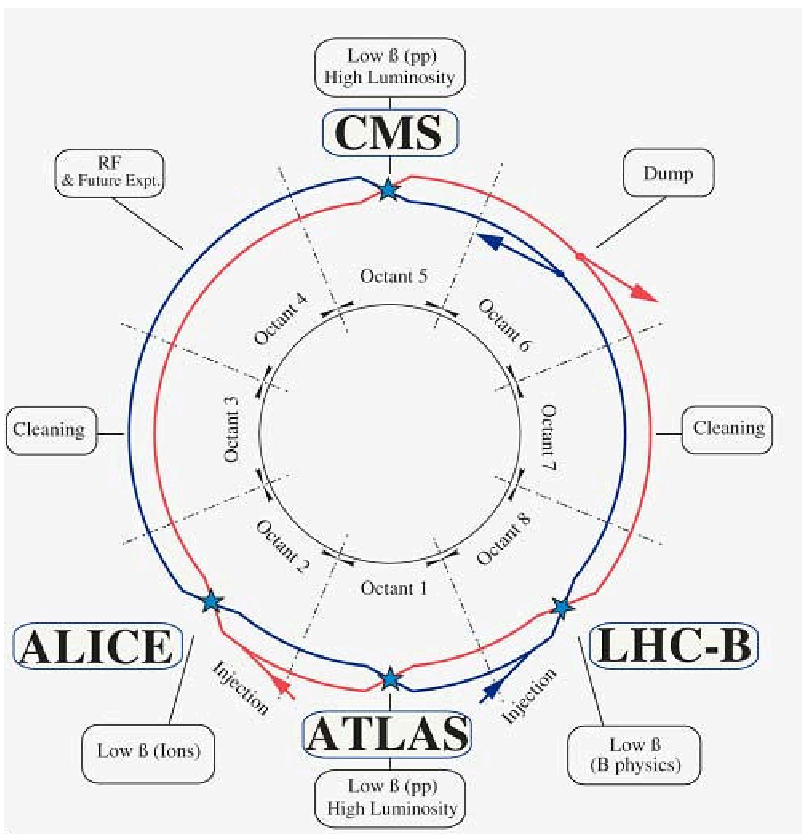

Figure 4.1: Scheme of the LHC main ring with the two beams passing four experiments (taken from [18]).

The Large Hadron Collider [18] [19] (LHC) is a two-ring particle accelerator and collider located at CERN and was put into operation in 2009. The colliding particles are mainly protons, but the operation mode can be switched to heavy ions. It is located about 100 m underground and is build into the former Large Electron Positron Collider (LEP) tunnel with a circumference of 26.7 km. The

ring contains eight straight sections, of which four are equipped with particle physics experiments. The time of operating the LHC was accompanied by shutdowns for maintenance of the collider. Each period of continuous operation is called a run. The LHC reached a center-of-mass energy of 13 TeV during run 2 in 2016 after starting run 1 with 900 GeV in 2009 and reaching 8 TeV at the end of run 1 in 2013. A scheme of the LHC main ring can be seen in figure 4.1
The counter-rotating beams are brought together at four locations to form interaction points. Two of these interaction points are occupied by the general purpose detectors ATLAS and CMS. A third one is occupied by LHCb, an experiment specialized on CP violation and rare decays of b hadrons. The fourth experiment is called ALICE and is dedicated to the measurement of ion-ion collisions.
The beam consist of so called bunches, which are dense particle packages. The high particle density of the accelerated bunches ensure a high collision probability at the interaction points. Strong magnets are used to guide the bunches along the circular tracks and to keep their form.

4.1 Luminosity

The LHC reached its center-of-mass energy goal of 13 TeV and its design luminosity of $1 \times 10^{34}\,\mathrm{cm^{-2}\,s^{-1}}$ in 2016. The luminosity [12] is given by

$$L = \frac{N_1 N_2 n_b f_{rev}}{2\pi\sqrt{\sigma_{1x}^2\sigma_{2x}^2}\sqrt{\sigma_{1y}^2\sigma_{2y}^2}} \cdot F \cdot W \tag{4.1}$$

where N_1 and N_2 are the number of particles per bunch for each beam, n_b the number of colliding bunches, f_{rev} the revolution frequency, σ the beam width of the two beams (1 and 2) in x (pointing to the LHC center) and y (pointing up) and F and W the geometric luminosity reduction factor due to the crossing angle and the transverse offset at the interaction point.
The peak luminosity desired by ATLAS and CMS of L = $1 \times 10^{34}\,\mathrm{cm^{-2}\,s^{-1}}$ was reached in the beginning of 2016. At the peak center-of-mass energy and design luminosity of the LHC, this results in about 23 events per crossing - or pile-up - and an estimated integrated luminosity of $300\,\mathrm{fb^{-1}}$ at around 2020 for ATLAS and CMS [18].

4.2 Injection chain

To fill the LHC ring with protons, a chain of various acceleration and optimization steps must be passed on the way. The linear accelerator Linac2 is the initial step to accelerate the protons. From there they are passed to the Proton Synchrotron Booster (PSB), further to the Proton Synchrotron (PS) and then to the Super Proton Synchrotron (SPS). All three, PSB, PS and PSP, are machines that existed beforehand and had to be optimized in terms of magnetic power, Radio Frequency (RF) systems and beam profile measurement devices and cryogenic systems. An especially challenging

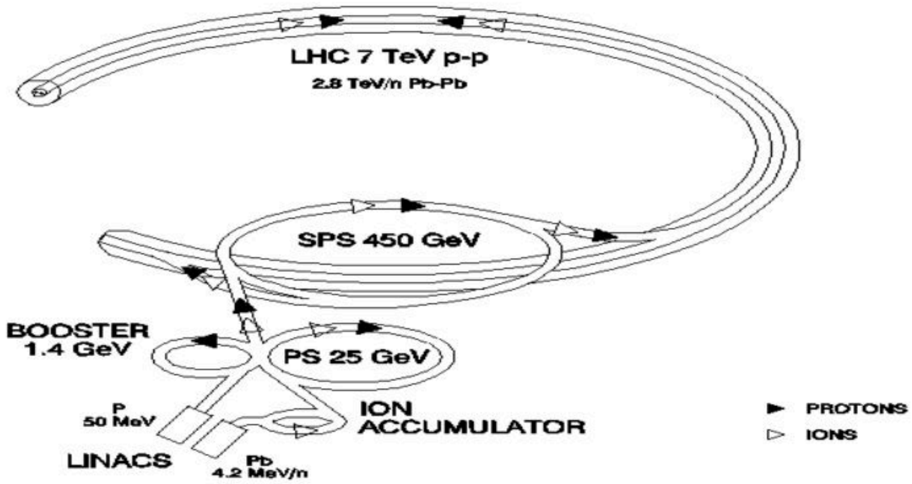

Figure 4.2: Scheme of the LHC injection chain (taken from [18]).

part of the chain are the different requirements on the beam properties at injection points and at interaction points (IP). While the longitudinal emittance - the emittance of the beam describes how confined it is - has to be small at injection points, it has to be large at interaction points to avoid inter-beam collisions, which are collisions of particles inside the bunches [18]. A scheme of the injection steps can be seen in figure 4.2.

Chapter 5

ATLAS detector

The ATLAS [20] [21] [22] (A Toroidal LHC ApparatuS) detector is one of two multipurpose detectors at the LHC. It is built to master measurements at a final center-of-mass energy of 14 TeV and a design luminosity of $1 \times 10^{34}\,\mathrm{cm}^{-2}\,\mathrm{s}^{-1}$.
In the following, a general overview of the detector is provided and subsequently, every sub-detector will be discussed in more detail.

5.1 Overall detector concept

The ATLAS detector has a cylindrical shape, is 46 m long, measures about 25 m in diameter, weighs approximately 7000 kg and consists of three main detector sections: the inner detector (ID), the calorimeters and the muon spectrometer.
Most sub-detectors are subdivided into a barrel and a number of endcaps, expanding the coverage of the barrel alone, and providing more hits per particle track than an extended barrel alone would provide. The coverage of the detector describes the ability of measuring particles with a small angle with respect to the beam pipe, and a hit represents a signal in a sensor from the energy deposited by a particle flying through.
The coordinate system (see figure 5.1) to describe positions and directions in the detector has the IP as origin. The beam pipe represents the z-axis, the x-axis points to the LHC center and the y-axis points up, perpendicular to the beampipe. In polar coordinates the azimuthal angle Φ is measured from the x-axis around the beam pipe and the polar angle Θ is measured from the positive z-axis. An alternative definition of the polar angle is the pseudo rapidity

$$\eta = -\ln \tan(\frac{\Theta}{2}), \tag{5.1}$$

representing a massless approximation of the rapidity [12].
The Inner Detector (ID) is based on silicon sensors (Pixel and SCT, see section 5.2) and a transition

tracking detector (TRT) based on drift tubes responsible for the tracking of charged particles coming from the interaction point. The ID is embedded into an axial solenoidal magnetic field (section 5.3) causing a bending of the particle trajectory to measure the particles' momenta. The silicon tracking section is surrounded by the calorimeters (section 5.4). They are responsible for the energy and position measurements of electrons, photons and hadrons. The muon detector (section 5.5) makes up the outermost part to detect the momentum of high energy muons escaping from the calorimeters. Toroid magnets in the barrel and endcaps of the muon spectrometer ensure a sufficient bending of the muon trajectories.
Furthermore the trigger system used to filter the events is described in section 5.7.

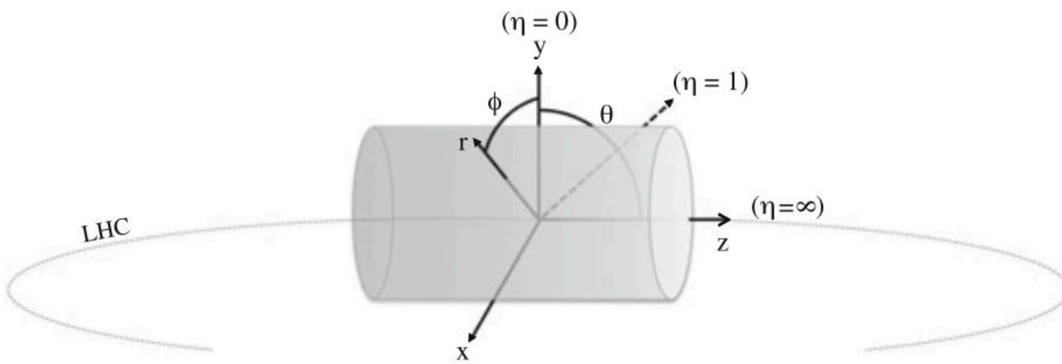

Figure 5.1: The coordinate system used by all LHC experiments, in Cartesian and cylindrical coordinates including the pseudo rapidity η and the polar angle Θ [12].

5.2 Inner Detector

The inner tracking system is designed to measure all charged particles emerging from the interaction point with a transverse momentum above $\approx 1\,\text{GeV}$ and over the range $|\eta| < 2.5$. Figure 5.2 shows a 2D view of a cut through a quarter of the ID to give an overview of the detector layers along η. Figure 5.3 shows a 3D scheme of the ID for a better spatial impression of the three subdetectors, the Pixel Detector, the SemiConductor Tracker (SCT) and the Transition Radiation Tracker (TRT).
Radiation hardness is one of the most crucial technical requirements of the detector since the radiation is strong due to the proximity to the primary interactions. Cooling also becomes very important due to the power consumption of the high-speed-front-end electronics. The ID has to fulfill a number of tight requirements from the performance point of view. It must be able to measure impacts of particles at high spatial precision to reconstruct their trajectories. The energy clusters of detected particles in the calorimeter must be matched with the reconstructed track momenta from the ID to identify the particles.
In the following, the three different sections of the ID mentioned earlier are discussed in more detail starting from the beampipe to the outside.

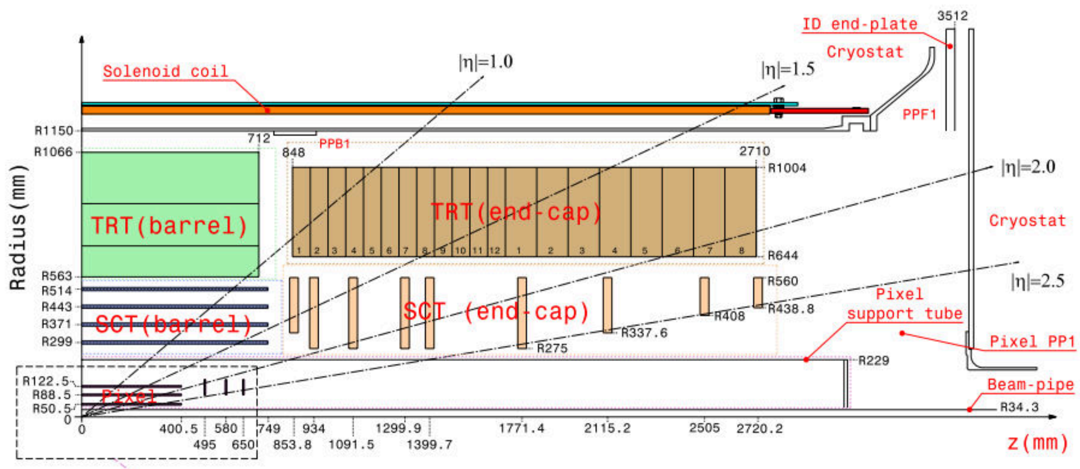

Figure 5.2: View of a quarter-section of the ATLAS inner detector during run 1, showing the major detector elements Pixel Detector, SCT and the TRT. [23].

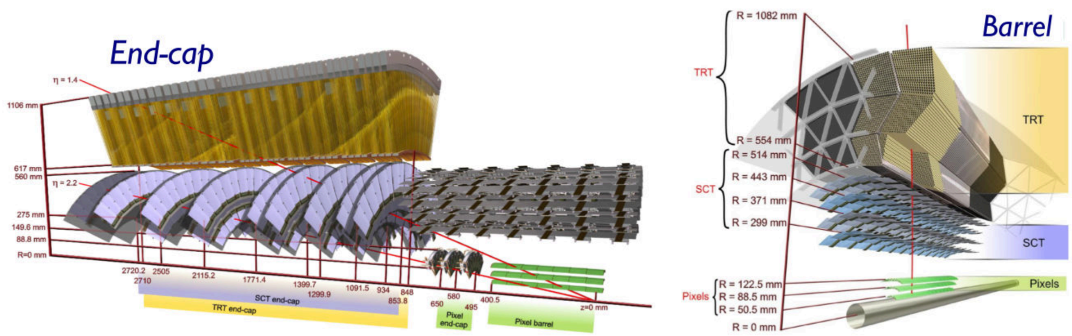

Figure 5.3: 3D view of the inner detector endcap and barrel section during run 1. [24].

5.2.1 Pixel detector

The Pixel Detector [25] is the part of the whole detector which is closest to the interaction point as shown in figure 5.3. It is important for pattern recognition and contributes to the ability of finding secondary vertices. It consists of four barrel layers in which the insertable B-layer (IBL) - with closest distance to the beam pipe - was inserted during a shutdown between run 1 and run 2 in 2013/2014. The Pixel Detector incorporates an active sensor area of 1.7 m^2. Three additional disk layers are located at each end of the barrel forming the endcap for a greater coverage.

The Pixel Detector is separated into modules, which consist of the 300 μm thick silicon pixel sensors and the read-out electronics. There are over 2000 modules in the four Pixel Detector barrel layers and endcap discs [26]. The pixel sensors are $n+$ on n silicon sensors permitting to operate in partially depleted mode in order to limit leakage currents. The outer three pixel layers are equipped with sensors with a pitch of 50 μm $\times$ 400 μm with the larger side pointing in the Φ-direction. The IBL sensors have a slightly smaller pitch of 50 μm $\times$ 250 μm [27].

The Pixel Detector readout architecture consists of the sixteen frontend (FE) Chips, a Module Controller Chip (MCC) and two optochips as main components. The FE chips amplify and digitize

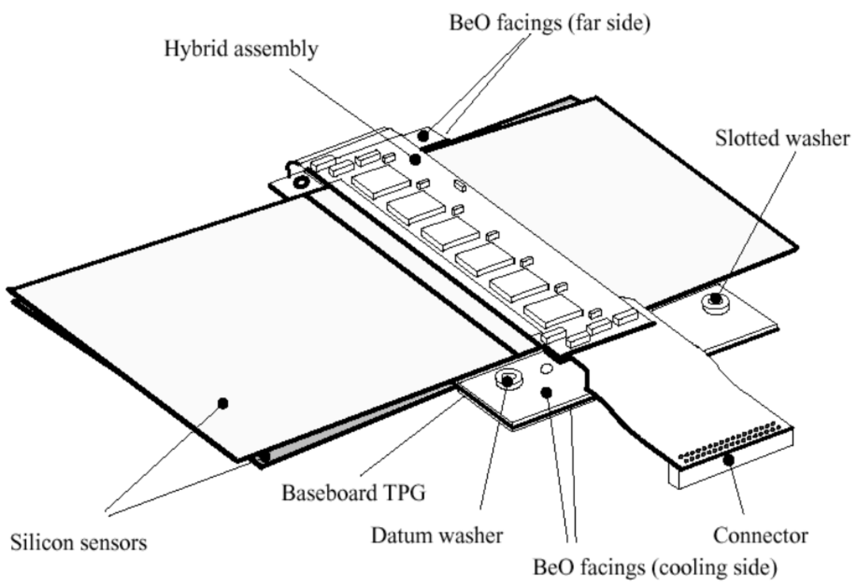

Figure 5.4: View of a SCT barrel module. The Beryllium oxide facings of the modules are connected to heat sinks, which are aluminium blocks with Cu/Ni cooling pipes [28].

the signal and buffer it during the trigger system latency time. The MCC handles the configuration of the FE Chips, the event building and the trigger signal. The trigger signal and MCC command decoding and signal transfer is provided by the two optochips.
The support structures in the barrel (staves) and in the disks (petals) are holding the modules in place, and have an integrated cooling structure to keep the silicon at low temperatures. The cooling system of the IBL differs in type from the rest of the Pixel Detector. Instead of using the evaporative C_3F_8 as in the rest of the ID, it is equipped with an evaporative CO_2 cooling system [27].

5.2.2 SemiConductor Tracker

The ATLAS SemiConductor Tracker (SCT) barrel [28] surrounds the pixel detector with radii from 299 mm to 514 mm and a length of 1429 mm as shown in figure 5.3. Each of the four layers is providing a two dimensional measurement of a particle hit position. The SCT endcaps [29] are located on each side of the barrel consisting of nine disks to cover $-2.5 < |\eta| < 2.5$.
The barrel is build to measure particles coming from an expected $\pm$ 76 mm around the nominal IP along the z-axis. Each barrel cylinder is equipped with modules equipped with four microstrip sensors and read-out electronics - two sensors on the front and two on the back side of the module. A total of over 2000 modules are installed, equipped with p in n microstrip sensors made of <111> oriented silicon. Each sensor has 768 strips to collect the charge produced by traversing particles. Figure 5.4 shows a SCT barrel module with a length in z-direction of 149 mm.
The baseboard represents the core of the module handling the thermal management, mechanical integrity and precision attachment to the barrel structure. The module is cooled down by connecting

one side (marked with 'cooling side' in figure 5.4) of the baseboard to an aluminum block acting a heat sink equipped with a cooling pipe running evaporated C_3F_8. The connection is realized with a Beryllium oxide (BeO) facing due its high thermal conductivity.
Twelve readout chips are mounted on each module, six on each hybrid across one sensor, each being capable of handling 128 strips with a binary readout. A hybrid is a Kapton board holding the readout chips and controller chips. The two sensors on the front (pointing towards the beampipe) are mounted with a 40 mrad angle with respect to the two sensors on the back of the module to provide a stereo measurement.

In order to prevent thermal runaway the SCT barrel modules have to be kept at an average sensor temperature of about −7 °C during data taking [30]. Finite element analysis (FEA) methods were used, to develop the design of the module and to predict the temperature distribution along the module. The maximum temperature of the module during operation is at the readout electronics on the hybrid with 5.7 °C and the maximum temperature of the sensors is about −4 °C [30]. A heat flux of 120 μW mm^{-2} is estimated for the 285 µm thick sensor after ten years of operation, giving a security margin of a factor of 2.3 before thermal runaway sets in.
The main mass contribution of 44 % to the module weighing 25 g comes from the silicon sensors. In total the material of the SCT barrel detector is about $\approx$ 3% X_0 per layer, including the module services, like the cooling system and cables, as main contribution [30]. The radiation length X_0 defines the amount of matter traversed to reduce the energy of a high energetic electron to $1/e$ by bremsstrahlung and the mean free path to 2/9 due to e^-e^+ pair production, which represent the two dominant ways of an high energetic electron losing energy in matter.
The initial bias voltage is around 150 V and the same for all barrel layers, whereas the configuration will change during the operation of ATLAS due to different radiation doses in each layer. Considering a factor of two larger irradiation for the first SCT layer than for the outermost SCT barrel layer, the bias voltage is estimated to reach $\approx$ 450 V for the first layer and $\approx$ 250 V for the outermost layer with a 90% charge collection efficiency after 10 years of operation [30].
Endcaps are installed at each ends of the SCT barrel. Each of the two endcaps consist of 9 disks with a diameter around 1.2 m and equipped with three rings of modules of which two (smallest and biggest radii) are on the front side and one ring with an intermediate radius is located on the other side. The modules installed in the endcaps partly overlap to avoid the gaps in the acceptance. The same evaporative C_3F_8 cooling system is used as in the barrel.
The inner ring modules are the only ones with just one sensor on each side due to the shorter module length. Due to the geometry of the petals, five different sensor shapes are used depending on their distance to the beam pipe. The target temperature of the silicon is −7 °C as in the barrel, which is maintained by using a support structure with very high thermal conductivity. That way, an estimated maximum heat of 6 W generated per module can be evacuated [29].

5.2.3 Transition radiation tracker

The Transition Radiation Tracker (TRT) is a drift tube detector covering the range $|\eta| < 2$ and is shown in figure 5.3. It is based on polyimide tubes filled with a gas mixture and a gold-plated tungsten sense wire. The tubes are surrounded by a radiator in a gas mixture to provide particle identification [31]. The tubes in the barrel are up to 150 cm long with a diameter of 4 mm. The TRT contains a total of 300000 straws in the barrel and the two endcaps. In order to reduce the occupancy, the straws in the barrel oriented in direction of the beampipe are separated in the center. The tube walls are kept at a negative voltage, so that primary electrons are directed towards the sense wire, which acts as an anode. [31]. Polypropylene fibres with a diameter of 19 µm (barrel) or thin polypropylene radiator foils (endcap) are placed between every straw layer to use the effect of transition radiation. When a charged particle passes an inhomogeneous medium with different dielectric constants, the particle emits electromagnetic radiation. Two thresholds are set in the readout of the TRT, a low threshold (LT) and a high threshold (HT). The photons emerging from the electron passing the scintillator material between the straws have a higher energy and produce a signal above the HT. The fraction of HT hits on a track can be used to distinguish between electrons and charged pions. The TRT provides a spatial resolution of around 130 µm [31].

5.3 Solenoid and toroid

In order to measure the momentum of high energetic charged particles in the range of 1 TeV, their trajectories are bent with the help of a magnetic field. A superconducting technology was chosen for the ID to operate a high magnetic field. A small-radius thin-walled 2 T solenoid was integrated into the cryostat of the barrel electromagnetic calorimeter, which is located right behind the TRT in the y-direction. In order to provide high-accuracy measurements the magnetic field has to be known at a nanometer precision, not only due to its effect on the particles but also due to its influence on the mechanical detector structure.

A separate magnet for the high precision measurements of the muon momentum is integrated in the muon spectrometer, the outermost detector layer. Three air-core toroids [22], one in the barrel and two in the endcaps, are responsible for the magnetic field in the muon spectrometer. The toroid installed in the barrel consists of eight separate magnets with a bending power of 1.5 T m to 5.5 T m in the range $|\eta| < 1.4$. The two magnet systems in the endcaps have a bending power of 1.5 T m to 7.5 T m in $1.6 < |\eta| < 2.7$.

5.4 Calorimeter

Calorimeters are designed to measure the energy a particle loses while traversing the material. Usually a calorimeter aims at completely absorbing energy of the particle. Surrounding the ATLAS ID

and the solenoid the calorimeter [20] [22] aims at identifying photons and electrons escaping the tracking detector, as well as sampling the energy of passing hadrons. The calorimeter is fragmented in a Liquid Argon (LAr) Calorimeter and a Tile Hadronic Calorimeter.
The design and technical requirements of the calorimeter was heavily influenced by the fact that it is located behind the solenoid magnet. This results in a significant energy loss of particles passing the detector, where approximately half the material from the center to the calorimeter is located due to the massive solenoid magnet. In the following the two different calorimeter systems are presented.

5.4.1 Electromagnetic liquid argon calorimeter

The Electromagnetic (EM) Calorimeter is a lead-liquid argon sampling detector separated into cells with its own readout electronics. The barrel covers $|\eta| < 1.475$ [32] and the endcaps $1.375 < |\eta| < 3.2$ [33]. Additionally, the endcaps contain copper-liquid argon hadronic sampling calorimeter wheels discussed in section 5.4.2 [34].
The barrel is divided in two equally long sections along the beam line, with a small gap at $z = 0$, whereas the two endcaps are divided into an inner and an outer section. Both regions - barrel and endcaps - are also segmented in z. The barrel consists of three layers in direction perpendicular to the beamline, of which the first one is a presampling layer. The endcaps inner-wheels are segmented in two sections having coarser granularity than the barrel layers and include also a presampling layer. The presampling layers are additional layers to correct for the energy loss of electrons and photons going through the solenoid.
The dynamic range should cover energies from 30 MeV - which is the typical noise level of a single EM calorimeter cell - to over 1 TeV, which is an expected single cell deposit for heavy gauge boson decays [32].

5.4.2 Hadronic liquid argon calorimeter

Due to the robustness against high radiations in the forward region, liquid argon was chosen as the active material. The absorbing layers are made of copper. Each endcap is segmented in two wheels with increasing copper plate thicknesses to fully absorb high energetic particle showers. To reconstruct the two jets emerging from a W decay, the transverse granularity is $\Delta\eta\times\Delta\phi = 0.1\times0.1$ for $|\eta| < 2.5$ and $\Delta\eta \times \Delta\phi = 0.2 \times 0.2$ in the $|\eta|$ region larger than 2.5.

5.4.3 Liquid argon forward calorimeter

The Forward Calorimeter (FCal) [35] is located between the electromagnetic and hadronic LAr calorimeter endcaps and the beam pipe utilizing LAr as active material and copper and tungsten as absorbing material, as shown in figure 5.5. The calorimeter covers a region with high radiation doses and high energy particle impacts in the range of $3.1 < |\eta| < 4.9$. It is segmented in three parts, with the first segment used as an electromagnetic FCal and followed by two hadronic FCal parts.

5.4.4 Hadronic tile calorimeter

The Hadronic Tile Calorimeter [36] (TileCal) is a sampling calorimeter covering $|\eta| < 1.7$ and it consist of three barrel sections surrounding the entire LAr calorimeter. Steel plates acting as absorbent are equipped with scintillator tiles as sensitive parts. The scintillator tiles are read out via fibres, transporting the scintillator light to photomultiplier tubes. The mechanical structure ranges from an inner diameter of 4576 mm to an outer diameter of 8460 mm with a module length of 5640 mm in the barrel and 2900 mm in the extended barrel.
The TileCal has the role of measuring the energy and position of electrons, photons, τ-leptons and jets. A maximum geometrical coverage ensures the indirect detection of missing energy due to neutrinos. Furthermore, it contains enough absorber material to fully capture hadronic showers from the p-p interactions.

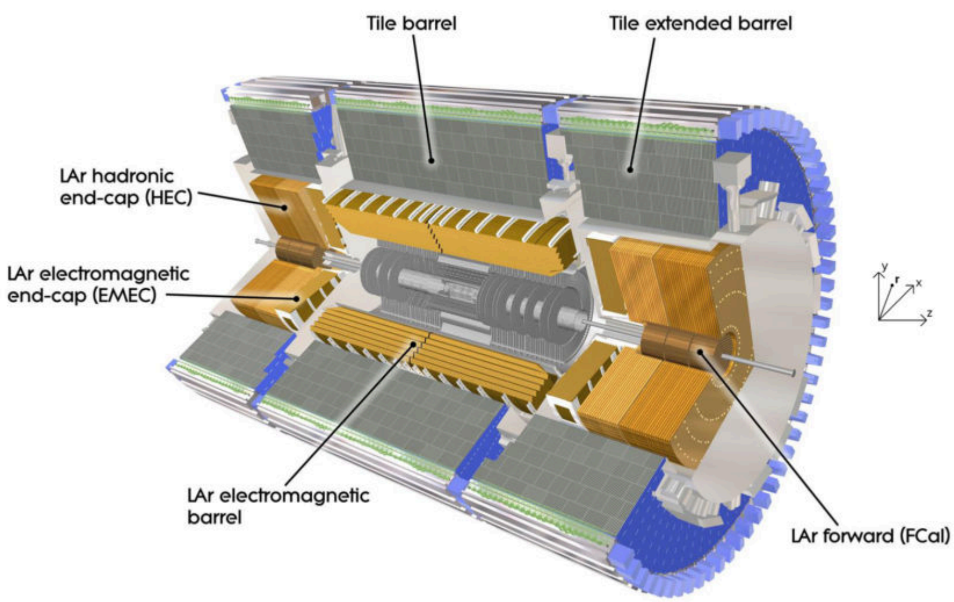

Figure 5.5: The ATLAS calorimeter system consisting of the electromagnetic Liquid Argon Calorimeter and the Hadronic Tile Calorimeter [36].

5.5 Muon spectrometer

The muon spectrometer [37] in the ATLAS detector is operated in a stand alone mode. It is equipped with three superconducting toroids and different tracking chambers for momentum measurements and triggering.
In analogy to the other parts of the detector the muon spectrometer is divided into barrel layers and endcap disks. With its size of 22 m in diameter and almost 44 m in length it covers a range of $\eta < |2.7|$.
The precision measurements are performed using monitor drift tubes (MDTs) equipped with aluminum tubes surrounded by an Ar-CO_2 gas mixture. Because of the large background rate in the larger η region this part has a higher granularity and uses cathode strip chambers (CSC).
Due to the different rates in the barrel and in the endcaps, different detectors were chosen for the trigger system in the two regions. In the barrel so called resistive plane chambers (RPC) [38] with a gas mixture with high primary ionization production, whereas the endcap is build of thin gap chambers (TGC).

5.6 Forward detectors

The ATLAS experiment features two detectors [22] in the forward region to determine the luminosity delivered to the detector. The luminosity is obtained using the Cerenkov Integrating Detector (LUCID), which measures inelastic p-p scattering and acts as the main relative-luminosity monitor located around 17 m away from the IP. Another detector called ALFA (Absolute Luminosity For ATLAS) is located around 240 m apart from the IP and uses scintillating fibers located very close to the beam.

5.7 Trigger system

A sophisticated trigger system helps to filter the interesting events. It would be impossible to save and analyze every event, due to the vast amount of accumulated data.
Thus, each sub-system of the detector has a separate trigger system. It is defined by two levels, the Level 1 (L1) trigger and a combination of the former Level 2 (L2) trigger and event filter. After run 1 the L2 trigger and the event filter were merged to the high-level trigger (HLT). The L1 is a hardware trigger reducing the event rate from the initial 40 MHz to 100 kHz, and the HLT a software based trigger to further reduce the rate to approximately 1 kHz [39]. The increase is caused by the higher center of mass energy of the p-p collision of 13 TeV, a higher peak luminosity and an increase in the maximum number of interactions per bunch crossing.
The hardware L1 trigger is based on the Central Trigger Processor pulling information from the L1

calorimeter trigger and the L1 muon trigger. The processing rate is below $2.5\,\mu s^{-1}$. The filtered events are called Regions Of Interest (ROI) and are forwarded to the HLT with a processing rate of approximately $50\,ms^{-1}$ [39]. In parallel, the accepted L1 events are used to compare with the data read out of other detector subsystems before being sent to the combined Read Out System (ROS). From there the data is filtered with the ROI information gained in the HLT and saved for offline analysis.

Chapter 6

High Luminosity LHC

To extend the discovery potential of the LHC, a major upgrade towards higher luminosity is planned for the time around 2024. This new machine, called the High Luminosity LHC (HL-LHC) [40] is designed to reach a luminosity increase of a factor 10. The integrated luminosity of the LHC is planed to reach 300 fb^{-1} by the end of run 3 around 2020. By upgrading to the HL-LHC an increase to 3000 fb^{-1} over 12 years is expected. This increase would not only make previously inaccessible decay modes available for further standard model cross checks, but also open doors to new physics. The upgrade of the LHC demands for the upgrade of the detectors ATLAS, CMS, LHCb and Alice, in which the two latter ones are upgraded already at an earlier stage and it is not clear yet if they will be operated in the HL-LHC. Especially the inner sector of the ATLAS and CMS detector, which are exposed to the highest radiation dose have to be replaced for further operation.

6.1 LHC upgrade

As described in section 4, the LHC is designed to reach a center of mass energy of 14 TeV with 7 TeV per proton beam. The luminosity is intended to reach $1 \times 10^{34}\,\mathrm{cm}^{-2}\,\mathrm{s}^{-1}$ for the two multi purpose detectors ATLAS and CMS. With a bunch spacing of 25 ns this adds up to an average of 27 events per crossing.

The main goal of the HL-LHC upgrade, is to accomplish the challenge of reaching a luminosity of $5 \times 10^{34}\,\mathrm{cm}^{-2}\,\mathrm{s}^{-1}$, enabling to reach an integrated luminosity of 250 fb^{-1} per year over 12 years.

The performance of the LHC is limited by several technology dependent factors. A revision of the quadrupole aperture to focus the beam is necessary to reach a lower β^*, which is the amplitude function at the interaction point and roughly indicates the width of the beam, to increase the luminosity due to more collisions. On the other side this will also increase the crossing angle representing also a luminosity reducing effect (see equation 4.1).

With the improvement of the beam properties comes also a downside, namely the increase in lost

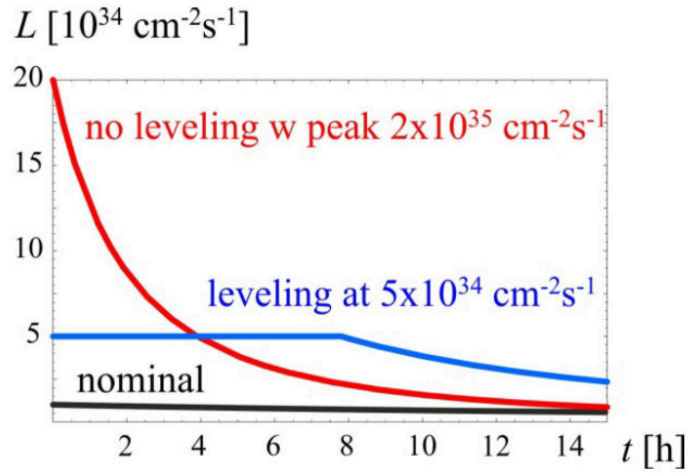

Figure 6.1: Luminosity profile for a single run. At nominal peak luminosity (black line), after the upgrade without leveling and a peak luminosity of $2 \times 10^{34}\,\mathrm{cm}^{-2}\,\mathrm{s}^{-1}$ (red line) and after the upgrade with leveling and a peak luminosity of $5 \times 10^{34}\,\mathrm{cm}^{-2}\,\mathrm{s}^{-1}$ (blue line) [40].

protons due to secondary collisions. By operating the collider with a constant luminosity instead of starting with a peak luminosity which is decreasing quite fast, the integrated luminosity will be almost similar to the one achieved without leveling, but at the same time it reduces the amount of pile up. This will affect the data taking process in a positive way. A luminosity profile for a single run can be seen in figure 6.1. As the reachable peak luminosity will not be set anymore at the beginning of a run, it is called virtual peak luminosity.

The main aim of the upgraded LHC is to enable the detectors to collect as much data as possible in a short period of time. This puts strong constraints to the beam availability and run length. As the luminosity gets restricted, the number of protons per bunch must be increased to achieve longer run lengths.

6.2 ATLAS upgrade

The upgrade of the ATLAS detector [41] [42] during the long shutdown of the LHC for the upgrade to higher luminosities is motivated by numerous factors. To begin with, the detector will face a much higher radiation dose and will accumulate radiation damage in its sub-detectors. Furthermore, the massive increase in events per crossing will demand for a much faster and complex trigger system. This means also a demand for an upgrade of the sub detector readout system.

In the course, the TRT will be removed because it would exceed a 100% occupancy. A new silicon tracker consisting of pixel and strip sensors is being developed to work at much higher particle fluxes and radiation fluences. A track trigger will be implemented to reduce the L1 trigger rates.

The current tracker was designed for a 10 years operation time at a design luminosity of

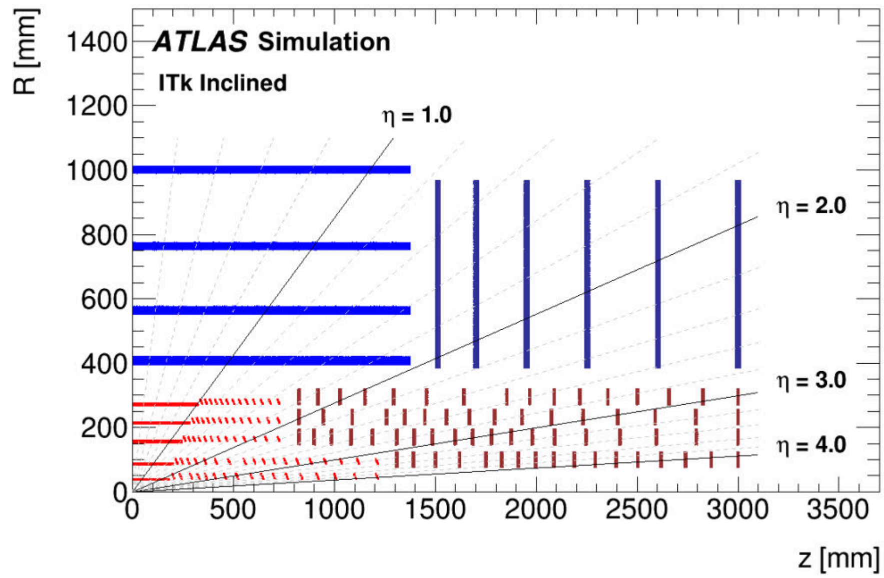

Figure 6.2: Schematic layout of the active ITk parts consisting of pixel and strip sensor layers arranged in cylinders and disks.

$1 \times 10^{34}\,\mathrm{cm}^{-2}\,\mathrm{s}^{-1}$ and pile-up of 23 events with a 25 ns bunch spacing. With its 100 kHz L1 trigger it would not meet the performance requirements of the planned HL-LHC.

Furthermore, the granularities of the Pixel Detector and the SCT are not fine enough and the front-end electronics are constructed to handle up to 50 pile-up events, not nearly enough to cope with the estimated over 200 events per bunch crossing after the upgrade.

There will also be a high demand regarding the physics goals at the future HL-LHC. The track densities will be especially high in regions with high-p_T tracks, which are of special interest for the physics program. It will make the association of tracks with primary and secondary vertices more challenging than ever before.

Several layouts for the inner tracking system based on the requirements previously mentioned were developed and are based on inner pixel sensors and outer strip sensor. Figure 6.2 shows the final ITk layout. The layout consists of five cylindrical pixel sensor layers followed by four cylindrical strip sensor layers. Additionally, six strip disks and four pixel ring layers are planned in the forward region to achieve greater coverage. The inner tracker will be surrounded by a polyethylene moderator, acting as a shield from neutrons entering from the calorimeter.

The biggest changes are the removal of the TRT and the increased radius of the silicon tracker, smaller pixels, more pixel layers providing more hits in the forward region, an increase of granularity in the strip sensors and a better momentum resolution due to an increased active outer radius. Non-sensitive material is moved out of the active region as far as possible.

Besides the ubiquitous radiation damage in the Liquid Argon Calorimeter, another reason to replace the front-end and back-end electronics is to provide real-time performance capabilities of the trigger system. This also applies for the Tile Calorimeter, which will undergo a complete replacement of the readout architecture to meet the requirements of the new trigger system. Furthermore, the Muon Spectrometer will require a main upgrade to increase performance due to the same reasons.

Chapter 7

SCT offline study

This chapter covers the work on the ATLAS SCT simulation. The work includes studies of hardware effects like the crosstalk between strips in the simulated ATLAS SCT strip sensors and the behavior of charge trapping in the SCT with different bias voltages. A study of these effects in the ATLAS SCT simulation helps to give an estimation of the future behavior of the detector and supports the optimization of the same. Details about the SCT sensor can be found in section 5.2.2.
This study aims at analyzing a subset of settings of the SCT simulation and to gain insights into their impact and the future behavior of the detector. Simulated hits were used for digitization with and without charge trapping. In the second part of the study different crosstalk strengths were set to see their influence on various parameters [43]. The real SCT sensors have a binary readout, but in the simulation it is possible to extract the simulated analogue signal during the digitization procedure and to analyze it afterwards. Moreover the results of the crosstalk variation were then compared to data recorded with the ATLAS SCT.

7.1 ATLAS SCT digitisation and reconstruction

Most physics measurements performed by the ATLAS collaboration rely on Monte Carlo simulations, to calculate acceptances or efficiencies, to optimize cuts in searches for new physics phenomena and to understand the performance of the detector [44]. The simulation program is integrated into the ATLAS software framework, Athena, and uses the Geant4 [43] simulation toolkit. The simulation software chain is generally divided into three steps: generation of the event and immediate decays, simulation of the detector and physics interactions and digitization of the energy deposited in the sensitive regions of the detector into voltages and currents for comparison to the readout of the ATLAS detector. The simulated and real data from the detector can then be run through the same ATLAS trigger and reconstruction packages.
Event generation, as the first step, consists of the production of a set of particles which is passed to

detector simulation and runs within the Athena framework. Each generated event contains the particles emerging from a single bunch interaction and modifications to account for the beam properties are applied to the event before it is passed to Geant4. The Geant4 particle simulation toolkit is the standard simulation ATLAS relies on. It provides models for physics and infrastructure, for particle transportation through a geometry and varying detector geometries.
The hits produced by the core simulation are converted into detector responses by the ATLAS digitization software. If the voltage or current on a particular readout channel rises above a specified threshold within a particular time-window a digit is produced to mimic the front-electronics and DAQ to simulate the real detector response [45]. The reconstruction, as last step, is deriving the particle parameters necessary for physics data analysis from the stored raw data: photons, electrons, muons, tau-leptons, K0s, jets, missing transverse energy, primary vertex. A reconstruction algorithm takes one or more collections as input, calls a set of modular tools, and outputs typically one collection of reconstructed objects. Common tools are shared between tracking detectors on one side and calorimeters on the other side [46].

7.2 Radiation damage

There are different effects that can occur in the sensors and can affect the signal as mentioned in chapter 3. Defects induced by radiation are one of the occurring effects. A known consequence of these defects is the charge trapping mentioned in chapter 3, where a charge drifting through the sensor can get caught in a defect and thus will not get read out resulting in a reduced charge collection efficiency. The charge collection efficiency is defined by the percentage of produced free charges that are collected at the strips, where 100% represent the efficiency of a non-irradiated sensor.

7.2.1 Effect of changing bias voltage on the cluster width

The silicon detectors in ATLAS are and will be exposed to a very high level of radiation. Due to displacement defects caused by hadron irradiation, the silicon sensors change their behavior during their lifetime. This can lead to charge trapping [47]. The rate of those defects depends on the irradiation dose of the sensors, which increases significantly in the course of time.
The reduced signal

$$Q_s = Q_0 e^{-\frac{t}{\tau}} \tag{7.1}$$

with Q_0 the signal without trapping, t the collection time and the effective trapping time τ, which differs for electrons and holes and depends on the fluence ϕ

$$\frac{1}{\tau} = \beta\phi, \tag{7.2}$$

with β the trapping constant. The probability of a charge to get trapped while drifting through the sensor is

$$P_t = 1 - e^{-\frac{t}{\tau}} = 1 - e^{-\frac{z}{v\tau}} \tag{7.3}$$

with the sensor thickness z and the drift velocity v. The drift velocity $v = \mu_d(E,T) \cdot E$ is a function of the sensor temperature T, the electric field E and the drift mobility

$$\mu_d = \frac{\frac{v_s}{E_c}}{(1 + \frac{E}{E_c}^{\frac{1}{\eta}})} \tag{7.4}$$

with the constants E_c, v_s and η, which also differ for electrons and holes [48].

This part of the study aims at determining the influence of varying bias voltages on the charge trapping effect at the start of run 2. Potential impacts of charge trapping at smaller bias voltages could have been used for further studies in data. Previous studies of the impact of radiation inside the SCT have been performed [49], whereas this study is concentrating on the effect of the bias voltage.

The threshold defines the lower limit of charge that has to be produced by deposited energy under a strip to create a signal. Since charge trapping influences the amount of charge arriving at the strip, the signal at each strip could be affected. A decrease of the signal on a strip can lead to the signal strength falling below the threshold and thus to a decrease of the cluster size or even a loss of the whole cluster. Therefore, a study of the cluster size for varying conditions of the detector could uncover an effect on future measurements.

The bias voltage has to be adjusted to the changing depletion voltage of the sensors due to radiation damage in the sensor. A change of the bias and depletion voltage directly changes the electric field inside the silicon and therefore the behavior of the charge drifting through the sensor. The fluence received in the innermost barrel layer of the SCT increased to $\phi \approx 4 * 10^{12}$ MeV$\frac{\mathrm{n_{eq}}}{\mathrm{cm}^2}$ at the end of run 1. Simulations predict a fluence of $\phi \approx 4 * 10^{13}$ MeV$\frac{\mathrm{n_{eq}}}{\mathrm{cm}^2}$ at the end of run 2 and a fluence of $\phi \approx 10^{14}$ MeV$\frac{\mathrm{n_{eq}}}{\mathrm{cm}^2}$ at the end of run 3.

An increasing irradiation of the sensor will affect the depletion voltage for a certain depletion depth, which first slowly decreases to the point of type-inversion to start raising again. The depletion voltage for the innermost SCT barrel layer of -70 V is expected at the start of run 2 after the type-inversion during run 1 [50]. Simulations including the estimated cooling plan show, that the depletion voltage will decrease to -270 V at the beginning of run 3. Figure 7.1 shows the change of the mean cluster size with increasing bias voltage at a fluence of $\phi = 4.2 * 10^{13}$ MeV$\frac{\mathrm{n_{eq}}}{\mathrm{cm}^2}$. The effect of charge trapping is around 2%, which would not visibly influence the cluster size in ATLAS. At a higher radiation dose the effect gets bigger but not recognizably large as it is shown in figure 7.2. The change in mean cluster size has its maximum at approximately 3% for a sensor on the borderline to being under-depleted.

Nevertheless, the study showed that the adaption of the bias voltage and the following change of the electric field inside the sensor has a noticeable impact on the amount of collected charges and

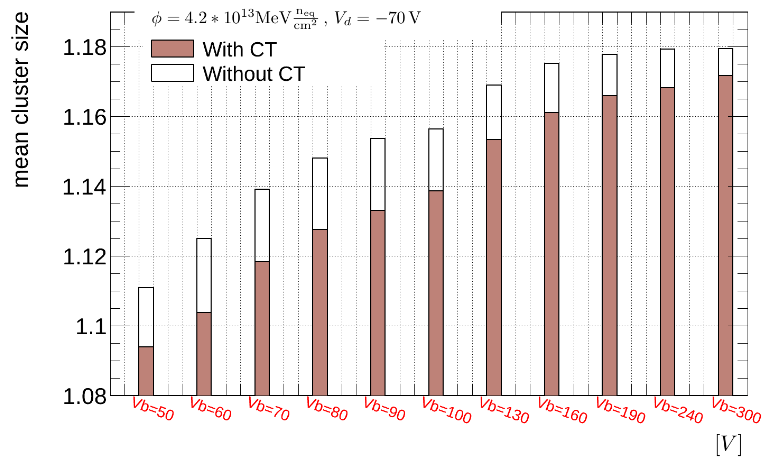

Figure 7.1: Dependency of cluster size on charge trapping with increasing bias voltage.

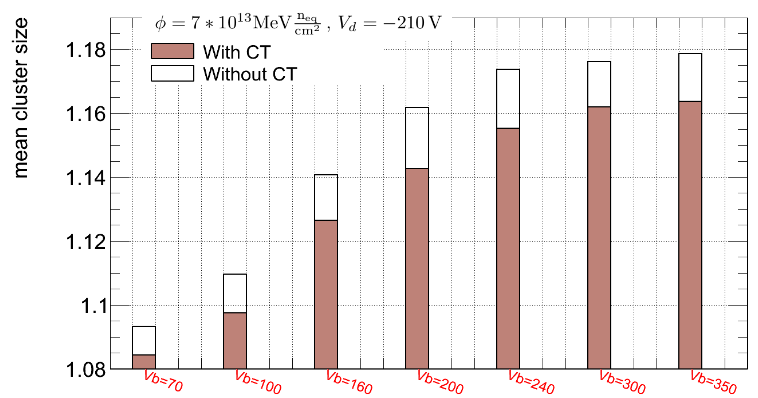

Figure 7.2: Dependency of cluster size on charge trapping with increasing bias voltage.

therefore the cluster width. Strips that would have a signal without charge trapping can have a damped signal, which is not reaching the threshold anymore with charge trapping happening in the sensor. This affects the outer strips in a cluster with lower signals first and reduces the cluster width.

7.3 Crosstalk

Every segmented detector is exposed to the effect of crosstalk shown schematically in figure 7.3. An ionising event in the silicon creates a signal on strip k, which introduces fake signals on the neighboring strips k-1 and k+1 due to the inter-strip capacitance. The cluster width, where a cluster consists of adjacent strips with a signal above a predefined signal strength (threshold), is an important parameter to see the impact of the crosstalk. The crosstalk can cause a widening of the clusters

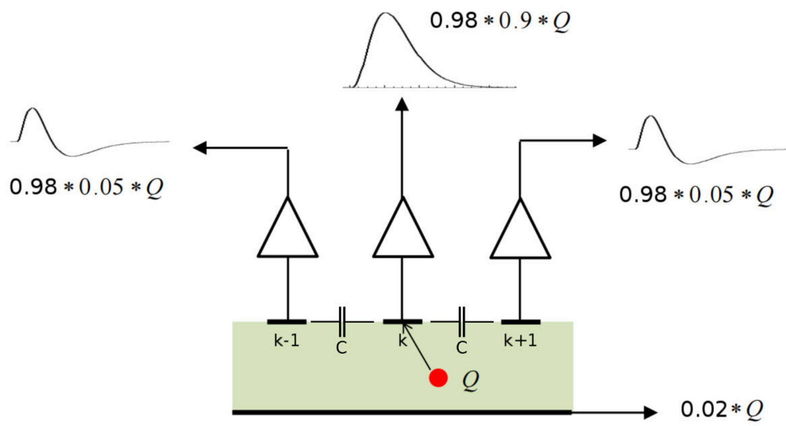

Figure 7.3: Scheme of the capacitive crosstalk effect in a micro strip detector. Fake signals appear on the neighboring strips k-1 and k+1 after an ionising event produced a signal on strip k. In total 2% of the charge is transfered to the backplane of the sensor and 5% to each neighboring strip [51].

by transferring charges to neighboring strips. It is directly related to the spatial resolution and the hit efficiency of the detector, which gives the fraction of hits per possible hit. The final output of the SCT amplifiers is not simply proportional to the amount of charge collected on a strip. The amplified signal $A(t)$ is a convolution of the signals of arriving charges Q_i at times t_i.

$$A(i) = \sum_i Q_i a(t - t_i), \tag{7.5}$$

where $a(t)$ is the response to a single charge depositing energy under a strip:

$$a(t) = \begin{cases} C(\frac{t}{\tau})^3 e^{-\frac{t}{\tau}} \text{ for t} > 0 \\ 0 \text{ for t} \leq 0 \end{cases}, \tag{7.6}$$

where C is a normalization factor and τ is the peaking time. Two different effects are appearing due to detector capacitance, namely the crosstalk to the high voltage backplane of the sensor and the crosstalk between single sensor strips. The first one causes an effective charge loss of 2% and the latter one causes a total charge loss of 10% (5% to each neighboring strip) on the strip that collects the charge [52]. Both effects are parameterized in the SCT digitization process and the parameters associated to the two different types of crosstalk are set to the above values. The crosstalk between neighboring strips is set to first order so that only immediate neighbors are affected. The signal $B(t)$ induced on each neighbor strip is again a convolution:

$$B(t) = \frac{1}{2} K \sum_i Q_i b(t - t_i), \tag{7.7}$$

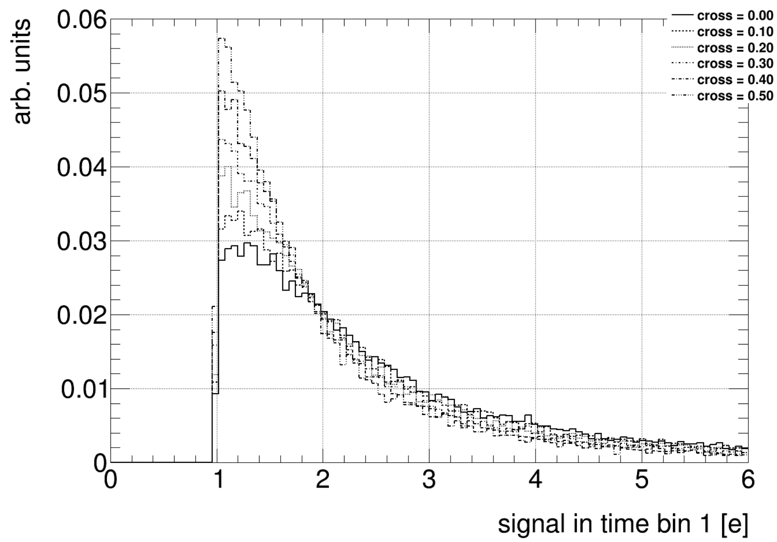

Figure 7.4: Signal of the highest strip of a cluster in time bin 1 with threshold at 6241 fC.

where K is the crosstalk and $b(t)$ is the derivative of $a(t)$:

$$b(t) = \begin{cases} C_2(\frac{t}{\tau})^2 e^{-\frac{t}{\tau}}(3 - \frac{t}{\tau}) \text{ for t} > 0 \\ 0 \text{ for t} \leq 0 \end{cases}, \tag{7.8}$$

The normalization factor C_2 is set so that the function reaches 1 at $t = (3 - \sqrt{3})\tau$, which is lower than the maximum peaking time 3τ where $A(t)$ reaches its maximum. This makes the choice of the threshold time very crucial [52].

7.3.1 Crosstalk in the analogue signal

The implementation of the SCT frontend electronics and the process of the SCT digitization in the software is managed in packages containing loops over all SCT strips to look for signals above threshold and to form the clusters. During the formation of the clusters, the following information is written into a ROOT [53] file:

- cluster number for identification
- first strip (the strip with lowest strip id in a cluster)
- last strip (the strip with highest strip id in a cluster)
- cluster size
- position of the cluster inside the detector
- barrel layer number

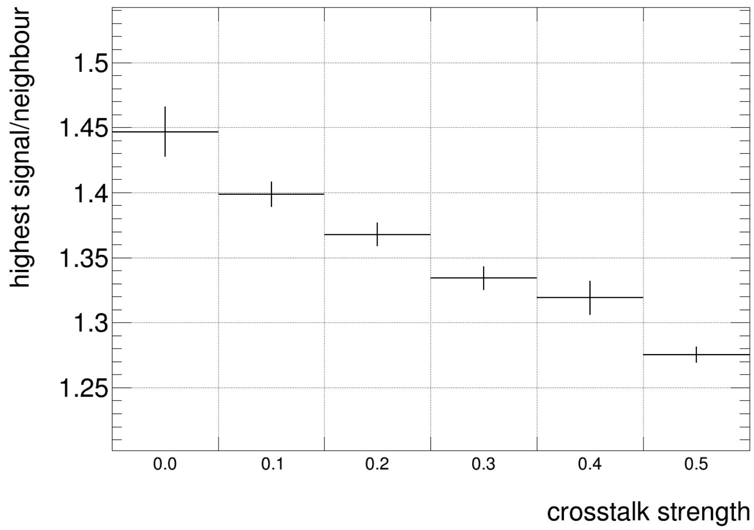

Figure 7.5: Ratio of highest signal to second highest signal in a cluster.

- layer side
- signal in time bin 0
- signal in time bin 1
- signal in time bin 2

The SCT reads out three time bins of 50 ns bin or 25 ns bin length, corresponding to the bunch spacing. During run 1 the spacing between the bunch crossings was mostly 50 ns. The hits should follow the pattern "01X" where 0 means no signal in the first 50 ns bin (bin 0), 1 means signal over threshold in the second 50 ns bin (bin 1) and X means no restrictions in the third 50 ns bin (bin 2). The signal strength in time bin 1 is shown in figure 7.4 where the signal is cut off at 6241 fC, which is the amplified signal generated by the charge of one electron and set as default threshold.
The crosstalk causes a decrease of the signal due to the transfer of charge to the neighboring strip. This effect becomes visible in the increasing amount of strips with lower signal energy for increasing crosstalk strength. Figure 7.5 shows the ratio of the highest signal to the highest neighbor signal inside a cluster. The plot shows a decrease of the ratio with increasing crosstalk strength. This behavior is expected because raising the crosstalk should make the two highest signal strength closer to each other. In general the analogue signal would be the best way to analyze the crosstalk in detail, but since the SCT readout is digital this information gets lost during the digitization process.

7.3.2 Crosstalk in Monte-Carlo and data

This study aims especially at examining the change of cluster size due to the crosstalk between neighbouring strips. Crosstalk between strips of the SCT modules results in a charge transfer and

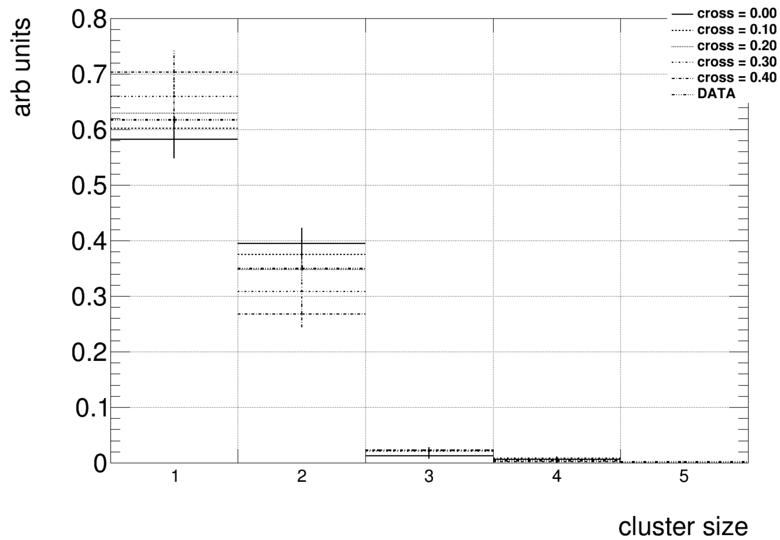

Figure 7.6: Cluster size distribution for varying crosstalk strength.

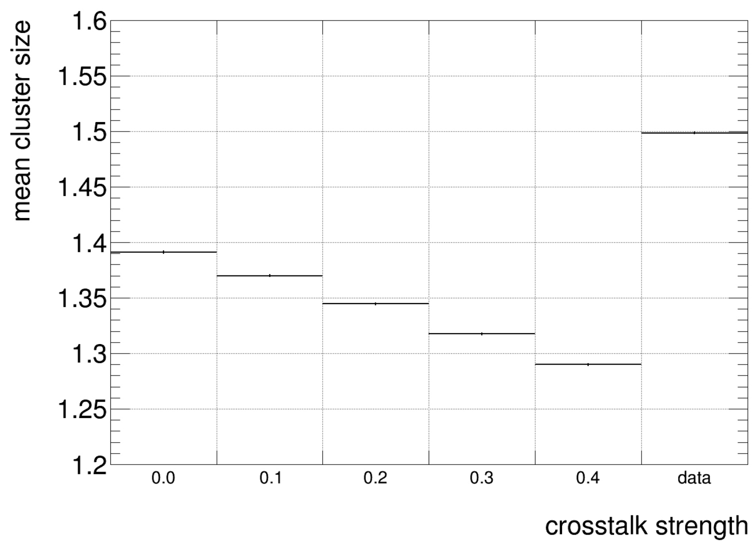

Figure 7.7: The mean cluster size for varying crosstalk strength.

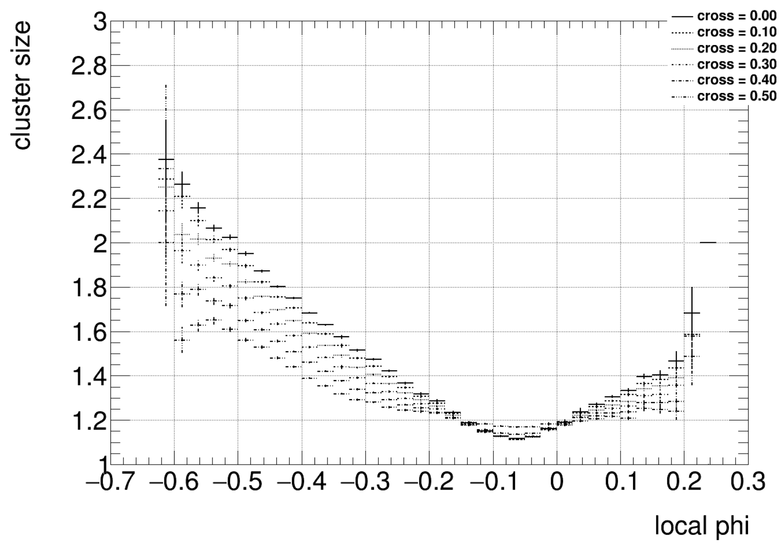

Figure 7.8: The cluster size versus incident angle φ for different crosstalk strength in the simulation.

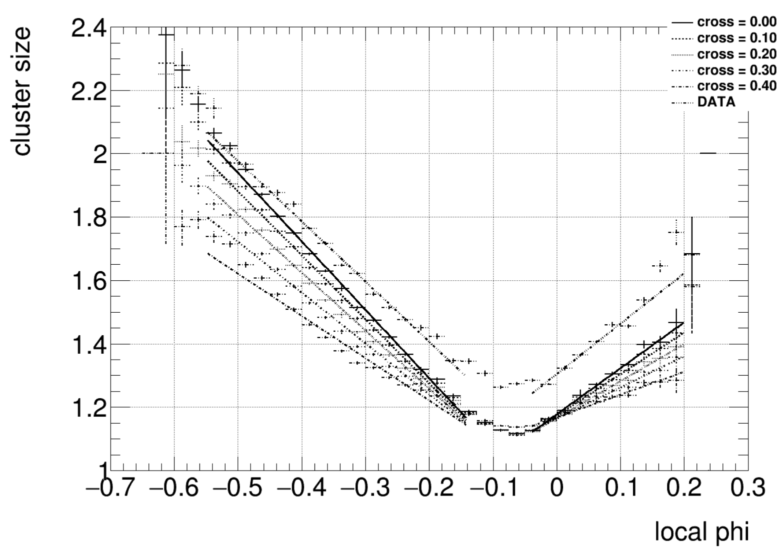

Figure 7.9: The cluster size versus incident angle φ for different crosstalk strength compared to real data. Linear fits are applied to compare the slope of the functions.

Table 7.1: Linear fit functions of the cluster size against incident angle φ plot.

crosstalk	a (left)	b (left)	a (right)	b (right)
0.0	-2.161 $\pm$ 0.015	0.859 $\pm$ 0.005	1.453 $\pm$ 0.036	1.178 $\pm$ 0.002
0.1	-2.019 $\pm$ 0.015	0.872 $\pm$ 0.005	1.314 $\pm$ 0.035	1.174 $\pm$ 0.002
0.2	-1.831 $\pm$ 0.015	0.892 $\pm$ 0.005	1.164 $\pm$ 0.034	1.167 $\pm$ 0.002
0.3	-1.603 $\pm$ 0.015	0.921 $\pm$ 0.005	0.982 $\pm$ 0.033	1.165 $\pm$ 0.002
0.4	-1.332 $\pm$ 0.015	0.954 $\pm$ 0.005	0.713 $\pm$ 0.035	1.170 $\pm$ 0.002
data	-1.900 $\pm$ 0.015	1.026 $\pm$ 0.006	1.590 $\pm$ 0.038	1.306 $\pm$ 0.002

thus in a possible change of the size of a cluster.

The data sample is a 50 ns run and the simulation was run at 50 ns too. The cluster size distribution is shown in figure 7.6, where the number of clusters with one strip increases with the crosstalk strength and the number of clusters with two strips decreases with increasing crosstalk strength. The data sample lies in between crosstalk strength 0.1 and 0.2 for cluster size one and two. The crosstalk is causing the flattening of the cluster due to the charge spreader over a larger number of strips. This effect causes the lower signal of some two strip cluster to shrink below the threshold.

Figure 7.7 shows the mean cluster size as a function of the crosstalk strength in the simulation. It decreases with increasing crosstalk strength. There are more effects like charge drifting or effects caused by radiation damage inside the sensor which can affect the cluster size. One way to distinguish these from the changes due to crosstalk is to find a parameter which affects the crosstalk-dependent cluster size in a different way than the other effects do. One of these parameters is the incident angle of the particle arriving at the sensor. This angle is represented by the local φ angle of a track crossing a module. The crosstalk dependence can be seen in figure 7.8.

The varying crosstalk strength manifests itself in a changing slope of the local φ dependent cluster size. This effect could be used to get the crosstalk value for real data, because the slope of a linear fit decreases in magnitude with the crosstalk strength. A first attempt was made using a data sample and by applying linear fits in the form $a * x + b$ to the positive and negative local φ values as shown in figure 7.9.

The fit-functions given in table 7.1 indicate that the crosstalk in the data sample is located around the default value of 0.1 for the left slope. The right slope of the real data sample is slightly steeper than the simulation without crosstalk to the neighboring strip.

The steepness of the slopes is caused by the flattening effect of the crosstalk on the cluster size. The bigger the cluster the higher is the probability of a signal on a strip at the cluster border to slip below the threshold. Since the mean cluster size increases with bigger $|\varphi|$ angles, the effect of increasing crosstalk becomes more visible than for smaller angles.

The minimum values of the slopes in figure 7.9 is not located at the $\varphi = 0$ because of the Lorentz effect affecting the drift direction of the electrons and holes in the sensor. The position of the minimum is called the Lorentz angle.

7.4 Summary and conclusion

The impact of charge trapping on the mean cluster size was studied for different bias voltages. It is unlikely to see the small change in cluster size in real data. A further study of the effect was not considered and the result did not show a need for action.
Furthermore the impact of the crossstalk on single SCT clusters and on the mean cluster size was studied. The decrease of the signal strength due to the crosstalk can cause the signal strength to fall below the threshold and thus to a reduction of the cluster size. Moreover the mean cluster size decreases for increasing crosstalk, caused by the flattening effect on the clusters.
In addition a method has been defined to compare the crosstalk strength of real data with the simulation to estimate the strength in the detector. The slope of the fit functions indicate that the data sample is located around the default crosstalk strength of 0.1. Again, a further study of the effect was not considered and the result did not show a need for action.

Chapter 8

Fluid Dynamics and heat transfer

In particle physics an efficient cooling systems is required to operate a silicon sensor at a low noise level and without risking thermal runaway due to leakage currents. The work at hand presents the results of a generic research and development project investigating micro-channel cooling for silicon sensors. This chapter gives an overview over the fundamentals of fluid dynamics and heat transfer in order to form a knowledge base for the study of a micro-channel heat sink. Both fields are then combined to explain mass and heat transfer in an internal flow in a pipe.
A general introduction to fluid dynamics will provide the understanding of important flow parameters like the viscosity of a fluid and the flow velocity gradient in channels. The flow behavior ranging from laminar to turbulent will be further discussed before introducing the various types of heat transfer. The combination of heat transfer and fluid dynamics will lead to the motivation of using micro-channels in a heat sink.

8.1 Fluid dynamics

Fluid Dynamics describes the way fluids behave in different scenarios. Whether an external force is acting on a fluid surface or if the flow is only caused by the gravitational force, every fluid can be characterized by its behavior in these different situations. To discriminate between fluids with different flow behavior it is necessary to classify them by more than their density and specific weight. These properties can be similar for two fluids with very different flow behaviors. To further differentiate, the fluids are assigned a parameter called the viscosity.
When a fluid is placed between two solid plates of which the bottom one is fixed and the upper one is movable, like shown in figure 8.1, the latter starts moving with a certain velocity U if the plate is put in motion by applying the force P. Examining the behavior of the fluid along the y-axis normal to the plates, a velocity gradient $u = u(y)$ is visible. The fluid in contact with the upper plate will move with the same velocity as the plate, while the fluid in contact with the plate at rest will be at

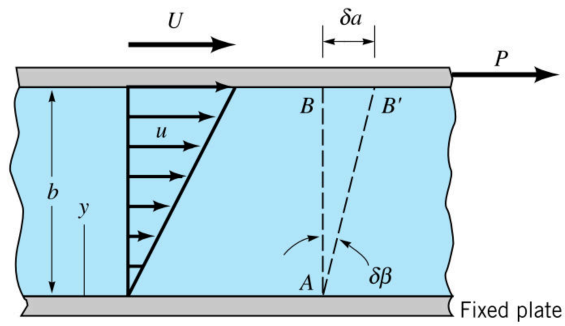

Figure 8.1: A fluid placed between a fixed and a movable plate, with a force P applied to the latter one [54].

rest too. This condition is of big importance in fluid dynamics and is called the no-slip condition. The shearing stress and the velocity gradient can be put in a relationship

$$\tau = \mu \frac{du}{dy}, \tag{8.1}$$

where μ is the viscosity of the fluid. However, the viscosity can be related to the shearing stress in many different ways. The most common one is a linear relation and the fluids belonging to this group are called Newtonian fluids, whereas fluids with a non-linearly related viscosity are called non-Newtonian fluids. Furthermore, the viscosity also depends on the temperature of the fluid in the following empirical way

$$\mu = D \cdot e^{B/T}, \tag{8.2}$$

where D and B are constants and T the absolute temperature [54]. The constants D and B can be obtained by measuring the viscosity at at least two temperatures.

Since the application presented in this thesis is based on a flow of a fluid through rectangular channels, this chapter is focused on the behavior of a fluid flowing through a closed conduit. An open-channel flow, where the pipe is not completely filled and gravity is the main driving force will not be discussed.

The flow in a pipe can be distinguished between three main types, turbulent flow, laminar flow and an intermediate state called the transitional flow. These different flow characteristics depend on the flow rate. Turbulent flow occurs only at large enough flow rates. A detailed discussion follows in section 8.1.1.

A definition of the flow rate and the velocity of a fluid follow from the Navier-Stokes equation, which represents the fundamental equation of fluid dynamics. The Navier-Stokes equations in x-direction follows from the equation of motion and the continuity equation

$$\rho(\frac{\partial u}{\partial t} + u\frac{\partial u}{\partial x} + v\frac{\partial u}{\partial y} + w\frac{\partial u}{\partial z}) = -\frac{\partial p}{\partial x} + \rho g_x + \mu(\frac{\partial^2 u}{\partial x^2} + \frac{\partial^2 u}{\partial y^2} + \frac{\partial^2 u}{\partial z^2}), \tag{8.3}$$

and analogous for the y-, and z-direction, with p the pressure.

The channels used in this work have a rectangular cross section, but there is no analytic solution for a flow through such a channel shape [55]. It can only be approximated by a Fourier sum and simplified for special cases in which $\frac{h}{w} \to 0$. Thus, the solution for pipes with a circular cross section is used as an approximation. A steady, incompressible, laminar flow through a straight tube with a circular cross section, as shown in figure 8.2, is called Poiseuille-flow. In the following the gravity will point downwards in the y direction.

Due to the geometry of a round channel it is more practical to use polar coordinates as shown in figure 8.2. In polar coordinates the Navier-Stokes equation for the r-, Θ-, and z-direction can be simplified to

$$0 = -\rho g \sin\Theta - \frac{\partial p}{\partial r}, \tag{8.4}$$

$$0 = -\rho g \cos\Theta - \frac{1}{r}\frac{\partial p}{\partial \Theta}, \tag{8.5}$$

and

$$0 = -\frac{\partial p}{\partial z} + \mu\left(\frac{1}{r}\frac{\partial}{\partial r}(r\frac{\partial v_z}{\partial r})\right), \tag{8.6}$$

due to the laminar flow with $v_r = 0$ and $v_\Theta = 0$ and following from the continuity equation $\frac{\partial v_z}{\partial z} = 0$. Also v_z is not a function of the time t or Θ, but only a function of r.

The pressure p acts on the plane defined by z and Θ, thus p can be derived by integrating equation (8.4) and (8.5)

$$p = -\rho g(r\sin\Theta) + f_1(z) \tag{8.7}$$

with $f_1(z)$ a constant of integration. The velocity in z is obtained by integrating the equation of motion in z-direction

$$v_z(r) = \frac{1}{4\mu}\left(\frac{\partial p}{\partial z}\right)(r_0^2 - r^2), \tag{8.8}$$

with r_0 the maximum radius of the pipe. From equation 8.8 the flow rate Q can be derived as

$$Q = \frac{\pi r_0^4 \delta p}{8\mu l}, \tag{8.9}$$

with l as the length of the pipe and δp as the pressure drop which follows from

$$\frac{\delta p}{l} = -\frac{\partial p}{\partial z}. \tag{8.10}$$

The velocity profile in a cylindrical pipe as given by equation (8.8) has to develop first after entering the pipe. Along the way from the entrance region to a fully developed flow as shown in figure 8.3, the fluid forms a boundary layer due to the viscous forces. This layer marks the region in which the viscous forces can not be neglected.

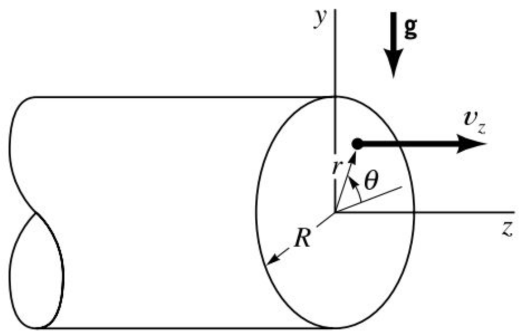

Figure 8.2: Flow through a cylindrical pipe [54].

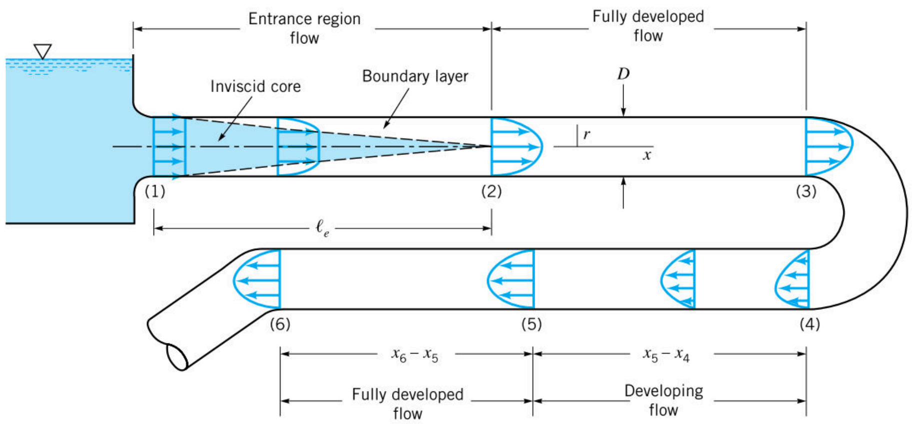

Figure 8.3: Velocity profile of a fluid in a pipe changing along the path [54].

Instead of the radius r another characteristic length, namely the hydraulic diameter

$$D_h \equiv \frac{4A}{P_c} \tag{8.11}$$

can be used [56], where A is the cross sectional area of the channel and P_c the circumference of the wetted area. Since the channels are considered to be completely filled, it follows that P_c is the circumference of the channels $2h$ + $2w$, with h the height of the channels and w their width as shown in figure 8.4.

8.1.1 From laminar to turbulent flow

Laminar flow along a pipe has only one component of velocity pointing along the flow direction parallel to the pipe. Turbulent and transitional flows have additional randomly appearing velocity components normal to the pipe axis [54]. More precisely, the flow characteristics depend on the density ρ, the average velocity $\overline{V}$, the pipe diameter D, and the viscosity μ of the fluid.

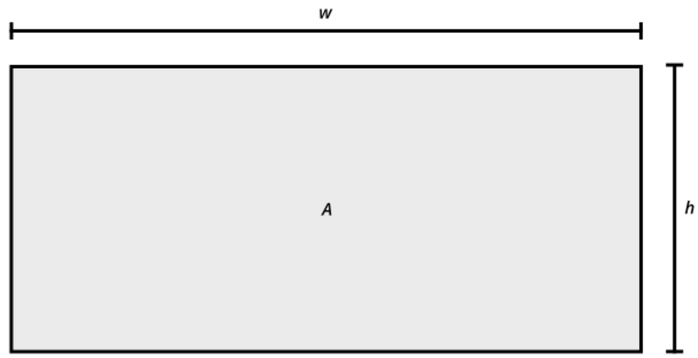

Figure 8.4: Rectangular channel with the height h, width w and cross sectional area A [56].

These parameters are combined in the Reynolds number Re

$$Re = \frac{\rho \overline{V} D}{\mu}. \tag{8.12}$$

The actual value of the Reynolds number at which laminar flow turns into transitional and turbulent flow depends on various factors. It can change due to vibrations, the wall surface roughness or the properties at entrance regions [54]. The flow stays laminar up to a Reynolds number of about 2100 and turns turbulent at around 4000. In between this region the flow can switch from laminar to turbulent depending on previously mentioned characteristics. When the Reynolds number exceeds the critical value of 2100, the axial components of the fluid velocity $V(t) = V(x, y, z, t)$ start to become random. The irregularities in the flow can have a strong effect on properties like the pressure drop or the heat transfer.

Turbulent flow is a very complex process, which still remains the least understood area of fluid dynamics. In the following the transition from laminar to turbulent flow and the main characteristics of turbulent flow will be discussed. The big difference between laminar and turbulent flow is not simply the randomness, but the scale at which the randomness takes place. In turbulent flow it happens on a macroscopic scale, with molecule clusters moving in random directions and in laminar flow this happens on a microscopic scale. As the energy transport rates in turbulent flows are much bigger, this behavior can also implicate an enhancement of the heat transfer due to the proportion of non diffusive energy transfer in the boundary layer. On the other hand, laminar flow keeps the pressure drop in a pipe much lower [54] and helps to keep it inside a critical range, which is especially beneficial for devices that are sensitive to pressure. To summarize, the random variations appear in every variable that can be described by a field like the velocity, the pressure, the shear stress or the temperature.

The fluctuations are strongly influenced by the flow properties near the wall. The no-slip condition and the wall shear stress occur in a very small layer close to the wall. Small irregularities in this layer can cause a transition from laminar to turbulent flow.

8.2 Heat transfer

What the conservation of mass is in fluid dynamics, is the conservation of energy in heat transfer [56]. Following from the first law of thermodynamics, which states that the energy in a closed system is constant, there has to be a boundary where energy can enter or exit the system to cause changes.

The energy in the system consists of kinetic energy, potential energy and internal energy. In most mass and heat transfer cases the sum of kinetic and potential energy can be neglected. The internal energy on the other hand is composed of a sensible component, accounting for any movement of the atoms, a latent component, accounting for phase changes, a chemical component and a nuclear component, accounting for the chemical bonds and the binding forces in the nucleus, respectively. All components but the sensible part are negligible in most cases. When a fluid enters the system with the mass flow $\dot{m}$ the inflow would be

$$\dot{m}(u_t + pV_f + \frac{1}{2}V^2 + gy), \tag{8.13}$$

with u_t the thermal energy per unit mass, the mechanical (kinetic and potential) energy $\frac{1}{2}V^2 + gy$ with V the fluid velocity and g the acceleration of gravity. The term pV_f accounts for the work done by pressure forces with V_f the specific volume of the fluid. Thus, a steady-state flow without thermal energy generation can be expressed as

$$\dot{m}(u_t + pV_f + \frac{1}{2}V^2 + gy)_{\text{in}} - \dot{m}(u_t + pV_f + \frac{1}{2}V^2 + gy)_{\text{out}} + q + \dot{W} = 0. \tag{8.14}$$

with q the rate of heat transferred into the system and $\dot{W}$ the work remainder accounting for example for a possible expansion of the system.

Assuming an incompressible fluid and constant specific heat C_p the equation can be simplified to the thermal energy equation

$$q = \dot{m}C_p(T_{\text{out}} - T_{\text{in}}) \tag{8.15}$$

to obtain the heat transfer into a fluid, with T_{in} and T_{out} the inlet and outlet temperature of the fluid. There are three ways of heat transfer, namely conduction, convection and radiation.

8.2.1 Conduction

Conduction is the transfer of energy from a more energetic object into a less energetic object. To compute the amount of energy being transferred, so called rate equations are being used. The equation utilized specifically for heat conduction is called Fourier's law and gives the energy transferred in the unit $\mathrm{W\,m^{-2}}$ [56].

For a wall with a temperature distribution $T(x)$, as shown in figure 8.5, the heat flux in x-direction

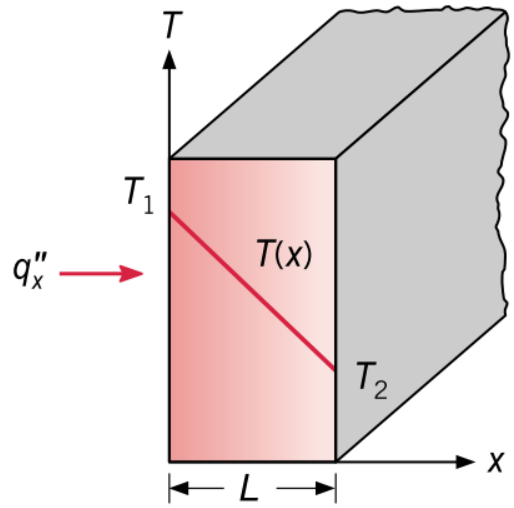

Figure 8.5: Heat conduction through a wall with temperature gradient $T(x)$ and thickness L [56].

through the wall would be:

$$q'' = -k\frac{dT(x)}{dx}, \tag{8.16}$$

with k the thermal conductivity of the wall.

8.2.2 Convection

Convection is an interaction of two different mechanisms. One part of the energy transfer occurs due to diffusion, the other part due to macroscopic motion of the fluid. As discussed in section 8.1, a fluid moving over a surface develops a velocity gradient due to shearing stresses. The boundary layer at the wall in the fluid also exists for the temperature distribution when the fluid and the surface temperature differ, and is called the thermal boundary layer. The effect is shown for the velocity and the temperature in figure 8.6, with a velocity gradient $V(y)$ and a temperature gradient $T(y)$ perpendicular to the flow direction x. The fluid at the wall surface has the same temperature T_s as the wall, and the fluid beyond the thermal boundary the temperature T_∞. The contribution of diffusion and macroscopic molecular motion depends on the distance to the wall. As the fluid in contact with the wall is at rest diffusion dominates in that region, but at increasing distances bulk movement of the fluid dominates the heat transfer.

Convection can be further divided into free convection and forced convection [56]. Free convection occurs when the flow is induced by density differences due to temperature differences. Forced convection results from a forced flow, induced for example by a pump or a fan. Mostly, one of the two modes dominates and a mixture appears only in rare situations, where the forced flow velocity is very small. However, an additional heat transfer can occur due to phase changes of a fluid state to a vapor state. This is called the latent heat exchange. The appropriate rate equation giving the

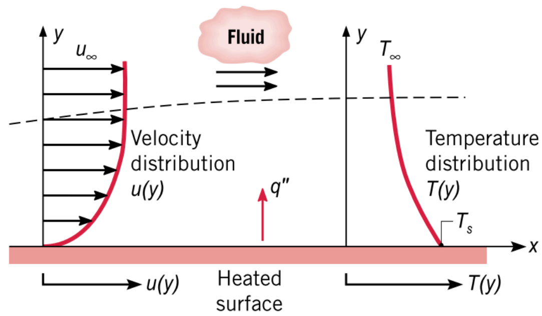

Figure 8.6: Velocity and thermal toundary layers of a fluid moving over a surface [56].

convective heat flux, regardless of its nature, is

$$q'' = h(T_s - T_\infty), \tag{8.17}$$

with h the convection heat transfer coefficient, T_s the temperature of the fluid at the wall, T_∞ the free stream temperature, and is called Newton's law of cooling. The parameter h depends on the surface characteristics which influence the boundary layer in the fluid and the nature of the fluid motion.

8.2.3 Radiation

Radiation is another way of heat transfer which occurs when an object has a non-zero temperature. The surface of that object emits radiation due to the energy bound by the surface material. The rate of emission of a black body is described by the Stefan-Boltzmann law

$$E_b = \sigma T_s^4 \tag{8.18}$$

with T_s the absolute temperature of the surface and σ the Stefan-Boltzmann constant [56]. The equation gives an upper limit for the emission power of a black body. However, the emission of a real body is smaller, and an additional property ϵ, called the emission factor, is introduced:

$$E = \epsilon\sigma T_s^4, \tag{8.19}$$

where ϵ ranges between zero and one, depending on the material and surface properties. The radiation can also be incident, originating from surrounding objects. This incoming radiation G can be either reflected or absorbed, depending on the material properties of the object of interest. The rate of the absorbed energy is given by

$$G_{\text{abs}} = \alpha G, \tag{8.20}$$

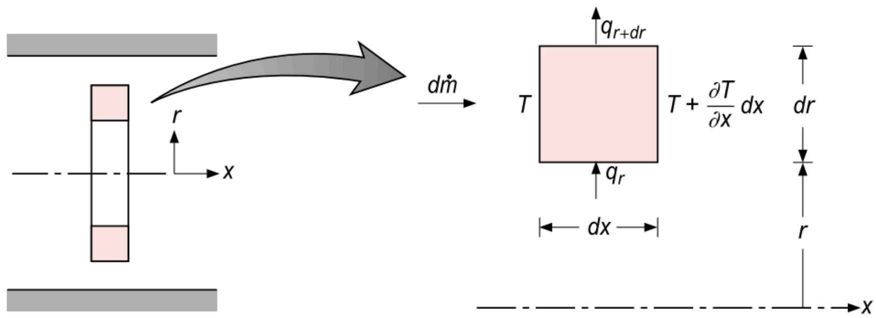

Figure 8.7: Heat transfer for a differential element of a fully developed laminar flow in a circular pipe [54].

with α the absorptivity ranging between zero and one, depending on the opaqueness of the material and the nature of the radiation G. The absorbed energy G_{abs} will hence increase the overall energy of the object.
A typical scenario would be a small surface at temperature T_s surrounded by a large surface, for example the walls of the laboratory at a temperature T_{sur}. Assuming $\alpha = \epsilon$, the net rate of radiation heat transfer q per area A can be expressed as

$$q'' = \frac{q}{A} = \epsilon E_b(T_s) - \alpha G = \epsilon\sigma(T_s^4 - T_{\text{sur}}^4), \tag{8.21}$$

since the emission of the surroundings can be approximated by the emission of a black body $G = \sigma T_{\text{sur}}^4$.

8.2.4 Flow in a pipe

The previous sections introduced the fundamentals of mass and heat flow, which can then be combined. A common interplay of mass and heat transfer is a mass flow through a pipe with a certain heat flux through the pipe surface as shown in figure 8.7. The total convection heat transfer into the fluid can be expressed analog to equation (8.15) to be

$$q_{\text{conv}} = \dot{m}C_p(\overline{T}_o - \overline{T}_i) \tag{8.22}$$

with $\overline{T}_o$ and $\overline{T}_i$ the mean fluid temperature at the outlet and the inlet, respectively [56].
In the following the Nusselt number is derived from the velocity $V(r)$, the mean velocity $\overline{V}$, the temperature $T(r, x)$ and the mean temperature $\overline{T}$. All further considerations are based on a fully developed laminar flow in a circular pipe as shown in figure 8.7. The Nusselt number

$$Nu = \frac{hD}{k} = 4.36 \qquad q_s'' = const, \tag{8.23}$$

Table 8.1: Nusselt number for different channel geometries with uniform surface heat transfer [56].

$\frac{width}{height}$	$Nu \quad q_s'' = const$
circular	4.36
1.0	3.61
2.0	4.12
3.0	4.79
4.0	5.33
triangular	3.11

gives the ratio of heat transferred by convection and by conduction [56].

For non-circular channels, instead of the diameter D, the hydraulic diameter is used (see equation (8.11)). With changing ratio of width and height of the channel the Nusselt number changes. Some important examples are shown in table 8.1. One way of enhancing the convection heat transfer is to increase h by increasing the surface area by adding surface roughness. Another way to enhance the overall heat transfer is to decrease the pipe diameter and use an array of channels, which compensates for the smaller surface. This will decrease the Nusselt number of a single channel, but will increase the total surface of all channels significantly due to the bigger surface to volume ratio. When the channels reach the dimension of micro meters they are called micro-channels. At that size, the classical heat and mass transfer theories discussed here can still be applied [56].

Chapter 9

Layout and Fabrication

This chapter covers the design and fabrication of a micro-channel embedded prototype. As described in chapter 3 silicon sensors have to be cooled to reduce noise due to increased leakage current and to avoid thermal runaway. A novel technique to do so is to directly integrate a cooling structure into the sensor. This method is capable of reducing the overall material of the detector and offers a much more efficient heat transport. The benefits of micro-channel cooling found favor in HEP and are investigated by several experiments such as LHCb [4], NA62 [2] or ALICE [3].
To investigate this technique a prototype of a channel structure etched into silicon was fabricated at IMB-CNM in Barcelona. This chapter presents the layout of the micro-channel device and its production including all necessary steps of fabrication. A prototype was developed with some main criteria: it should fit on a 4 inch wafer and cover a large part of the available area. At the same time the flow distribution across the area should be homogeneous. Flow simulations were used for a first optimization of the design before the prototype was produced and are presented in chapter 10. Based on the results of the simulations, the layout was fixed to the one presented below.
Two different methods were used to fabricate the full micro-channel cooling devices, namely anodic bonding and eutectic bonding. Both methods have channels etched into a silicon wafer, but the sealing of the channels differs. In the anodic bonding process a Pyrex layer is bonded onto the silicon to seal the channels, and in the eutectic bonding method a silicon layer is bonded on the channels with a gold layer in between to ensure the connection.

9.1 Layout

As mentioned previously one constraint on the channel structure was a homogeneous distribution of the coolant across the actively cooled area to keep the temperature gradient on the surface as small as possible.
The layout of the micro-channel cooling device was designed to fit on a 4 inch silicon wafer, which is

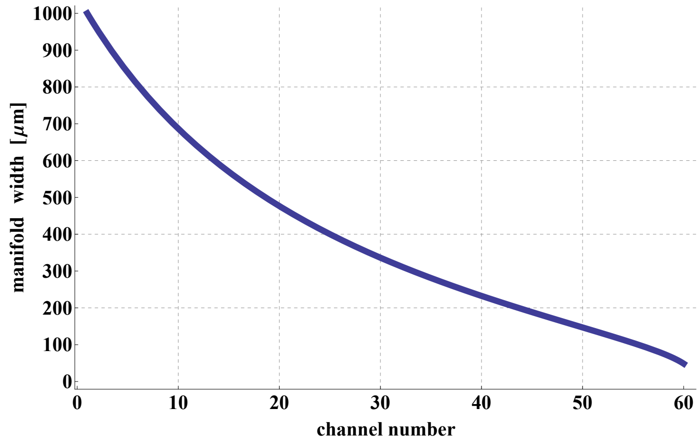

Figure 9.1: The width of the manifold according to equation 9.6, for sixty channels and a starting width of 1000 µm at the first entry to a channel.

a standard wafer size and at that time represented the maximum machinable diameter at IMB-CNM. A design was chosen based on two manifolds connecting sixty smaller channels, which keeps the pressure drop low and prevents a destruction of the device.
The channel height was chosen to be 100 nm, due to mechanical stability of the device. The limiting factor of the channel height is the thickness of the silicon wafer, which varied from 300 nm to 500 nm representing a typical sensor thickness in particle physics. One inlet and one outlet are located on opposite corners of the channel structure and provide the interconnectivity.
To provide a homogeneous flow through all n channels, the pressure at each transition from a manifold to a smaller channel must be the same:

$$\Delta p_n = \Delta p_{n+1} \tag{9.1}$$

with Δp_n (Δp_{n+1}) the pressure drop in the inlet manifold at the entrance to the n-th (n + 1-th) channel. The pressure must be adjusted by decreasing the width of the inlet manifold along the flow direction. The flow in the inlet manifold decreases with the number of channel entries along the way:

$$Q_n = Q_0 - n\frac{Q_0}{N}, \tag{9.2}$$

with Q_0 the total flow through the device, N the total number of channels and Q_n the flow through the manifold at channel n. The pressure drop derived by the Navier-Stokes equation for a circular channel cross section is used as an approximation:

$$\Delta p = Q\frac{8\eta L}{\pi a^4}, \tag{9.3}$$

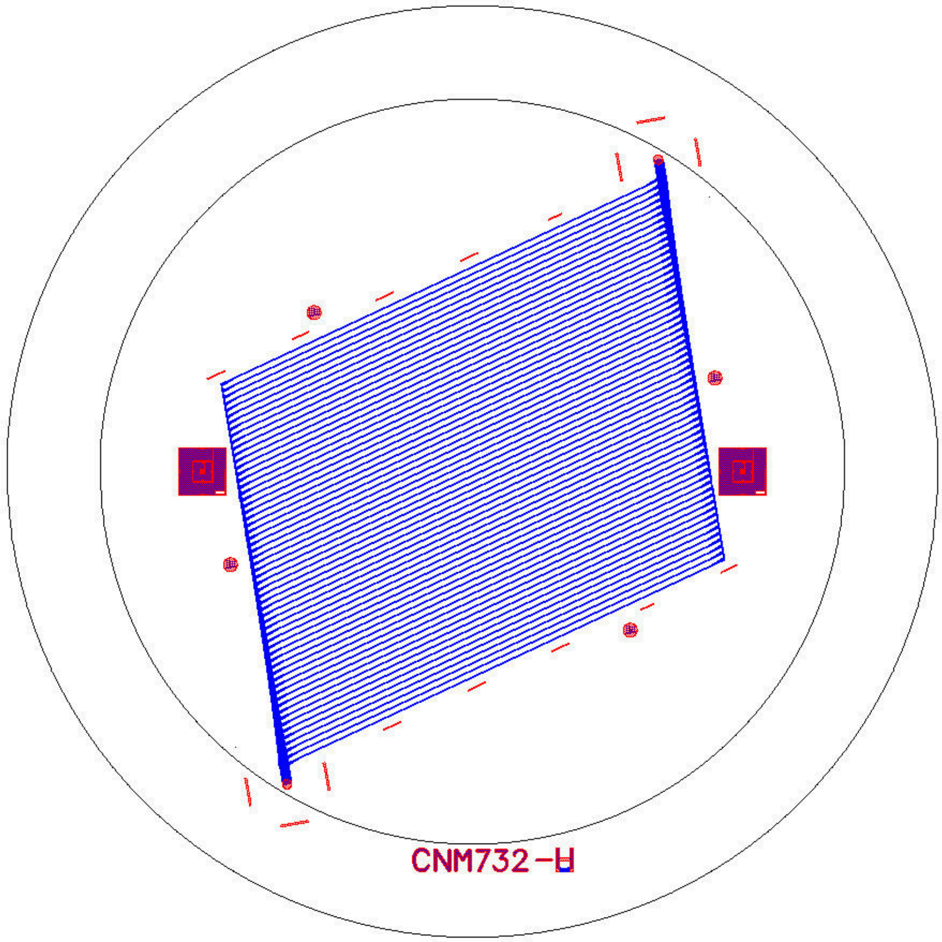

Figure 9.2: Layout of the micro-channels, projected on the outlines of a 4 inch wafer.

with η the viscosity, L the overall channel length and a the characteristic dimension. The characteristic dimension of the manifold at channel n is given by a_m

$$a_m^4(n) = (1 - n\frac{1}{N})a_c^4 \tag{9.4}$$

with a_c the characteristic length of the manifold at the first channel entry. The characteristic length is chosen to be the hydraulic diameter, which in the case of a fully filled channel is

$$a = 2 * \frac{w * h}{w + h}, \tag{9.5}$$

with h the constant manifold height and w the width of the manifold. The hydraulic diameter of the manifold at the entry to channel number n is $a_m(n)$. This results in the width of the manifold at channel n:

$$w_m(n) = \frac{h\left(-\frac{w_c^4 h^4(-1+n-N)}{(w_c+h)^4 N}\right)^{\frac{1}{4}}}{-h + \left(-\frac{w_c^4 h^4(-1+n-N)}{(w_c+h)^4 N}\right)^{\frac{1}{4}}}, \tag{9.6}$$

with a total channel number of N. Due to technical limitations during the etching process the manifold function was approximated by eleven linear sections.
The size of the channels was chosen to be 100 µm high and 100 µm wide with a starting width of the manifold w_c = 1000 µm at the first channel entry. A width of the manifold larger than 1000 µm is not only putting the sample at risk of breaking in that region, but is also causing problems in the fabrication process, due to a possible collapse of the silicon in that region. The layout has sixty parallel channels connecting the inlet and the outlet manifolds with a pitch of 675 µm, in which the pitch width was chosen for mechanical robustness of the device. Figure 9.1 shows $w_m(n)$ as a function of the channel number with a starting width of 1000 µm. The channels were designed with a 15° angle with respect to the perpendicular of the manifolds in order to avoid possible flow separations and limit resulting recirculating flows [54]. The channel entries and ends were widened to further increase the entry angle and to prevent possible turbulence at sharp edges resulting in a structure shown in figure 9.2. One inlet and one outlet hole was added to the manifolds with a diameter of 1 mm. Finally the whole design was rotated by 10° with respect to the wafer axis to avoid coincidence of the channel etch direction with the silicon crystallographic planes, in order to avoid cracks or full wafer cleaving. Additional technical test structures and alignment marks were added to facilitate processing.

9.2 Fabrication

The fabrication of the micro-channel assembly structure was performed at the Centro Nacional de Microelectronica (IMB-CNM, CSIC) in Barcelona, Spain. Two different bonding techniques were used for different prototypes, namely anodic bonding and eutectic bonding. Each technique has his own benefit why it was used in this work. An anodic bonded Pyrex layer on top of the silicon wafer equipped with micro-channels is useful for visual inspections of the channels. The eutectic bonded prototype with two silicon layers put together represents a more realistic scenario when it comes to the thermal characterization of the prototype.
The fabrication of the anodic and the eutectic bonded prototypes was performed in several steps as shown side by side in figure 9.3. The process for the anodic and the eutectic method starts with a blank 4 inch diameter wafer. After a standard cleaning of the wafer, the layout previously defined was transferred to the wafer by a photo-lithography process. The photo-lithographic resist was used as mask during the silicon etching process. Then, a 100 µm etch was processed with an ALCATEL 601-E equipment [57].
The etching was carried out by the Bosch process [58] to achieve a very anisotropic etching and a high aspect ratio of the micro-channels [59] [60]. The Bosch process is one technology of deep reactive-ion etching (DRIE) based on consecutive steps of silicon plasma etch and deposition of a passivation layer. In the first step a plasma is generated from a gas by applying an strong oscillating electromagnetic field. The free electrons are partially absorbed by the surrounding walls and by

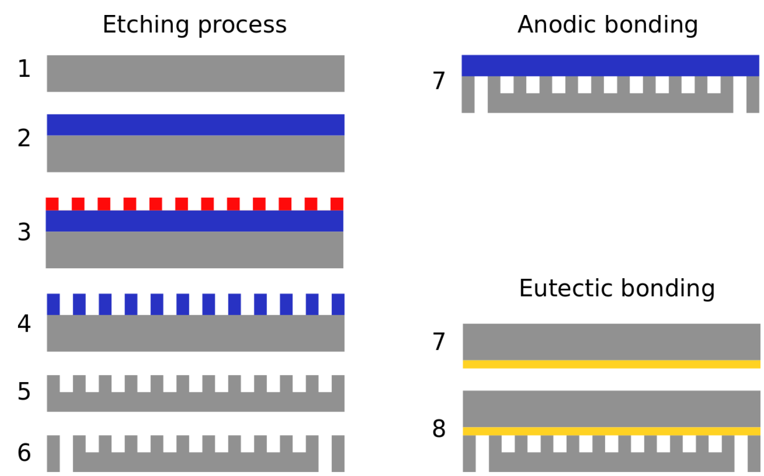

Figure 9.3: The basic steps of micro-channel fabrication of an anodic bonded prototype and a eutectic bonded prototype. Both techniques start with the same steps. One side of a blank wafer (1) is coated with a photo-lithographic resist (2). A mask of the layout is used (3) to transfer the channel design to the resist (4). The 100 µm deep channels are etched into the silicon (5), in another full photo-lithographic process the inlet and outlet holes are added (6). The next steps differ between the anodic and the eutectic bonding process. In the first one the channels are closed with a Pyrex layer (7) and in the latter one a gold layer is added on the second silicon layer (7) and then both wafers are bonded together (8).

the wafer. The voltage difference between the negatively charged wafer surface and the positively charged ions cause a a drift of the latter ones towards the wafer surface where the ions react with the silicon. In the next step a passivation layer is applied to the silicon to protect the walls from further reactions with the ions. A Scanning Electron Microscopy (SEM) picture of the result of this etch and details of the resulting micro-channels are shown in figure 9.4 and 9.5, where the characteristic rippled structure (scalloping) of the deep reactive-ion etching can be seen in the micro-channel walls, which originates from the alternating production steps described above.
After the micro-channels were created on one side of the wafer, a thermal oxide was grown at both wafer sides to protect the micro-channels from the next etching process. A metal mask was defined

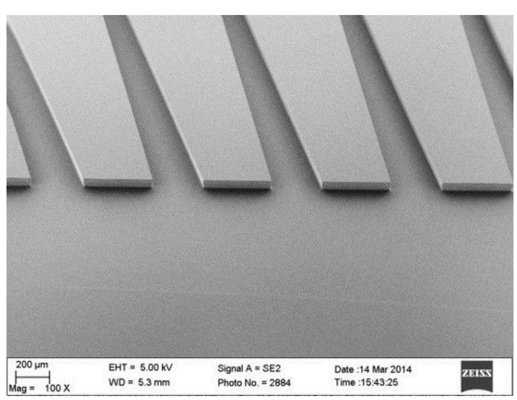

Figure 9.4: Electronic microscopy image of the channels produced by the DRIE process.

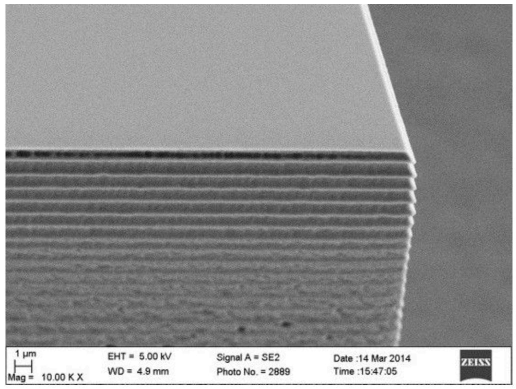

Figure 9.5: Detailed view of the scalloping effect at the micro-channel walls produced by the DRIE process, note the smaller scale compared to figure 9.4.

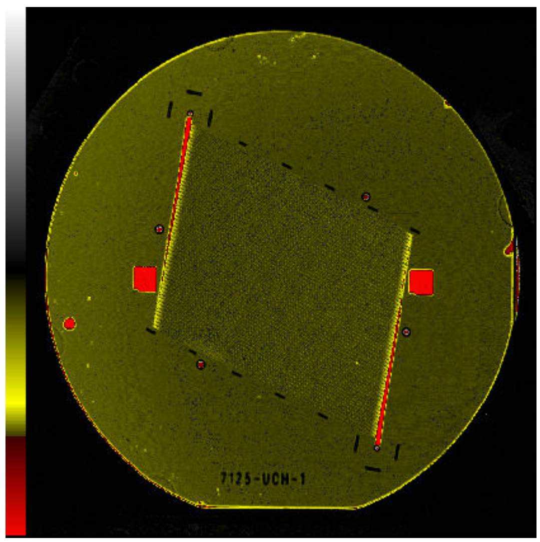

Figure 9.6: Scanning Acoustic Microscopy image of the assembly produced by anodic bonding.

on the wafer by a second photolithographic step, leaving open the areas for the inlet and the outlet that have to be etched through the wafer. The silicon oxide layer previously grown was then etched by a physical dry process in the open areas not covered with metal, and later the second DRIE etch was performed on the same open areas. In this process, the etching continues for the whole silicon thickness, creating through-holes to define the inlet and outlet entries to the micro-channels. Finally, the metal mask was removed, the protecting oxide was wet etched, and a standard set of wafer cleaning steps (RCA clean [61]) was performed on the wafer to leave the bare silicon exposed for the next step by removing organic contaminations, a thin oxide layer and ionic contaminations.
In the second step of the fabrication either a blank 500 µm thick Pyrex wafer was used to close the micro-channels created in the silicon wafer by an anodic bonding process, or a 500 µm thick silicon wafer with a sputtered gold layer on one side was used to close the micro-channels [62] [63].
For the anodic bonding a high potential difference (1000 V) was applied between the two wafers which are in close contact. The high electric field across the wafers enhances the ion interchange

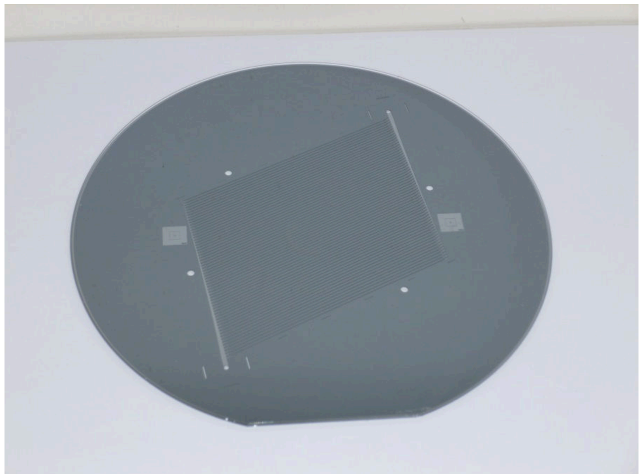

Figure 9.7: Optical image of the resulting assembly. The four white dots around the channel structure are alignment marks.

needed to form the Si-SiO_2 bonding at a relatively low temperature ($< 400\,°C$). The process creates a bond between the two wafers sealing the micro-channels.

In the case of the eutectic bonded prototype, the channels were closed with a second silicon layer equipped with an intermediate gold layer to provide the bonding. The 2000 Å thick gold layer was applied by sputtering deposition on the silicon layer which was designated to seal the channels. The bonding process was carried out by applying a pressure of 7 bar and a temperature of 450 °C.

The assembly of both bonding techniques was then analyzed by Scanning Acoustic Microscopy (SAM) with a Sonoscan GEN-5 equipment, which detects any voids between the wafers, to test the bond quality. An example of the SAM results can be seen in figure 9.6. The micro-channels sealed in the interior of the assembly can be clearly identified together with the alignment marks next to them. Only a small negligible void, recognizable as red dot in figure 9.6, can be seen at the very left edge far away from the micro-channels, probably due to some small particle on either of the two wafers before the process. In figure 9.7 an optical image of the anodic bonded prototype can be seen where the micro-channels are visible through the transparent Pyrex wafer that seals them.

Chapter 10

Simulation of the prototype

Before manufacturing the prototype it is helpful to perform a simulation to investigate the flow behavior. Simulations of the flow through different micro-channel structures were performed in order to ensure a homogeneous flow distribution and to check for a general usability in terms of pressure drop and flow rate.
Simulations are an essential element of the design process and of the subsequent studies of the device. They help identifying possible weak points before producing a real device and can be very useful to develop a practical design. It is cheaper and faster than going through several production steps and first prototyping attempts to test for specific characteristics of a planned device.
Before manufacturing the silicon based micro-channel heat sink, the channel structure was simulated. The main requirements for the channel array in this study - regarding the flow of the coolant - are a homogeneous flow across the device and to stay in an acceptable pressure range for a sufficient flow rate without putting the device at risk of breaking.
First flow simulations were performed using OpenFoam [64], an open source computational fluid dynamics (CFD) software, to test different design ideas. The homogeneity of the flow distribution was tested using singlephase flows and a test for possible air enclosures was realized using multiphase flow simulations.
Steady state simulations were carried out using ANSYS-CFX [65], including singlephase simulations investigating the pressure drop and the coolant stream lines to detect a possible turbulent flow. Studies of the thermal characteristics were carried out by simulating an anodic bonded and a eutectic bonded sample with different with heat loads as well as a prototype cut the dimensions of the channel structure. The simulation was used to obtain local temperature information at certain spots on the silicon surface and contour plots of the temperature distribution across the prototype.
This chapter provides the theoretical and technical background knowledge about computational fluid dynamics and describes the simulation environment, the boundary conditions and model properties. Finally, the results of the simulation will be discussed.

10.1 Computational Fluid Dynamics

Due to the fact that there is no analytic solution to the general Navier-Stokes equations and only very few precise solutions for simplified cases, most studies are performed numerically. There are several approaches, all of them describing the continuous flow field in terms of velocity or pressure at a certain time and location as discrete values at prescribed points in space. These methods avoid using differential equations, which are replaced by simpler algebraic equations.
The method used in this work is called the *finite element method* (FEM). The volume under observation is separated into many smaller volumes, in which the algebraic equations, following from the conservation equations of mass and energy, are solved to obtain the overall flow field. The CFD software used in this work is the CFX [65] package of ANSYS [66] and the open source CFD software OpenFoam [64]. In the following, the approach of computational fluid software is further discussed.

10.1.1 Methods in Computational Fluid Dynamics

The first step of a simulation is to build a three dimensional (3D) model. A model consists of volumes (if 3D), surfaces and lines, which have to be meshed. By meshing one understands the act of dividing the model into a number of elements. The sizes of these elements depend heavily on the purpose of the simulation and the boundary conditions. For example if a movement of a volume should be simulated a force has to act on it, or more precisely on one of the volume surfaces. This is then called a boundary condition. The essential function of the software is solving the calculations in each element with a software specific solver.
The fluid enters through an inlet and exits through an outlet, but the mesh is actually independent of the fluid movement and does not change during the calculations. This is called the immersed solids method, and is used to simulate an infinitive motion of the fluid without the need to re-mesh the fluid volume or simulate a closed fluid circuit connecting the outlet to the inlet [67].
In general, three main approaches can be distinguished: the Direct Numerical Solution (DNS) to the Navier-Stokes equations, the Reynolds-averaged Navier-Stokes equation method (RANS) and the Large Eddy Simulation (LES). DNS can only be applied to simple models at low Reynolds numbers and needs a very high computation power. Calculations based on LES need less computing resources, but still a lot more than RANS. Today, most programs are based on RANS for fluid simulations [68].
Both laminar and turbulent flow calculations were realized in this work. In laminar flow calculations, the velocity field is computed based on the distance to the wall for each element with a constant wall shear stress in the wall boundary region, making the flow behavior at the boundary layer independent of the flow behavior at a greater distance to the wall.
In turbulent flows several methods are used to compute the velocity field with the RANS method, varying from simple models restricted to constant turbulent viscosity (zero-equation models), to

several models including one or more separate transport equation (two-equation models). The most commonly used flow models are based on a combination of two of the following parameters to solve the Reynolds-averaged Navier-Stokes equation: the turbulent kinetic energy k, the angular velocity ω and the turbulence dissipation ϵ. The kinetic energy k is defined as the kinetic energy per unit mass of the turbulent fluctuations and ϵ as the rate at which k is converted into thermal internal energy [69].

Different geometries and diameters of the simulated device demand for suitable solving approaches. One possible combination of two of the parameters mentioned above is forming the k-ϵ method, which is widely used in industry and is known for its robustness. However, ϵ contains velocity terms that are hard or impossible to calculate at the wall boundary and the model does not work accurately with high pressure gradients. Instead of solving ϵ close to a boundary, an approximation is used for the calculations [70]. This problem is avoided in the k-ω model, which represents another combination of the fundamental parameters to solve the Reynolds-averaged Navier-Stokes equation and can be solved near the wall, but with the cost of higher CPU demand. A compromise is represented by the Shear Stress Transport k-ω model (SST), which uses the k-ω approach at the boundaries and blends to a k-ϵ model at greater distances to the wall.

10.1.2 Multiphase flow

Fluid dynamics often include more than one phase or fluid. The biggest challenge is to realistically describe the surface boundary between the two fluids or phases. The most common method to do so is called the Volume Of Fluid (VOF) method [71]. Each point in the model is ascribed a function F_{vof}, which is zero if there is no fluid and one otherwise. If the average of F_{vof} in an element of the mesh is between zero and one, it contains a surface. The orientation of the boundary between the two phases can be obtained through the change of F_{vof}. If an element contains a surface and its normal direction is known, the element can be divided as an approximation to the real surface. The evolution of the F_{vof} field is then calculated as moving with the flow.

10.2 Simulation setup

The simpleFoam solver within the open source CFD software OpenFoam [64] was used to simulate the overall flow distribution along the channel structure in a singlephase approach. Multiphase simulations were realized with the interFoam solver to simulate the initial filling process of the micro-channels.

Both solvers are designed for different problems: the simpleFoam solver is specifically designed to handle steady state calculations for incompressible flows. The interFoam solver is designed to calculate the flow of two incompressible fluids, which are isothermal and immiscible in a transient approach as explained below. The interFoam solver uses a VOF interface capturing approach to

calculate the phase boundary between the fluids (see 10.1.2).
The mesh for the simulations with OpenFoam was constructed with Gmsh [72] and then importedinto the OpenFoam project. All flow simulation configurations with OpenFoam are based on a laminar flow and an incompressible fluid. A pressure was set to the inlet of the structure as driving force for the fluid. The multiphase simulation was divided in two separate fields: the air which was filling the complete channel structure at the start of the calculation, and the fluid entering through the inlet. Both the air and the fluid were treated as incompressible, which might have an effect on the results because the air volume slightly changes in the pressure range assumed here (few bar).
At this point, a main difference between the singlephase and multiphase simulation becomes apparent, namely the transient and the steady state approach. The multiphase approach is transient, which means that it is solved for a series of time steps providing a result after each time step, whereas the singlephase simulation is solved once for a steady state after reaching equilibrium i.e. when the velocity distribution remains constant.
In addition CFX was used for further flow studies and to include the thermal calculations into the setup. The simulations which were carried out with the CFX package were singlephase steady state calculations. The mesh of the 3d model was refined to investigate the effect of the mesh element size on the results. The flow for the thermal studies was assumed to be laminar in all calculations presented here, but a comparison between a laminar flow and two different turbulent flow models was realized, too (see section 10.3.1). Thermal properties of the fluid and the wafer material were added to the simulation setup to calculate the heat flow from a heat source into the wafer and into the fluid and is shown in section 10.3.2.

10.3 Simulation results

This section is divided in two main parts, the flow simulations and the thermal simulations. The flow simulations include the filling process calculated with OpenFoam, the singlephase calculations of the flow distribution with OpenFoam, a detailed mesh study of the singlephase flow calculations and a comparison of the laminar flow model with the k-ϵ and the SST model in CFX.
Thermal simulations were performed with a model of a 4 inch heater attached to the wafer to investigate the temperature distribution on the opposite wafer surface and to probe the temperature on specific spots over the micro-channel structure. A number of results of the simulation are presented in chapter 12 together with the experimental results to avoid a repetition.

10.3.1 Flow Simulations

Before producing the prototype with embedded micro-channels, the initial filling process of the structure was simulated using OpenFoam. Results of the simulation with an inlet pressure of 0.05 bar are shown in figure 10.1. Blue coloring indicates volumes filled with air, while red coloring

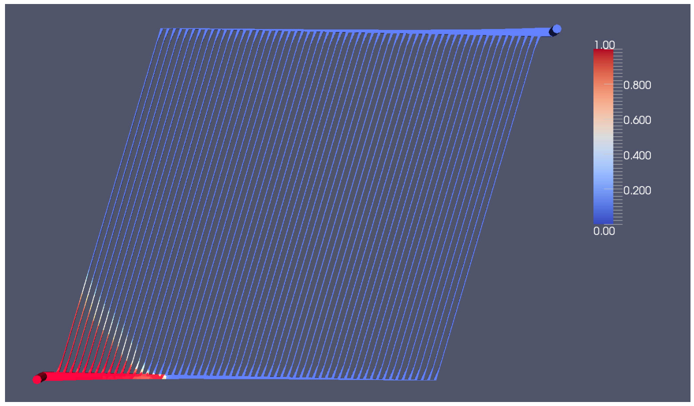

(a)

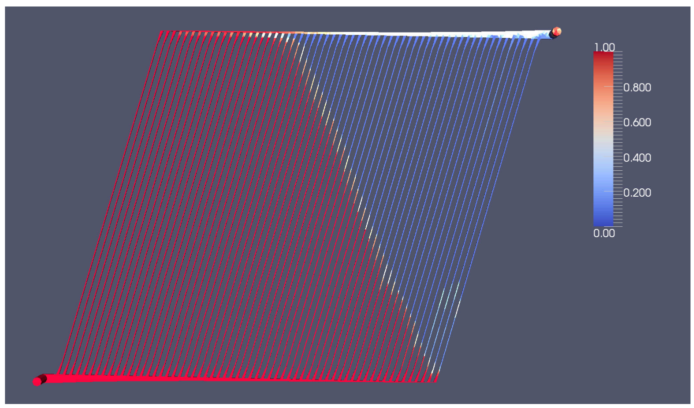

(b)

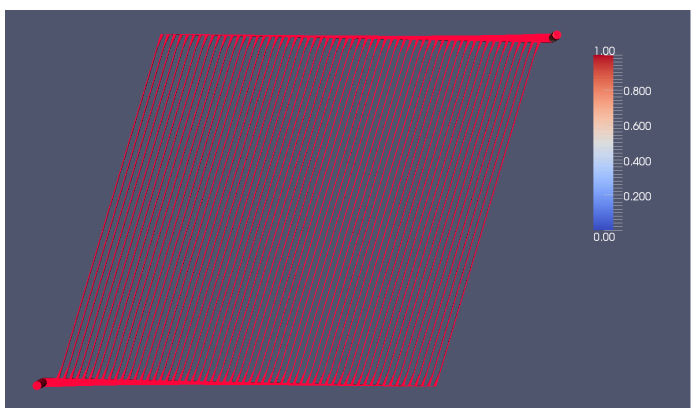

(c)

Figure 10.1: The initial filling of the micro-channels simulated with OpenFoam. The pressure at the inlet was set to 0.05 bar with water at room temperature as coolant. The scales show the fraction used in the VOF method, where 1 stands for the fluid and 0 for the air. The pictures show the result after a) 0.06 s, b) 2.19 s and c) 6 s.

indicate volumes filled with the fluid. The scales in the three pictures show the fraction used in the VOF method, where 1 stands for the fluid and 0 for the air. Figure 10.1 shows the result of the simulation after a) 0.06 s, b) 2.19 s and c) 6 s.

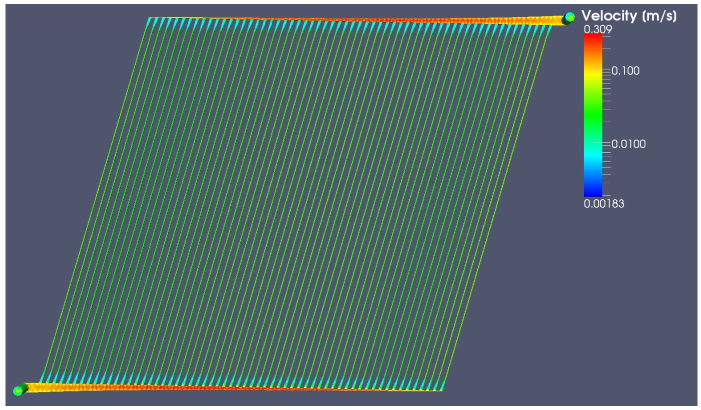

Figure 10.2: Velocity distribution of the fluid across the channel structure with a constant pressure of 0.05 bar at the inlet calculated inside the OpenFoam framework using a laminar flow model and water at room temperature.

The fluid filling process is in a good agreement with the behavior observed in the experiment by filming the filling process through the Pyrex. The homogeneous distribution of the fluid is very important to avoid empty channels due to a misdirected flow. Air enclosures at channel entries known as clogging [73] could lead to an increased pressure drop. However, revealing this problem in a simulation demands a much finer mesh and more processing power than accessible for this work. After the fluid enters through the inlet the channels are filled one after another, and it becomes unlikely that the fluid enters a channel from the top manifold to create a reversed flow or that it skips one channel and an air enclosure is created.

Completely empty channels were observed in the multiphase simulation when the initial pressure at the inlet was chosen around 1 bar, which is a rather high initial overpressure. This behavior did not appear in every calculation, but when it happened, random channels were affected. However, this exact behavior could not be observed in the experimental setup (see chapter 12) and was considered to be an artifact of the simulation. The pressure which has to be applied to the inlet to ensure the fluid to fill all channels and exit through the outlet is increasing with the amount of fluid entering the channel structure. The pressure of 0.05 bar represents a realistic overpressure for the circuit in the experiment, where the micro-channel structure is almost solely causing the pressure drop.

In order to provide a homogeneous cooling of the wafer heated by a homogeneous heat injection, the fluid must be equally distributed across the channel structure. A reference for the flow distribution is the velocity distribution, which is directly connected to the mass flow, since the density remains constant. A velocity distribution with a constant pressure of 0.05 bar at the inlet calculated within OpenFoam is shown in figure 10.2. Although the pressure at the inlet is much less than expected in the experimental setup, the results of the simulation were used as indication of a homogeneous flow distribution.

A feature of great importance is the pressure drop along the channel structure for a given mass flow. It determines whether the device can provide a sufficient flow rate without putting it at risk of breaking. This calculation depends heavily on the mesh quality of the 3d model, due to the

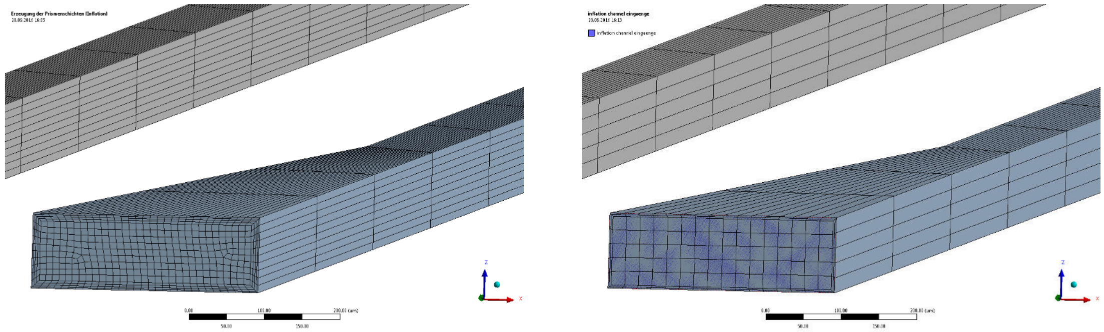

(a) (b)

Figure 10.3: Changing the mesh size in terms of channel entry surface element size and the layer configurations at the walls. The picture a) shows the entry of a channel with four mesh layers at the walls and an entry surface element size of 10 µm, whereas the picture b) shows the same entry with two layers and an surface element size of 20 µm. The element size along the channel length was kept constant.

very thin boundary layers near the walls (see section 8.1). Especially in micro-channels with an increased surface to volume ratio, the flow behavior near the walls is very important and has a big effect on the pressure drop. The model and the calculations to produce the following results were performed in CFX.

To save computing power and time, the mesh should be adapted to the requirements. For a fluid flow through a channel, which is not expected to become turbulent, the center of a channel is not as important to the calculation as the walls or the corners of the channel layout. The mesh element size at each point of the model should be chosen according to this prioritization.

There are several ways to adapt the mesh. Two different methods were used for the mesh study presented here. A general element size can be defined for the elements of any part of the model, which divides the chosen structure into elements with the desired edge length. The mesh refinement at important points can be realized in numerous ways, but since the walls play an important role, mesh layers parallel to the walls with increasing thickness towards the channel center (inflation layers) are an obvious option to increase the precision of the calculations near the boundaries. Typically the thickness of the layers is increasing with the distance to the wall.

Furthermore the channel entry surface and the manifold volumes had a preset element size. The entry surface was chosen because the division of the cross sectional area is of greater importance to capture the velocity profile than the division along the channel length. The manifolds do not have a constant width and have openings along the length for the channels, which makes the mesh division along the manifold length equally important as the cross sectional division.

It was tested to keep the inflation layer configurations at the walls constant and to change only the element size of the channel entry surface as well as to keep the channel entry surface element size constant and to change the numbers of inflation layers at the walls. An example of the changes on the mesh is shown in figure 10.3.

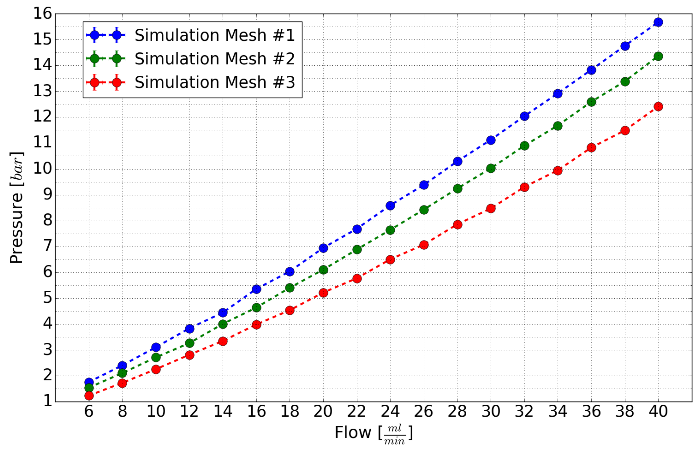

Figure 10.4: Pressure versus flow rate calculated with CFX using the laminar flow model. The element size of the channel entry surface was changed from 20 µm in mesh #1 to 15 µm in mesh #2 and 10 µm in mesh #3 and the manifold element size from 40 µm in mesh #1 to 30 µm in mesh #2 and 20 µm in mesh #3. The number of layers at the walls was set to two with a starting thickness of 2 µm for all mesh configurations.

As already mentioned, the main characteristics of micro-channels is their increased surface to volume ratio compared to channels with larger diameters. The importance of the mesh near the walls is observable in the plots in figure 10.4 and figure 10.5 showing the pressure versus the flow rate through the full micro-channel structure for varying element sizes of the channel entry surface and the manifold volume and changing inflation layer configurations at the walls.
The flow rate of the HFE coolant was increased from 6 ml min^{-1} to 40 ml min^{-1} in 2 ml min^{-1} steps. It is visible that the pressure drop is decreasing with a finer mesh. Changing the overall element size of the channel mesh and of the manifolds was done in three steps. The mesh element size of the channel entry surface was changed from 10 µm to 20 µm in 5 µm steps and the element size of the manifold volumes was changed from 40 µm to 20 µm in 10 µm steps. One configuration with a fixed element size of the channel entry surface and of the manifolds was then simulated with two to five inflation layers at the walls. The layer thickness was growing with a rate of 1.2 and had a starting layer thickness of 2 µm.
The plot in figure 10.4 shows the results for a change of the overall mesh element size with the number of boundary layers at the walls fixed to two. The element size of the channel entry surface and the manifold section was changed from 20 µm and 40 µm, respectively, in mesh #1 to 15 µm and 30 µm in mesh #2 and 10 µm and 20 µm in mesh #3. There is a continuous decrease in the pressure drop for decreasing element sizes. It is also noticeable, that the results for each flow rate show the same general behavior.
The results for a change of the layer number and a fixed overall element size is shown in figure 10.5. The element size of the channel entry and manifold was fixed to 15 µm and 30 µm and the number of inflation layers at the walls were changed from two in mesh #1 up to five in mesh #4. The change in pressure between the different mesh layer configurations is larger than in the previous

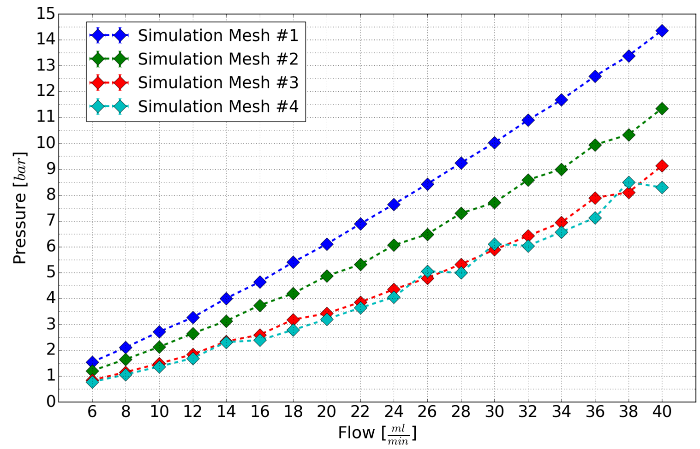

Figure 10.5: Pressure versus flow rate calculated with CFX using the laminar flow model. The element size was fixed to 15 μm at the channel entry surfaces and to 30 μm in the manifolds. The number of layers at the walls was changed from two in mesh #1 up to five in mesh #4, with a starting thickness of 2 μm.

approach (see figure 10.4) and a convergent evolution of the results is observable. The result of the simulation with four and five mesh layers at the walls is almost the same, but the curve with five mesh layers shows more fluctuations. A further mesh refinement did not show an additional pressure decrease or increase but an increase of statistical fluctuations. The results obtained with the mesh with four layers at the boundary walls and a mesh element size of 15 μm in the channels and 30 μm in the manifolds is taken as optimal mesh setup with respect to the available computing power. Although the change of the element size did not show a convergence as the layer number variation, a further refinement of the overall element size would increase the required computing resources to an intolerable level and was therefore not realized.

As shown in figure 10.5 the mesh refining method by changing the number of inflation layers leads to a convergence of the results calculated with different mesh configurations. The remaining fluctuations between the result obtained with four mesh layers at the wall and the result obtained with five mesh layers are used to define the error on the calculations. A comparison with the experimental data is shown in chapter 12.

10.3.1.1 Study of flow separation

In addition to the pressure drop simulations, a detailed study of the flow behavior was carried out at the entry points to the smaller channels. As mentioned previously the flow in micro-channels tends to stay laminar up to high fluid velocities around $10\,\mathrm{m\,s^{-1}}$. The velocities for this study are assumed to keep the Reynolds number in a laminar or transitional range across the geometry. Nevertheless, a transition to turbulent flow can occur when the boundary geometry includes sudden changes along the flow. A flow can undergo a so called separation especially at sharp corners, which can lead to

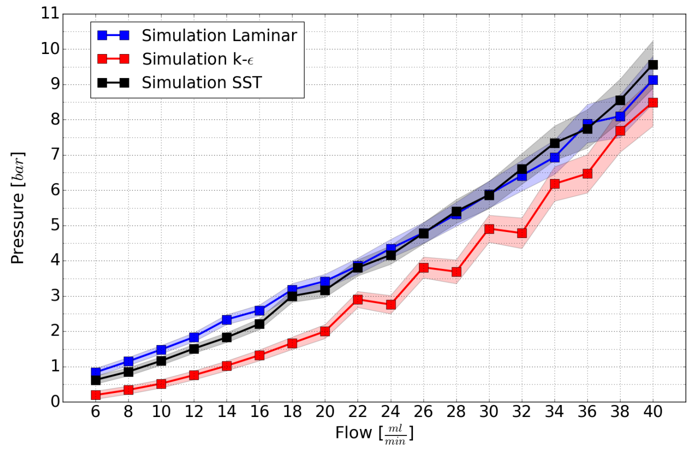

Figure 10.6: Comparison of the pressure drop versus flow rate behavior between the laminar, the k-ϵ and the SST flow model.

recirculating flows also known as vortexes [70].
In principle it is not forbidden to have vortexes in laminar flow [74]. The flow was modeled using the laminar, the k-ϵ and the SST model to compare the results.
The influence on the pressure drop by using different flow models in the simulation is shown in figure 10.6. The laminar model and the SST model are in a good agreement, whereas the k-ϵ model shows a significantly smaller pressure drop. Only at higher flow rates around $40\,\mathrm{ml\,min^{-1}}$, the agreement between the three flow models gets better.
By looking closely at the fluid flow paths in the entry area of the smaller channels, another difference between the three models gets apparent. Figure 10.7 shows channel entries for all three flow models with a flow rate of $20\,\mathrm{ml\,min^{-1}}$. The vortex in the laminar and the SST flow model look very alike. The k-ϵ model was found to not being capable of resolving the vortex in the channel entry region. In order to resolve the recirculating flow in the laminar and the SST flow model, the mesh had to be refined drastically in the entry region. However, the velocities in the channel entrance area are in a similar range for all three models, but the maximum velocities differ a bit. The maximum velocities are reached after exiting the channel and entering the outlet manifold, which is not shown in figure 10.7 but decreases from a) to c). This difference can be explained by the different treatment of the flow near the walls, as mentioned in section 10.1.1.

10.3.2 Thermal simulations

The results for the thermal simulations were obtained using CFX. Two different heat sources attached to the micro-channel device were simulated: first of all a Kapton board with implemented resistors to mimic the heat dissipation of read out chips, secondly a heater pad with the same size as the wafer was carried out to have a homogeneous heating across the full wafer surface and thirdly thermal measurements of a wafer cut to the structure of the channel structure were performed.

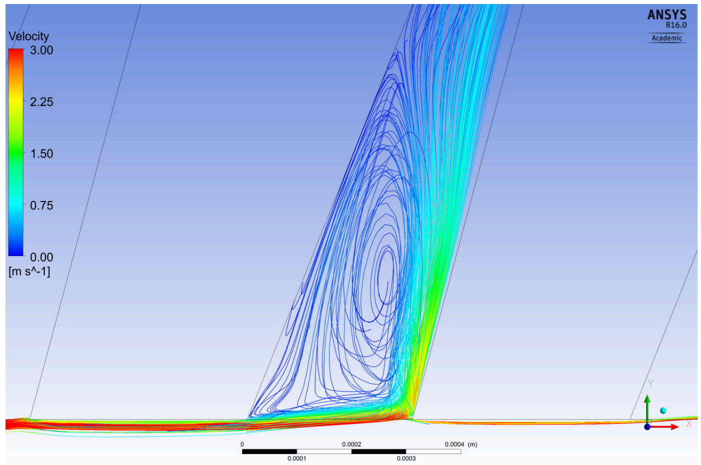

(a) Laminar flow model

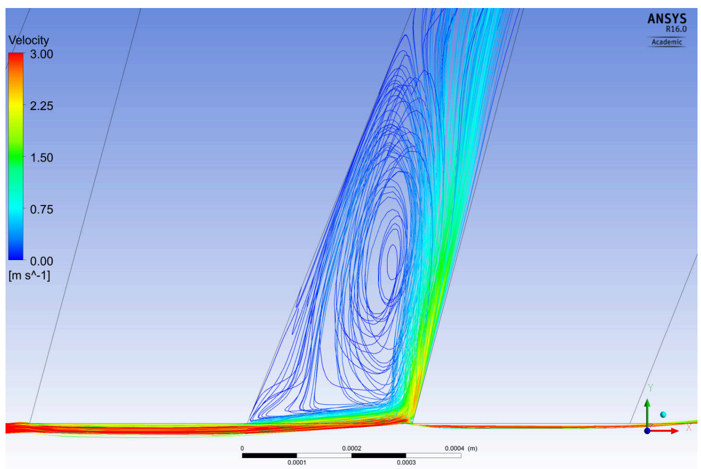

(b) SST flow model

Figure 10.7: Velocity flow paths at the entrance to a small channel from the manifold with a flow rate of 20 ml min^{-1}. Figure a) shows the result for a laminar flow model and b) for the SST model using HFE as fluid.

The thin hybrid sized Kapton layer (16 mm $\times$ 97.5 mm $\times$ 0.025 mm) with 10 rectangular areas on top with the same size as the read out chips on a real hybrid board for the upgraded strip detector in the future endcap petals was modeled on top of the wafer, as shown in figure 10.8. A hybrid represents the board which incorporates the electronic parts needed to read out the sensor. The position and dimensions of the hybrid board and the resistors were adapted very closely, but without taking the glue layer into account. As all measurements were steady state measurements and the 150 µm thick glue layer was assumed to be negligible. The top surface of the resistors on the hybrid were set as heat source.
For a detailed characterization of the micro-channel cooling device, it was equipped with a round heater having the same diameter as the 4 inch wafer. In the simulation the heater was not modelled as additional volume, but a heat flux of 30.8 mW cm^{-2} was set to the outer surface of the Pyrex layer.

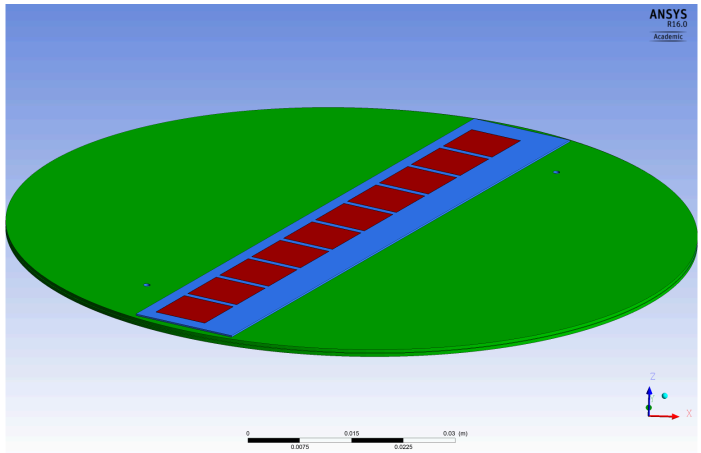

Figure 10.8: The 3d model of the micro-channel device (green) equipped with a thermomechanical hybrid (blue). The ten rectangles (blue) represent the resistors to mimic the heat dissipation of real readout chips.

The inlet temperature of the fluid entering the micro-channels was set to 19 °C. A heat transfer to the environment was not modelled.

Figure 10.9 shows the temperature distribution on the wafer surface for 3 steps of mesh refinements. The mesh was refined from an overall element size of 500 µm for the wafer and 100 µm for the contact surfaces between the fluid and the wafer in a) to 400 µm and 90 µm in b) and down to 300 µm and 80 µm in c). The available computing power prevented a further refinement. The maximal temperature on the wafer is increasing from 21.58 °C in a) up to 21.62 °C in c) and the temperature distribution is slightly changing. The total rise of the maximal temperature of 0.04 °C is negligible, especially considering all the other error sources in the simulation like the deviation from the exact material properties.

Further results of the thermal study are presented in connection with the experimental results in chapter 12.

The same setup was used for a sample with the silicon and Pyrex layer cut to the micro-channel structure. The results of the thermal studies are presented in connection with the experimental results in chapter 12. The dependence of the viscosity on the temperature was not taken into account but fixed to the viscosity at around 20 °C, due to a very small variation of the viscosity inside the temperature range in which the measurements were realized.

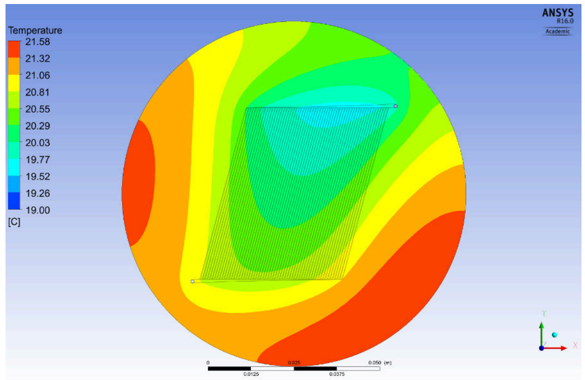

(a)

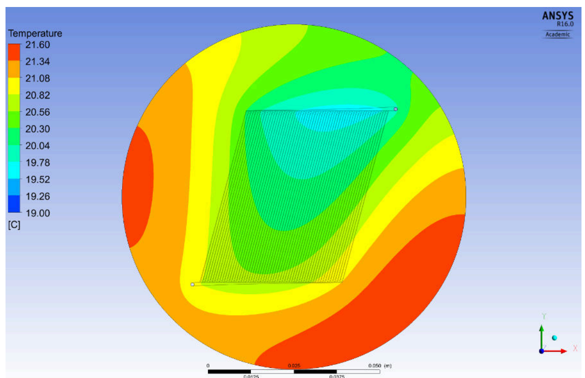

(b)

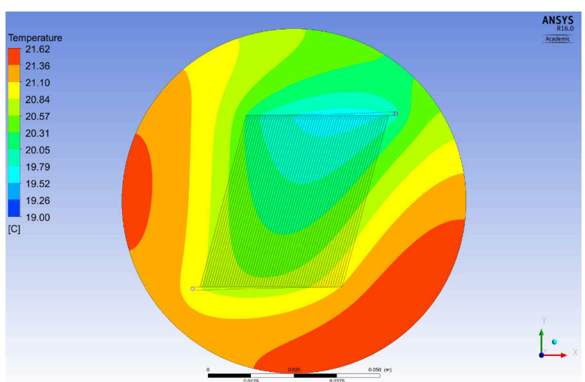

(c)

Figure 10.9: The temperature gradient on the silicon side of the wafer with a heat flux of 30.8 mW cm^{-2} and a flow rate of 50 ml min^{-1}. The mesh was refined from an overall element size of 500 µm for the wafer and 100 µm for the contact surfaces between the fluid and the wafer in a) to 400 µm and 90 µm in b) down to 300 µm and 80 µm in c). An increase of the maximal temperature from 21.58 °C to 21.62 °C is observable towards a finer mesh.

Chapter 11

Test stand for hydrodynamic and thermal measurements

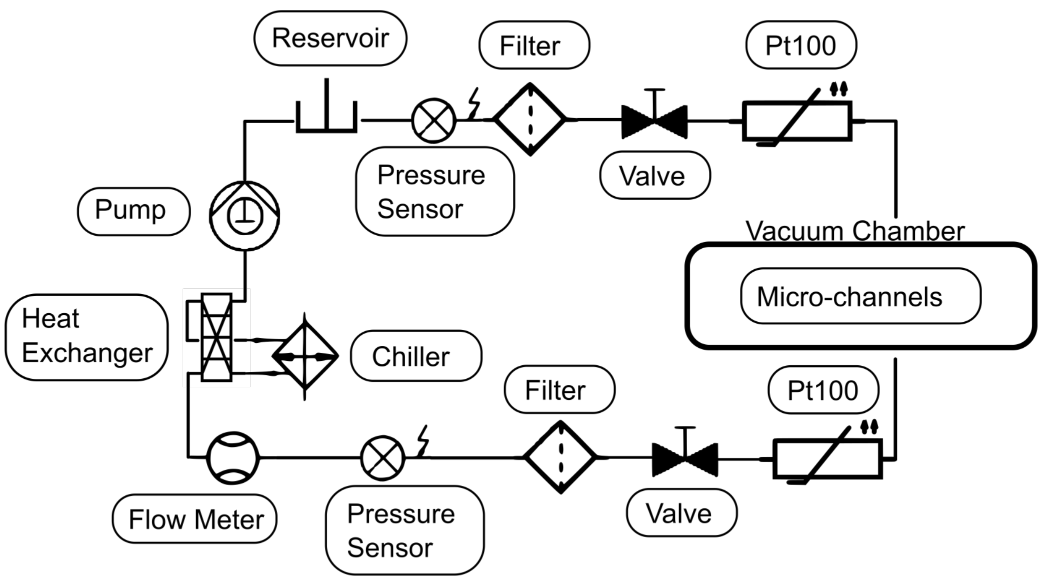

Figure 11.1: Scheme of the setup to determine flow and thermal characteristics of the micro-channel embedded prototypes.

The layout and the production of the micro-channel equipped wafer has already been introduced in section 9. The prototypes were integrated into a test stand providing the possibility of hydrodynamic and thermal measurements. Therefore, numerous devices had to be included suiting the demands of the expected flow rate and pressure. The test stand had to provide control of the flow rate, of the temperature of the fluid flowing through the channels, as well as a way to measure the pressure drop of the device and the temperature at various locations. In the following the setup, which is shown as a scheme in figure 11.1 is described in detail.

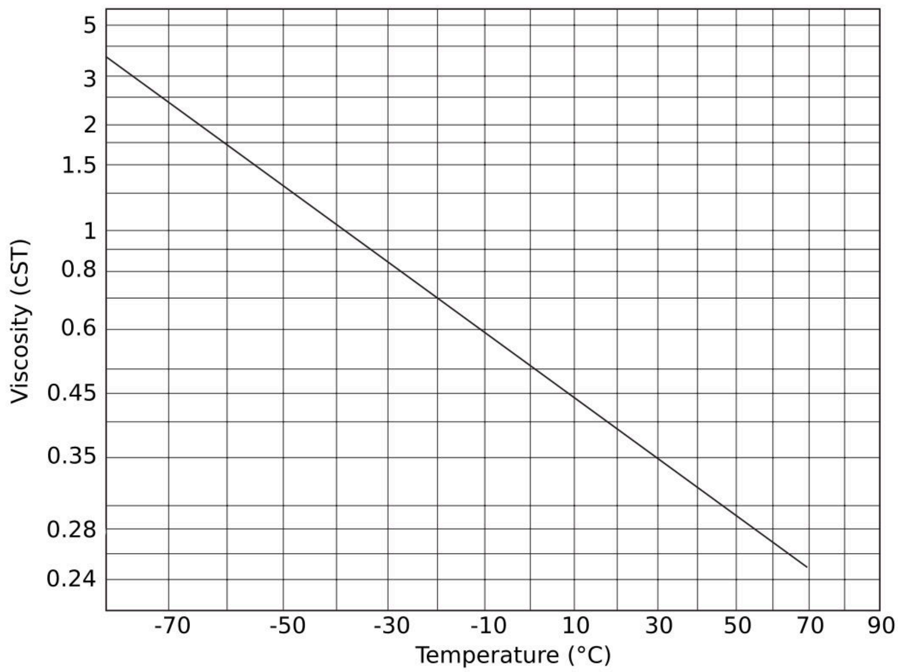

Figure 11.2: Temperature dependence of the kinematic viscosity of HFE, which was used as coolant [75].

11.1 Coolant circuit and devices

A hydro-fluoro-ether [75] providing a low viscosity over a broad temperature range was chosen as coolant. The temperature dependence of the viscosity is shown in figure 11.2. A High Pressure Liquid Chromatography (HPLC) piston pump (ECOM IOTA 300 [76]) is suiting the requirements of a small flow rate with high pressure. It has two pistons connected in parallel with a diameter of 3/8 inch. The flow rate can be set in a range from 1 ml min^{-1} to 300 ml min^{-1} with the pressure being automatically adjusted to provide the desired flow rate up to a maximum pressure of 75 bar.
The pump draws the coolant from a reservoir and pumps it with a certain flow rate through a plate heat exchanger [77], using 1/8 inch stainless steal pipes. The heat exchanger itself is connected to a cooling unit (Huber petite fleur w [78]) to control the temperature of the coolant.
A flow meter (Bronkhorst mini Cori-Flow M14 [79]) capable of also measuring the density and the temperature is located directly after the heat exchanger. A pressure sensor (Swagelok pressure transducer model-s [80]) is installed after the flow meter to obtain a precise pressure measurement.
In order to keep dust and other possible contaminations out of the micro-channels, the first filter (Swagelok 15 µm filter [81]) is integrated in the circuit, which is followed by one of two valves (Swaglok batching valve series-L [82]) to ensure and facilitate interconnectivity.
All devices and additional parts such as the filters and valves as well as the pipe diameters were chosen with the purpose of adding as little additional pressure drop to the setup as possible. In fact the pressure drop of the setup without the micro-channel prototype attached is below 0.05 bar in the

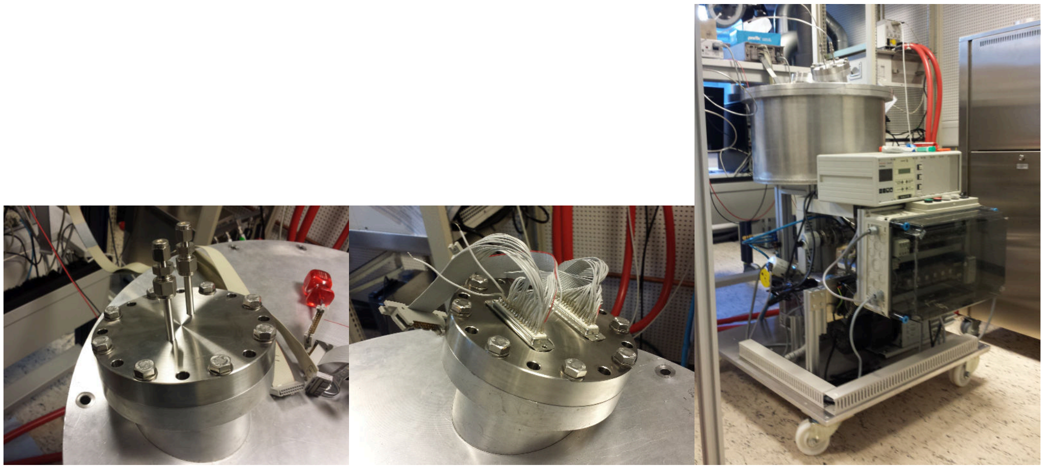

(a) (b) (c)

Figure 11.3: a) The feedthroughs for the coolant, b) the feedthroughs for the Pt100 resistors and the power supply for the heater and c) the full vacuum vessel with the pumps and the control unit.

used flow rate range of 0 ml min^{-1} to 50 ml min^{-1}. Depending on the purpose of the measurement, the coolant pipes are guided into a vacuum chamber or an acrylic glass frame, containing the micro-channel device. The acrylic glass frame holds the device in place to perform measurements with an infrared camera (Infratec VarioCam HD [83]).

The vacuum chamber producing a vacuum pressure of 4 mbar consists of an aluminum vessel with a lid having two exchangeable flanges [84] for feedthroughs. One flange is equipped with feedthroughs for the coolant and the other one with two Sub-D plugs with 50 pins each to connect Pt100 [85] temperature resistors and the power supply for heaters. Figure 11.3 shows both flanges from the top side.

After flowing through the channel structure, the fluid is led through pipes out of the vacuum chamber, passing another valve, another filter and a second pressure sensor before being collected in a reservoir. The filter and valve are implemented to maintain interconnectivity, prevent backflows and contaminations during test stand maintenance.

A picture of the setup can be seen in figure 11.4 showing the pump (green), the heat exchanger (orange), the flow meter (blue), the pressure sensor (red), the filter and the valve (yellow). The transparent cylindrical plastic vessel acts as a reservoir for the coolant.

The pump and the flow meter were connected via their serial communication interface and were controlled using the communication protocol provided by the manufacturers. Due to the fact that the signal of the pressure sensors was analogue, they were connected to the analogue inputs of an Arduino UNO Micro-controller Board [86], which served as a read out board sending the digitized measurement values to the PC. The cooling unit was connected via USB. A Keithley 2700 multimeter [87] equipped with two Keithley 7700 multiplexer modules [88] was utilized to measure the resistance of the Pt100 resistors. A Hameg HM8143 [89] served as power supply for the different heaters used in the thermal studies and described below.

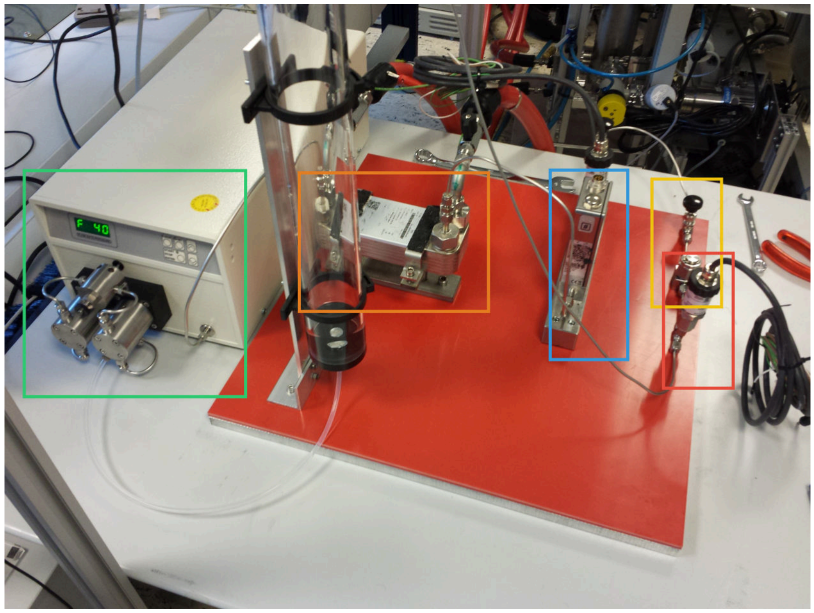

Figure 11.4: Picture of the setup, including the pump (green), the heat exchanger (orange), the flow meter (blue), the pressure sensor (red) and the filter and valve (yellow).

The measurement data of the devices included in the setup was read out via PC using an in-house software - written in C++ [90] and using Qt [91] - to create log files of individual measurements.

11.2 NanoPort connectors and gluing jig

In order to implement the micro-channel embedded wafer into the test facility, connectors had to be used which resist high pressure and feature the possibility of gluing them to silicon to provide a sealed connection. These requirements were fulfilled by PEEK NanoPort connectors [92] for inlets up to a diameter of 1.6 mm, a maximal pressure rating of 69 bar and equipped with 1/16 inch outer diameter tubing connections. The NanoPorts are glued to the silicon with an adhesive ring.
Figure 11.5 shows two NanoPort connectors glued to an anodic bonded 4 inch prototype. The stainless steal pipes in the coolant circuit are converted from 1/8 inch to 1/16 inch to enable the connection to the NanoPort connectors glued to the inlet and outlet of the micro-channel prototype.
A precise alignment of the NanoPort connectors on the inlet and outlet of the micro-channel structure is important to prevent leakage and a blocking of the inlet or outlet. Therefore, a custom jig was designed and built to press the NanoPort connectors on the wafer and is shown in figure 11.6. Holes were drilled in the top bar of the jig to ensure a stable support of the NanoPort connectors. In order to ensure the alignment of the adhesive ring with the PEEK connectors, four small holes where drilled in the jig's top bar. The jig demonstrated a very accurate way to glue the connectors to the silicon without putting the wafer at risk of breaking due to wrongly distributed pressure on the wafer. A spring on each screw of the jig was holding the top bar of the jig in place during the

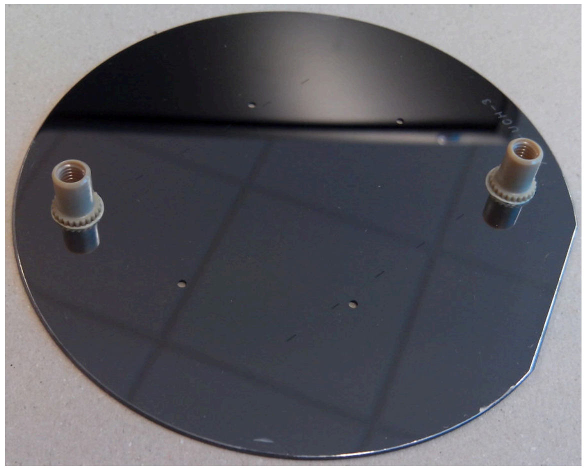

Figure 11.5: Picture of two NanoPorts glued to the inlet and outlet of an anodic bonded 4 inch prototype.

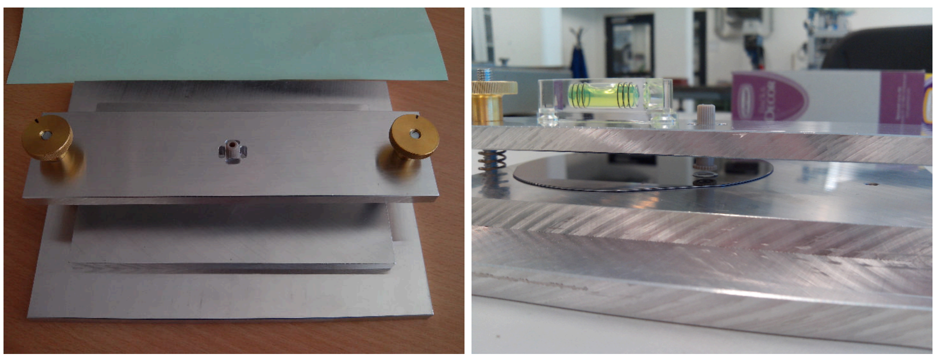

Figure 11.6: Picture of the jig to align and fix the NanoPorts on the prototypes (left) and of the alignment process with a NanoPort mounted in the jig (right).

alignment procedure.

The connectors were glued to the silicon surface with an adhesive ring which was cured at a temperature of around 170 °C for approximately 2 h. Destructive pressure tests with blank wafers were carried out to examine the quality of the glue joint. A hand held pressure test device [93] was used to increase the pressure of water on the NanoPorts and the silicon wafer. It was found that the glue joints did not represent the weak point, but actually withstood more pressure than the silicon wafer. Two attempts were realized and the wafer broke at approximately 50 bar and at 70 bar. This showed that the NanoPort connectors - when properly glued - are withstanding higher pressures than the silicon. The blank wafers were 500 µm thick, which is significantly more than the thickness of the silicon at the inlet of a prototype (see section 9.1).

The prototypes' silicon thickness varied from 300 µm to 500 µm with 100 µm deep channels, causing the stability to differ from prototype to prototype. During data taking at higher flow rates the pressure once exceeded 31 bar and the silicon broke at the inlet, which is shown in figure 11.7. Because the inlet manifold channel shown in figure 9.2 has the maximum width of the structure with

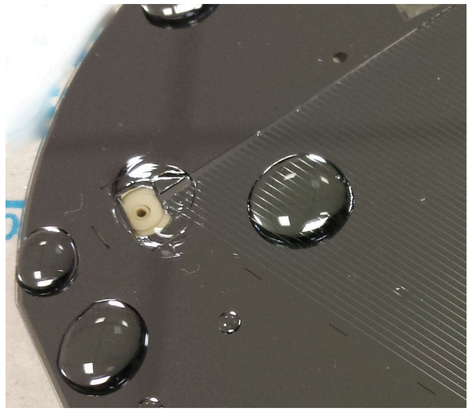

Figure 11.7: Broken silicon wafer due to a pressure increase to 31 bar.

the highest flow rate passing through, this area remains the most fragile part of the structure.

11.3 Temperature measurement devices and heaters

Pt100 temperature resistors were used to measure the temperature of the prototype during thermal tests. Before starting a measurement the resistors were inspected. At a fixed temperature each Pt100 resistor showed a slightly different resistance. The deviations of the temperature resistors from one resistor chosen as reference was used as correction for the others. A Weicon instant adhesive (contact VA100 [94]) was utilized to attach the Pt100 resistors to the Pyrex wafer surface.

Some prototypes were heated with a thin 4 inch self adhesive heater mat [95] with etched foil elements embedded into a glass cloth supported rubber compound and some with a custom made 3d printed heater mat. Latter one is further described in section 12.2.4.

In order to obtain an overview of the temperature distribution across the full wafer surface, in some cases an infrared (IR) camera was attached over the prototype. The IR camera was fixed to a cage surrounding the table with the setup and the micro-channel device, providing the possibility to block thermal radiation from other heat sources by shielding the experiment with a curtain.

Chapter 12

Experimental Results

In order to characterize the different prototypes in terms of hydrodynamic and thermal properties, a range of measurements were realized. This section includes flow measurements in section 12.1 and thermal measurements in section 12.2.
The results of pressure drop measurements are presented in section 12.1.1 and flow path measurements with fluorescent tracer particles in section 12.1.2. A precise knowledge of the pressure drop development with different flow rates is crucial to stay below a critical pressure. Weak points in the channel layout in terms of unwanted turbulence creation or other effects could cause additional pressure drops and may influence the flow homogeneity.
The thermal characteristics of an anodic and an eutectic bonded 4 inch micro-channel device obtained with Pt100 resistors and a thermal camera in air are presented in section 12.2.2. These measurements are important to determine the cooling power of the micro-channel device and to compare with the results of the simulation.
Section 12.2.3 presents the results of similar measurements of an eutectic bonded prototype in air and a vacuum, which is helpful to visualize the effect of free convection appearing in air and suppressed in a vacuum.
The final section 12.2.4 of this chapter shows the measurements with a thermal camera of a cut eutectic bonded prototype. The wafer was cut to the geometry of the micro-channel structure to avoid the effect of a surplus of material on the temperature of the prototype at the outer regions of the channel structure.
Table 12.1 shows all prototypes used in this work and their properties.

12.1 Flow studies

Measurements of the hydrodynamic properties of the device are indispensable to verify its general usability in terms of sufficient mass flow for acceptable pressure drops regarding its mechanical

Table 12.1: Table of all prototypes and their properties used in this thesis.

Name	Bonding type	Diameter	Thickness	Identification
Sample A	Anodic	4 inch	Si=300 µm, Pyrex=500 µm	A-U2-1
Sample B	Anodic	4 inch	Si=500 µm, Pyrex=500 µm	A-U3-2
Sample C	Eutectic	4 inch	Si=500 µm, Pyrex=500 µm	E-U2-1
Sample D	Eutectic	cut	Si=500 µm, Pyrex=500 µm	E-U3-1
Sample E	Anodic	cut	Si=500 µm, Pyrex=500 µm	A-U4-2

stability. Moreover, it is important to investigate the flow paths through the channel layout to search for possible weak points in terms of regions with turbulent flows or misrouted flows.

12.1.1 Pressure drop measurements

As indicated in figure 11.4, the pressure was measured shortly before and after the coolant flows through the micro-channels. The pump regulated the pressure so that it is zero at the exit of the circuit. The metal pipes as well as the devices built into the loop did not contribute measurably to the pressure drop of the full setup. This was tested and confirmed with pressure measurements of the circuit without integrating the micro-channel device.
The volumetric flow rate was set from 6 ml min^{-1} to 40 ml min^{-1} to obtain the corresponding pressure drop from inlet to outlet. The flow rate was chosen in that range because the pressure sensors were not capable to reliable measure the pressure at very low pressure values occurring below 6 ml min^{-1}.
Figure 12.1 shows the dependence of the pressure drop on the flow rate for two anodic bonded prototypes - samples A and B - and two eutectic bonded prototypes - samples C and D.
At 40 ml min^{-1} the pressure values for all prototypes are still far away from reaching a critical value of around 30 bar (see section 11). The pressure for samples A, B and D is almost on the same level throughout the flow rate range of 6 ml min^{-1} to 40 ml min^{-1}, whereas the eutectic bonded prototype C shows a much lower pressure drop.
The pressure needed to maintain a certain flow rate is an indication for possible differences between the prototypes due to the production process or contaminations in the channels. The gold layer covering one side of the channels in the eutectic bonded samples C and D effects the flow, due to a different surface roughness and a different chemical interplay with the coolant.

It is unlikely that the eutectic sample C is the only one behaving correctly, which would indicate, that the samples A, B and D accidentally contain contaminations or artifacts produced during the fabrication yielding almost exactly the same pressure increase. In addition the anodic bonded samples A and B were visually examined through the Pyrex cover and no evidence of contaminations or empty channels were found.

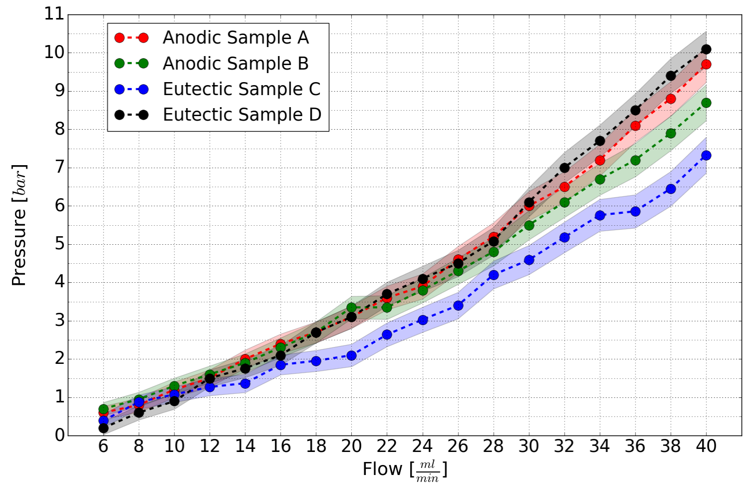

Figure 12.1: Pressure drop versus flow rate for 4 different prototypes, two anodic bonded prototypes and two eutectic bonded prototypes.

As a conclusion sample C can be classified as malfunctioning due to an issue during fabrication. There are a number of possibilities what could have caused this behavior. The bonding of the wafers is a crucial procedure and sometimes air enclosures are produced during both bonding methods used here. The enclosures lead to non-ideal sealing of the channels and cause fluid traversing to neighboring channels. When not perfectly applied the gold layer yields another weak point of the eutectic bonding process, which can cause the same effect.

The analysis of the thermal characteristics provided more insight to the homogeneity of the flow and is presented in section 12.2.2.

12.1.2 Flow measurements with fluorescent particles

In order to detect potential weak points in the design of the micro-channel structure a study of the stream through the channel array was performed using Fluoro-Max dyed green aqueous fluorescent particles [97] with a diameter of 1 µm and 0.5 µm and the anodic bonded cut sample E. The setup included the pump, a filter, a valve, an anodic bonded prototype of the micro-channel device and an inverted Nikon eclipse Ti confocal microscope [98].

The confocal principle is shown in figure 12.2. The fluorescent particles have an absorption peak at 468 nm and an emission peak at 508 nm. A beam splitter with two suitable filters was used, one for a range from 457 nm to 492 nm and one for a range from 508 nm to 551 nm. The first filter only lets the desired excitation wave length through and blocks all other wave lengths coming from a light source. After passing the filter the light is focused by a lens to a focal plane and the sample. The light emitted by the fluorescent particles is then guided through the second filter blocking all wave lengths outside the filter spectrum, and is collected by a light detector. A magnification scale of 20 was used throughout the measurements. The tracer particles were diluted in water with a concentration of around 1:5000, at which the signal was good to spot the stream lines.

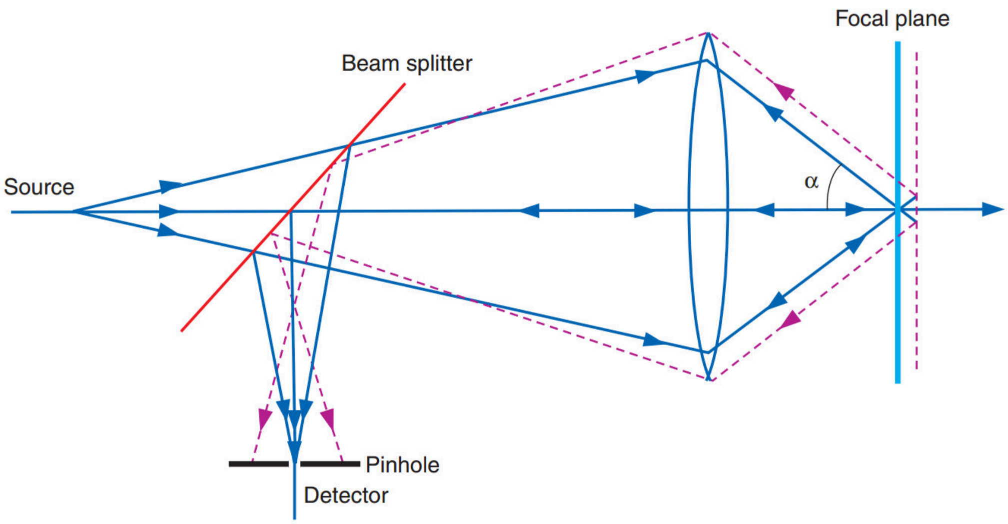

Figure 12.2: Principal of a confocal microscope [96]. The solid lines represent the light that is coming from the focal plane and later detected. The dashed lines represent the light that is coming from outside of the focal plane and blocked by the pinhole. The beam splitter works with two filters for different wave lengths to block the light outside the emission peak of the object under investigation.

The measurements were started with a flow rate of $1\,\mathrm{ml\,min^{-1}}$. In total thirteen channels stayed without flow at that flow rate, although the channels without flow were already filled at the time the behavior was observed. A possible explanation for that behavior is a pressure created by the fluid from the end of the channels. Since the channel structure was already filled, the fluid in the output manifold is creating a pressure at the channel outlets against the desired flow direction and prevents the fluid to enter from the inlet manifold into some channels.
This was reproducible with random channels and different channel numbers being affected, but only after the channel structure was completely filled first. The effect was not observed in the simulation and is not related to the empty channels that appeared in the multiphase simulation, which stayed completely dry. At a flow rate of $2\,\mathrm{ml\,min^{-1}}$ the fluid was flowing through all channels and no channels without flow were observed anymore.
Flow rates up to $20\,\mathrm{ml\,min^{-1}}$ were tested and compared. Especially the flow behavior at the transition from the manifold to the channels was changing with the flow rate. A flow separation was observed in this area caused by the corners of the channel entries like it was already observed in the simulation (see figure 10.7). It was observed that the vortex is growing towards higher flow rates after being created at around $3\,\mathrm{ml\,min^{-1}}$. Although, the small channels were tilted by about 15° in respect to the manifold axis and the channel ends were widened to avoid this effect, it appears strongly (see 12.3, 12.4 and 12.5).
The fluorescent particles proved to be a useful technique to analyze the flow in critical regions of the channel layout. At flow rates above $2\,\mathrm{ml\,min^{-1}}$ no evidence of smaller velocities at channel entries

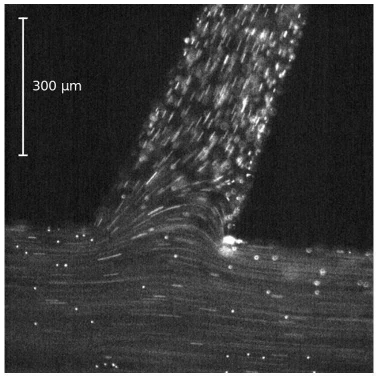

(a) 1 ml/min

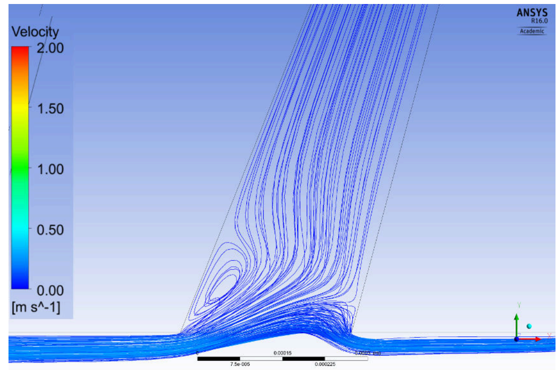

(b) 1 ml/min

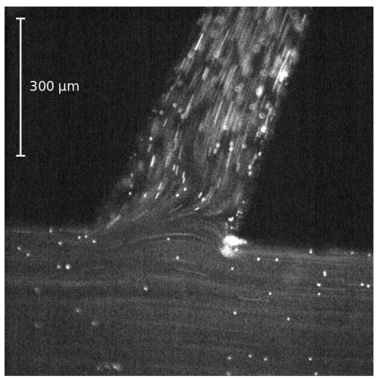

(c) 2 ml/min

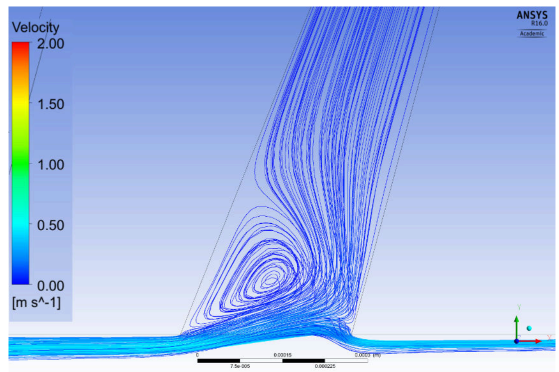

(d) 2 ml/min

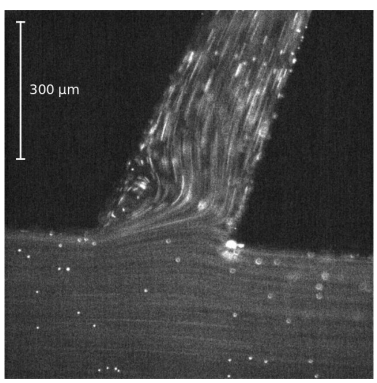

(e) 3 ml/min

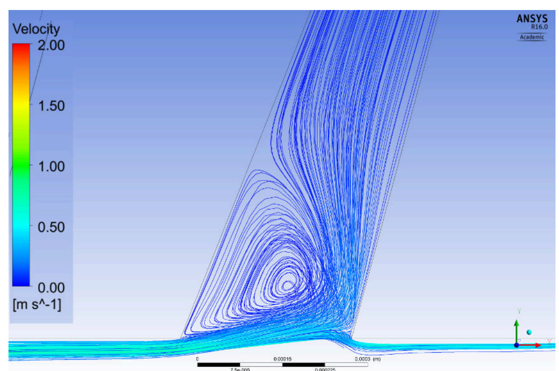

(f) 3 ml/min

Figure 12.3: Velocity streamlines at the entrance to a small channel from the manifold with a flow rate of $1\,\mathrm{ml\,min^{-1}}$ to $3\,\mathrm{ml\,min^{-1}}$. Figure a), c) and e) show the result of the fluorescent tracer measurement and b), d) and f) for the laminar model in the simulation.

could be observed by comparing the vortex sizes between the channel entries, indicating less mass flow through certain channels. At a fixed flow rate the vortexes in the channel entries had the same size in all channels, which indicates a homogeneous flow.

As presented in section 10.3.1.1, three different flow models were tested in the simulation: a laminar model, a k-ϵ model and a SST model. The results of the calculations using the laminar and

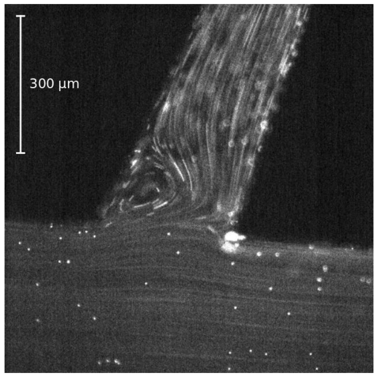

(a) 4 ml/min

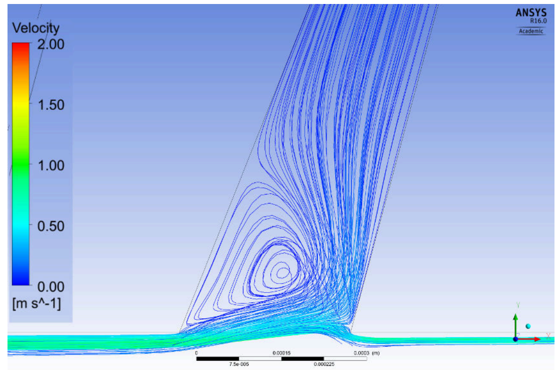

(b) 4 ml/min

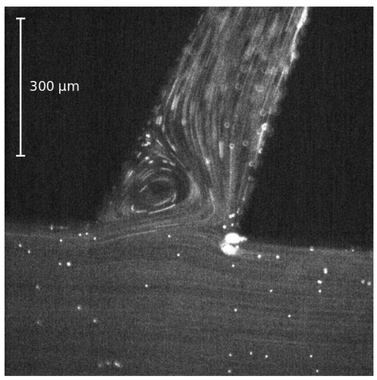

(c) 5 ml/min

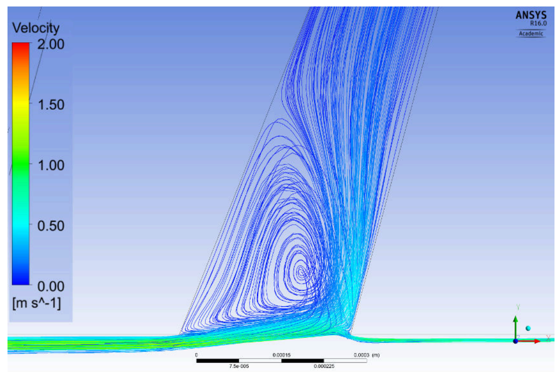

(d) 5 ml/min

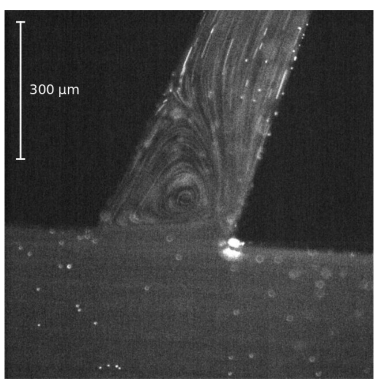

(e) 10 ml/min

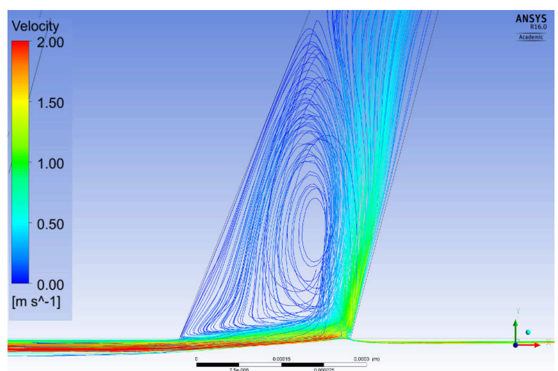

(f) 10 ml/min

Figure 12.4: Velocity streamlines at the entrance to a small channel from the manifold with a flow rate of $4\,\mathrm{ml\,min^{-1}}$ to $10\,\mathrm{ml\,min^{-1}}$. Figure a), c) and e) show the result of the fluorescent tracer measurement and b), d) and f) for the laminar model in the simulation.

the SST flow model were in a good agreement, but the k-ϵ model showed a different behavior. At the same time, the observations of the flow in the prototype utilizing fluorescent tracers showed a similar behavior as in the simulated laminar and SST model.

In the following, the flow in the channel entry is compared between the experiment and the simulation for flow rates ranging from $1\,\mathrm{ml\,min^{-1}}$ to $20\,\mathrm{ml\,min^{-1}}$. Figures 12.3, 12.4 and 12.5 show the

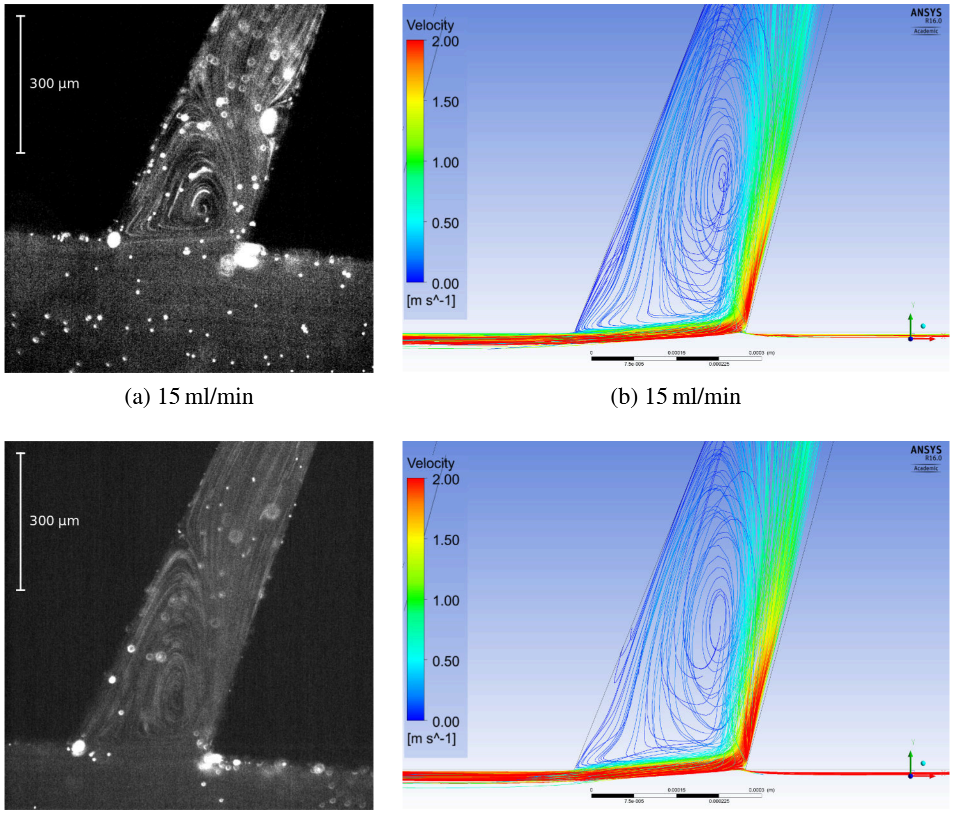

(a) 15 ml/min (b) 15 ml/min

(c) 20 ml/min (d) 20 ml/min

Figure 12.5: Velocity streamlines at the entrance to a small channel from the manifold with a flow rate of $15\,\mathrm{ml\,min^{-1}}$ to $20\,\mathrm{ml\,min^{-1}}$. Figure a) and c) show the result of the fluorescent tracer measurement and b) and d) for the laminar model in the simulation.

flow measurements in the prototype and the simulation using the laminar flow model side by side with the same flow rate. The vortex generation starts at a flow rate of $3\,\mathrm{ml\,min^{-1}}$ in the experiment, but appears from the start in the simulation. In both cases the vortex is created very close to the entry directly after the fluid enters the channel. The vortex in the simulation is stretched a bit more along the channel axis towards higher flow rates but the area of the recirculating flow is growing with increasing flow rates in both.

Unfortunately the flow velocity could not be calculated in the fluorescent measurements due to the high velocities and the sub-optimal filter properties of the microscope leading to an exposure time of 2 ms. As can be seen in the figures 12.3, 12.4 and 12.5 showing the fluorescent tracer measurements, it is not possible to calculate the particle speed by measuring the length of the line it creates due to the exposure time. The dependence of the particle speed on the location in the channel due to the distinct velocity profile in the channels would make the determination even harder.

The simulation shows that the fluid is reaching its minimum velocity in the vortex. This area is growing as the flow rate increases, which is causing a pressure increase in each channel by slowing down the flow at each entry and reducing the effective width of the channel entry.

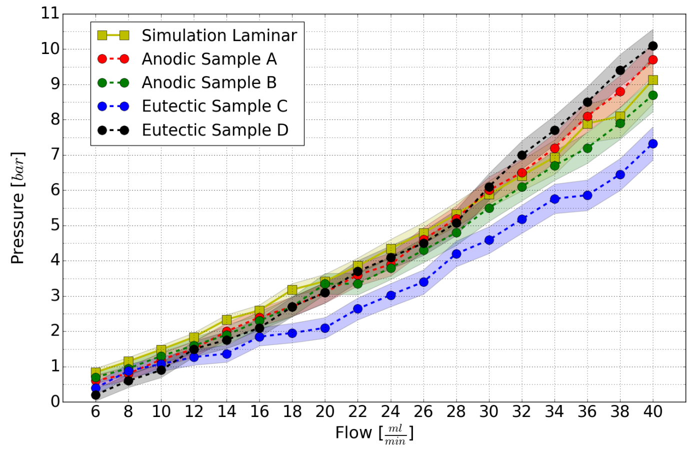

(a)

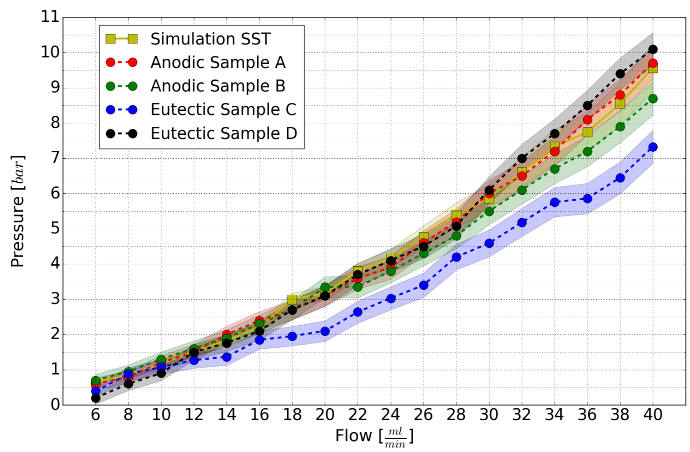

(b)

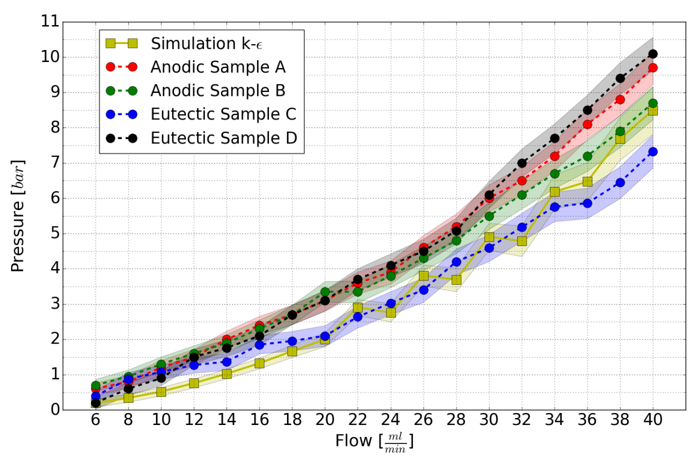

(c)

Figure 12.6: Pressure drop versus flow rate comparison for all prototypes and the laminar flow model a), the SST flow model b) and the k-ϵ flow model c) in the simulation.

In the following a comparison of the pressure drop versus flow rate between different flow models in the simulation (see figure 10.6) and different prototypes in the experiment (see figure 12.1) is presented. This study is aiming at investigating whether including the possibility of turbulent flow in the simulation provides a result that suits the experimentally obtained results better.
Figure 12.6 a), b) and c) show the three different flow models of the simulation compared to the measurements of the four different prototypes. The laminar and the SST flow model show a very good agreement with two of the anodic bonded prototypes A and B and the eutectic bonded prototype D, whereas the k-ϵ model is fitting better to the eutectic bonded prototype C.
The error band on the experimental data represents the area around the measurement points, which includes 95% of the pressure drop measurement data taken during several runs. The error in the simulated data is obtained through the mesh refinement and is a fit of the remaining fluctuations as described in section 10.3.1.
The experimentally gained results agree very well with the simulation using the laminar model and the SST model with the laminar model having a shorter computing time.

Thermal tests were carried out to investigate the effect of the flow behavior on the cooling capabilities. A change in the pressure drop and thus the flow behavior in the channel structure could also affect the fluid distribution. Thermal tests are a good way to detect such discrepancies between the prototypes and the simulation and are presented in the next section. The thermal tests were carried out with the samples A and C, without the knowledge of the different behavior.

12.2 Thermal measurements

Three approaches were realized to study the cooling performance of the micro-channel device.
In the first approach, a thermo-mechanical hybrid, which served as a dummy of a real hybrid holding the readout electronics, was glued to the silicon side of the 4 inch sample B. Resistors embedded on the hybrid were heating the sample mimicking the heat dissipation of real readout chips. The results of the temperature measurements are presented in section 12.2.1.
In another approach the device was equipped with an adhesive silicone heater mat with the same size as the 4 inch wafer (see section 12.2.2) to provide a homogeneous heating of the full wafer surface. The measurements are compared to the simulation. The buildup was realized with the anodic bonded sample A and repeated with the eutectic bonded sample C (see section 12.2.3). The latter one was used to compare the thermal behavior in air and a vacuum to investigate the effect of free convection.
Sample D, which was cut to the size of the micro-channel structure, was equipped with a custom heater and investigated with a thermal camera (see section 12.2.4) to study the effect of a surplus of material.

12.2.1 Anodic bonded wafer equipped with a thermo-mechanical hybrid

A thermo-mechanical hybrid with the same size and heat dissipation as a real hybrid for future endcap modules was utilized to observe the behavior of the micro-channel cooling device. It can give an idea of the cooling performance in a realistic case. Hence this setup can be seen as a proof of concept to cool a realistically shaped heat source in a particle detector.

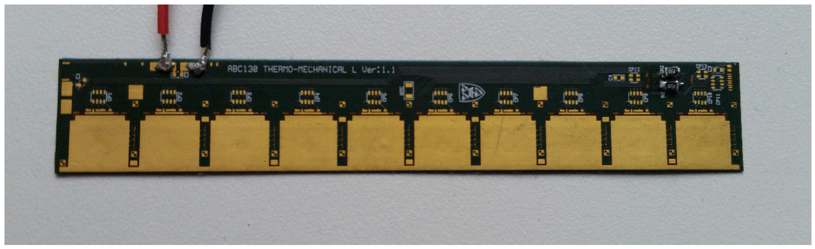

Figure 12.7: Thermo-mechanical hybrid board equipped with ten resistors connected in series, emulating the heat dissipation of read out chips of a real hybrid.

The hybrid shown in figure 12.7 is equipped with ten square shaped embedded resistors of $0.3\,\Omega$ connected in series having the same size as the asics on a functional hybrid. These are meant to emulate the heat dissipation of read out chips of a real hybrid. In order to emulate the heat of the Hybrid Controller Chip (HCC), two additional resistors are soldered to the hybrid board. The thermo-mechanical hybrid provided a power dissipation of around $1.14\,\mathrm{W}$ resulting in a power density of $170\,\mathrm{mW\,cm^{-2}}$ with an applied voltage of $2\,\mathrm{V}$.

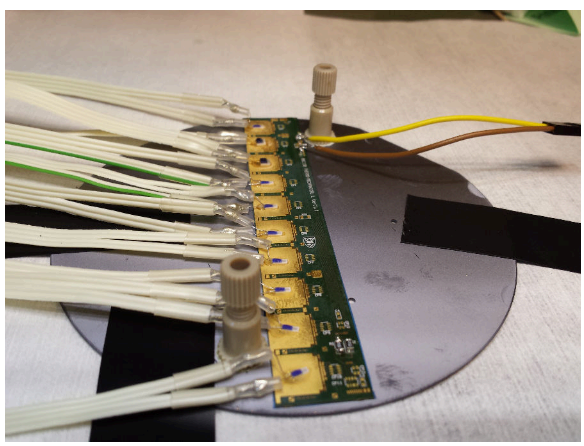

Figure 12.8: Thermo-mechanical hybrid board glued on a micro-channel embedded wafer, equipped with ten Pt100 resistors to measure the temperature along the board, of which eight were used. Two Pt100 resistors were needed for measuring the inlet and outlet temperature and are not shown here.

In order to keep the glue between the thermo-mechanical hybrid and the micro-channel sample B at an even thickness, a mask was constructed to deposit an epoxy glue film with known height on the hybrid's backside. Although the effect of the glue layer on the measurement was assumed to be negligible, the thickness was held as constant as possible along the hybrid length in order to

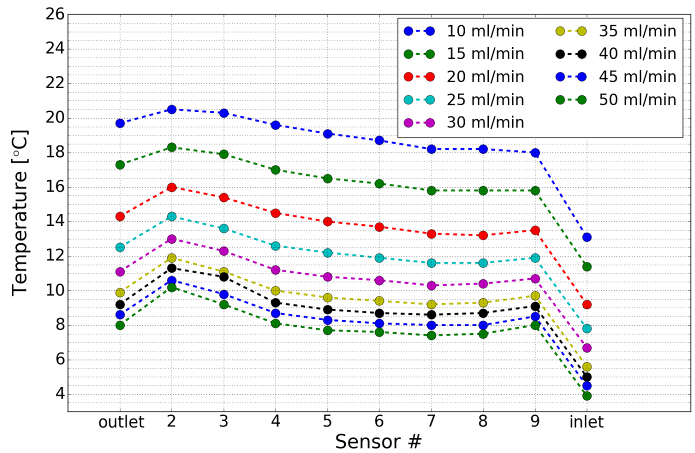

Figure 12.9: Temperature along the thermo-mechanical hybrid measured with Pt100 resistors. The resistors to measure the temperature of the fluid at the inlet and outlet are placed directly on the pipes, whereas the other temperature sensors were placed on the resistors of the hybrid.

have a homogeneous thermal conductance. To measure the temperature at each build-in resistor, ten Pt100 resistors were glued with epoxy to the board as shown in figure 12.8 of which only eight were used due to a limited read out channel number of the Keithley multiplexer. The Pt100 resistors were pressed down to the board while the glue cured to provide an optimal connection between the resistors on the board and the Pt100.

The temperature of the chiller was set to $-5\,°C$ resulting in a maximum coolant temperature at the inlet of $13.1\,°C$ for a flow rate of $10\,\mathrm{ml\,min^{-1}}$ and a minimum temperature of $3.9\,°C$ for a flow rate of $50\,\mathrm{ml\,min^{-1}}$. The temperature of the measured positions on the hybrid is shown in figure 12.9.

The temperature distribution on the hybrid is as expected and shows an increase from the inlet towards the outlet. The coolant heats up while transporting the dissipated power of the hybrid resistors out of the system. The difference between the curves of the temperature measurements on the hybrid for different flow rates shows a saturating effect towards higher flow rates. Sensor 2 and sensor 9 are located at the outer regions of the channel layout and are not cooled as much as the other ones. This is reflected by the temperature measured with sensor 2 and 9 with different flow rates. The temperature is decreasing less than at the positions equipped with Pt100 sensors in-between sensor 2 and 9.

This was the first indication of the micro-channel device being capable to maintain a small temperature gradient on a heated structure with a heat load comparable to a realistic application in a HEP detector and without risking to break the device due to high pressure.

12.2.2 Adhesive heater on anodic and eutectic bonded prototype in air

Adhesive heater mats [95] with a diameter of 4 inch were attached to the backside of the anodic bonded sample A and the eutectic bonded sample C to provide a homogeneous heat flow across the

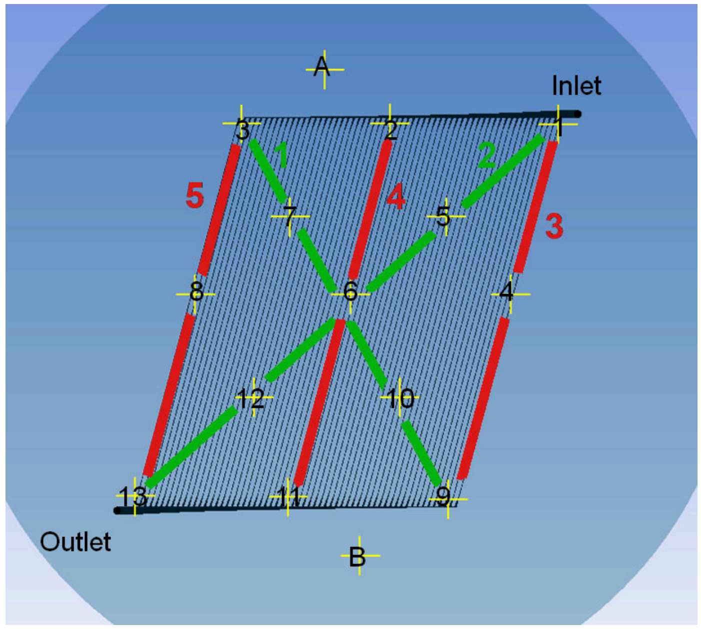

Figure 12.10: The Pt100 resistors arranged on the wafer surface across the micro-channel structure. Two diagonal lines (green) connecting resistors 3, 7, 6, 10 and 9 and 1, 5, 6, 12 and 13, and three lines (red) connecting resistors 1, 4 and 9, 2, 6 and 11 and 3, 8 and 13 are marked.

full wafer. The homogeneity of the heat distribution was tested beforehand by means of an infrared camera and was found to be good.

The heater was set to heat fluxes of 30.8 mW cm^{-2}, 43.1 mW cm^{-2}, 55.5 mW cm^{-2} and 67.8 mW cm^{-2} corresponding to 2.5 W, 3.5 W, 4.5 W and 5.5 W across the full wafer surface to compare the cooling performance of the prototypes. The chosen heat loads are based on the heat dissipation of a future micro-strip module for the ATLAS detector. The module with the sensor and the readout electronics is estimated to dissipate about 2.5 W. To investigate the behavior of the prototypes at higher heat loads, they were more than doubled to a maximum of 5.5 W.

A thermal camera [83] was used to measure the overall temperature distribution across the wafers. To obtain more precise temperature values at certain positions on the wafer, thirteen Pt100 resistors were placed on the same side as the inlet and outlet connectors of the micro-channel device. The positions of the Pt100 resistors are shown in figure 12.10.

Two differences between the two samples which have to be considered are the materials of the top layers and the thickness of the silicon layers with the embedded channels. The latter one is 300 µm thick in sample A and 300 µm thick in sample C.

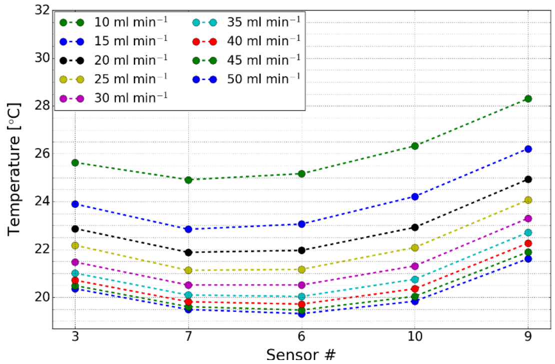

(a) Line 1 on the anodic bonded sample.

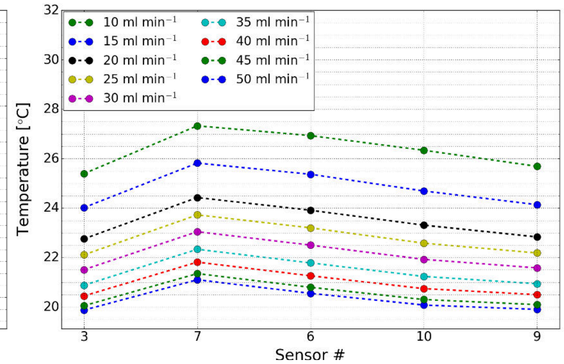

(b) Line 1 on the eutectic bonded sample.

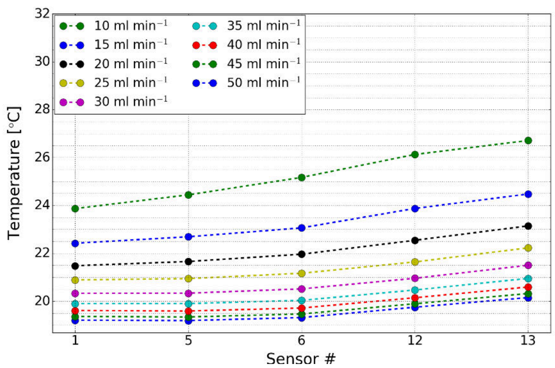

(c) Line 2 on the anodic bonded sample.

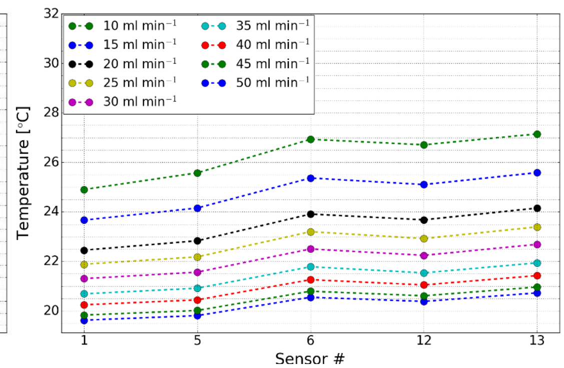

(d) Line 2 on the eutectic bonded sample.

Figure 12.11: Temperature along line 1 and line 2 for a heat flux of 30.8 mW cm^{-2} on the anodic and the eutectic bonded prototype.

12.2.2.1 Measurements with Pt100 resistors

For a better visualization of the temperatures measured across the structure, Pt100 resistors along lines (see figure 12.10) were combined in five plots. As the measurements were steady state measurements, the small amount of glue used to support the Pt100 resistors was assumed to not affect the results.

The plots in figure 12.11 a) and c) show the diagonals across the channel array (lines 1 and 2 in figure 12.10) of the anodic bonded sample A. Especially sensor 9 on line 1 shows an increased temperature compared to the other sensors due to its remote location at the edge of the channel layout. The flow rate was set from 10 ml min^{-1} to 50 ml min^{-1} in 5 ml min^{-1} steps. A saturation effect is clearly visible in the temperature measurements with increasing flow rate. This means that a good part of the cooling power of the device and the coolant is reached at flow rates which do not put the device at risk of breaking. Furthermore, one would only gain little performance by increasing the flow rate beyond 50 ml min^{-1}. The shapes of the curves in figures 12.11 a) and c) do not indicate any hot spots. A region with a significantly higher temperature would be denoted as a hot spot. It could be caused by channels without flow or a general inhomogeneous flow distribution. A single

empty channel affects the flow distribution, but is not assumed to have a measurable effect on the sample temperature.
The difference of the maximal temperature and the minimal temperature on line 1 is 3.02 °C at a maximum flow rate of 50 ml min^{-1}, and the difference on line 2 is 1.66 °C. The diagonals contain points affected by different layout properties. Line 2 contains both inlet and outlet whereas the other one contains the Pt100 resistors at the top left and bottom right edge of the channel array with less flow compared to the inlet and outlet region. These properties explain the temperature differences on the diagonals.
Figure 12.11 b) and d) show the diagonals across the channel array of the eutectic bonded sample C. It is clearly visible that the temperature distribution along the two diagonals show a very different behavior compared to the anodic bonded sample (figure 12.11 a) and c)). Especially sensors 6 and 7 on the eutectic prototype show a different behavior. The tested eutectic prototype is the one that showed a different pressure drop in the flow analysis in section 12.1.1. The problem influencing the pressure drop appears to influence also the temperature distribution across the micro-channel structure of the eutectic bonded prototype. The pressure drop is decreased in this prototype probably due to channels which are not properly sealed by the top wafer. These leakages could cause a transfer of the fluid to a neighboring channel and disturb the homogeneity of the flow distribution. However, the location of the problem can not be precisely specified without investigating the inside of the micro-channel device. The measurements can only provide the test for a malfunctioning device in general.
Figure 12.12 a), c) and e) show the three lines along the channels in flow direction as indicated in figure 12.10 on the anodic bonded sample. On line 3 the maximal temperature difference is 2.40 °C, on line 4 1.16 °C and on line 5 0.71 °C with a flow rate of 50 ml min^{-1} and a power dissipation of 30.8 mW cm^{-2}. Again, the temperature development along the lines does not give any hints to a region with a significantly higher temperature. Everything points to a homogeneous flow distribution across the micro-channel structure. The three lines vertical to the manifold axis give an indication of the region in which the flow distribution changes the most. Compared to the results of the eutectic bonded prototype in figure 12.12 b), d) and f), especially the region around sensor 9 on line 3 and sensor 11 on line 4 show a different behavior as the mentioned sensors measured a lower temperature, indicating that a defect is located in the bottom right corner of the micro-channel layout opposite to the outlet causing more flow in that region.

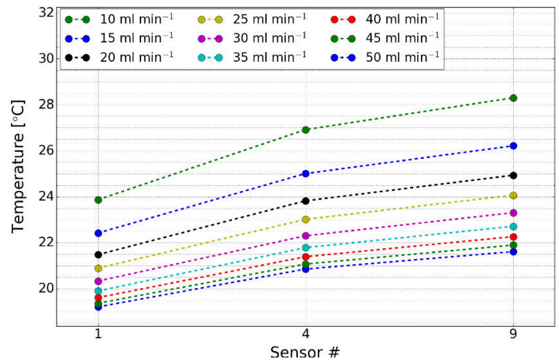

(a) Line 3 on the anodic bonded sample.

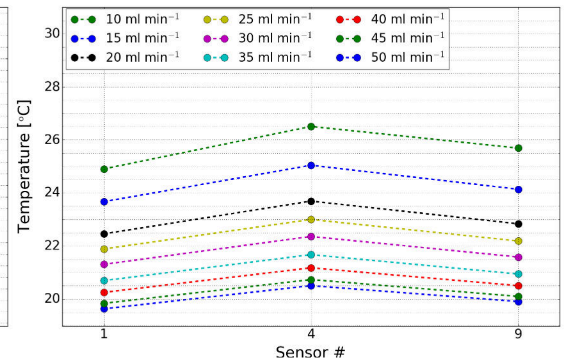

(b) Line 3 on the eutectic bonded sample.

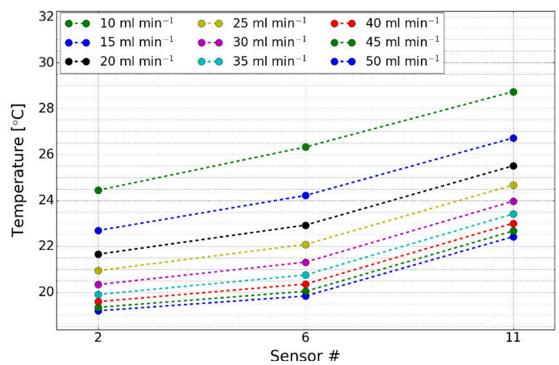

(c) Line 4 on the anodic bonded sample.

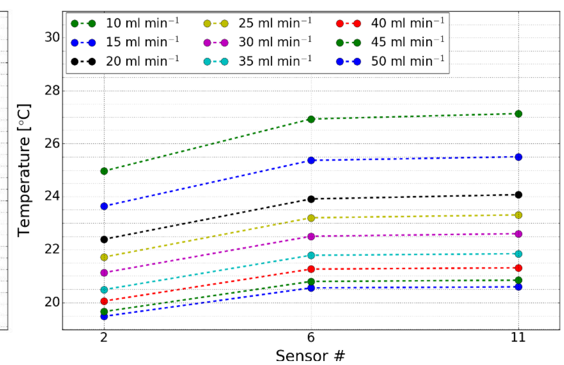

(d) Line 4 on the eutectic bonded sample.

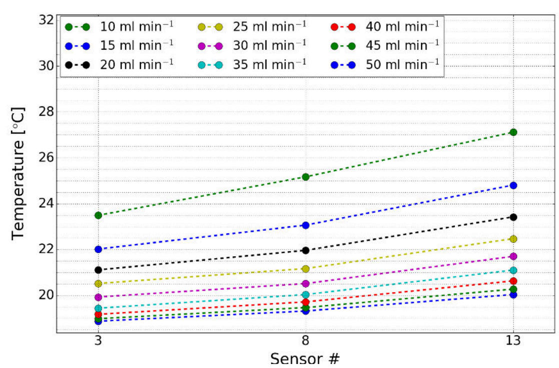

(e) Line 5 on the anodic bonded sample.

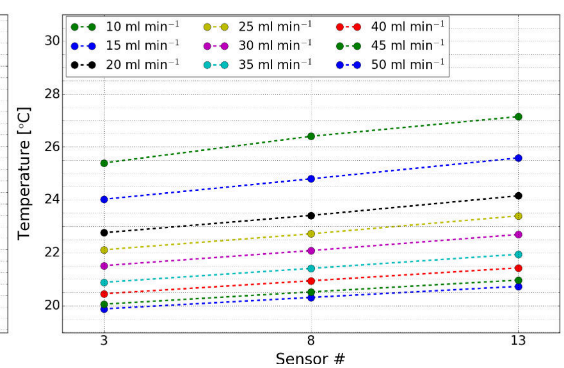

(f) Line 5 on the eutectic bonded sample.

Figure 12.12: Temperature along line 3 in a) and b), the temperature along line 4 in c) and d) and the temperature along line 5 in e) and f) for a heat flux of 30.8 mW cm^{-2} on the anodic and the eutectic bonded prototype, respectively.

12.2.2.2 Measurements with Pt100 resistors compared with the simulation

The device was simulated and the temperature probed at the same positions as in the experimental setup. In the following the results of the simulation of both bonding methods are compared to the experimental results. The only differences between the simulations of the anodic and the eutectic bonded sample is the material of the top layers, which is made from Pyrex for the anodic bonded

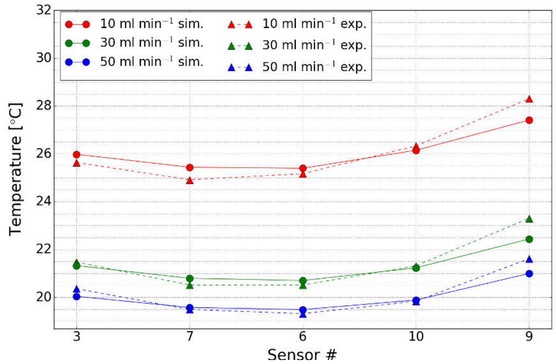

(a) Line 1 on the anodic bonded sample and in the simulation.

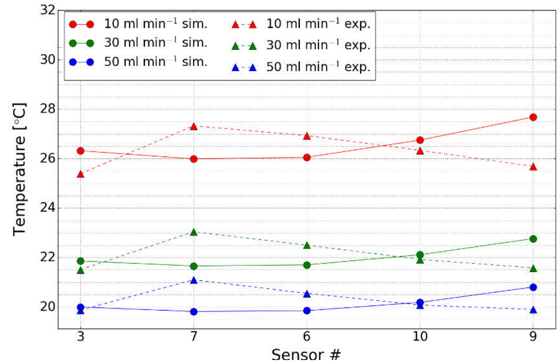

(b) Line 1 on the eutectic bonded sample and in the simulation.

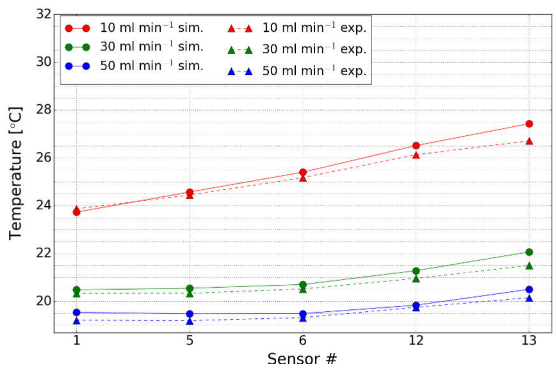

(c) Line 2 on the anodic bonded sample and in the simulation.

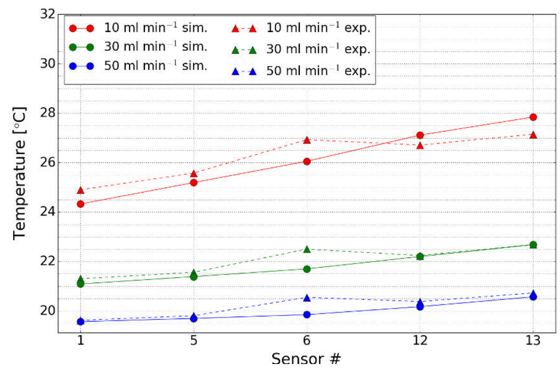

(d) Line 2 on the eutectic bonded sample and in the simulation.

Figure 12.13: Temperature along line 1 a) and b) and line 2 c) and d) for a heat flux of 30.8 mW cm^{-2} on the anodic and eutectic bonded prototype, respectively, for the simulation and the experiment.

prototype and from silicon for the eutectic bonded prototype, the thicknesses of the bottom layers with the embedded channels and the loss to the environment, which is not taken into account in the simulation. The different thermal conductivity of the two materials will influence the temperature distribution on the prototypes. The thermal conductivity of silicon is 150 W mK^{-1} and of Pyrex only 1.3 W m^{-1} K^{-1}.

Figure 12.13 a) and c) show the temperature of the simulation and the anodic bonded sample A on the diagonals named line 1 and line 2 for flow rates from 10 ml min^{-1} to 50 ml min^{-1} and a heat flux of 30.8 mW cm^{-2}. The agreement of the two lines between simulation and experiment is very good and the biggest discrepancy appears at sensor 9 at the bottom right corner of the channel layout. The agreement between the simulation and the experiment is slightly better for higher flow rates due to small deviations from the exact position of the sensor in the simulation. For lower flow rates the gradient across the surface is larger and hence the different positioning of the sensors has a greater effect on the measurement.

The same small discrepancy becomes visible by looking at the plots in figure 12.14 a), c) and e) showing the results for lines 3 to 5 on the anodic bonded sample. Due to the very small deviation of

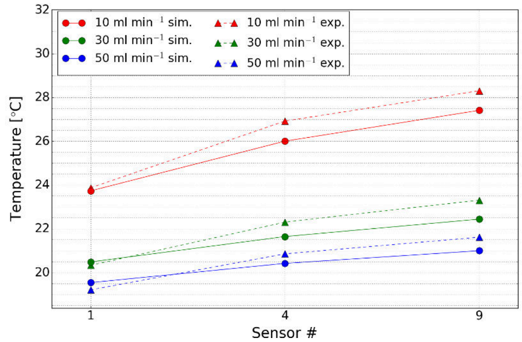

(a) Line 3 on the anodic bonded sample and in the simulation.

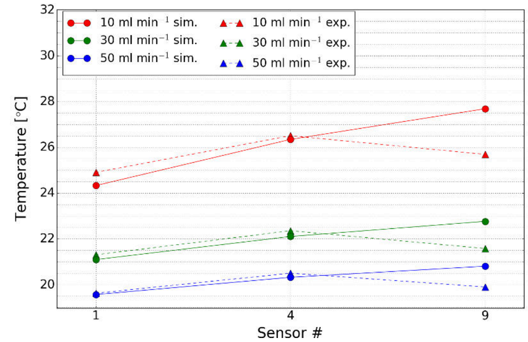

(b) Line 3 on the eutectic bonded sample and in the simulation.

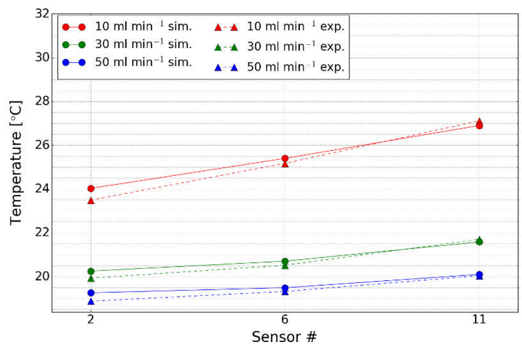

(c) Line 4 on the anodic bonded sample and in the simulation.

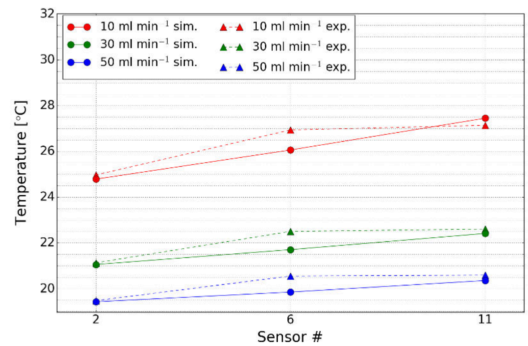

(d) Line 4 on the eutectic bonded sample and in the simulation.

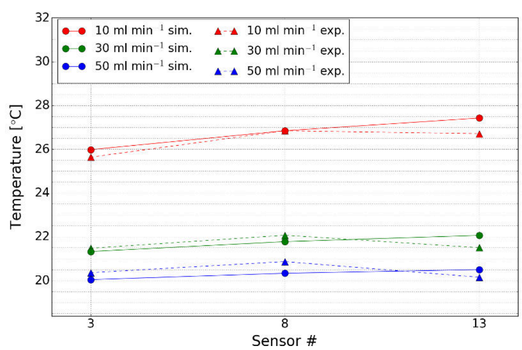

(e) Line 5 on the anodic bonded sample and in the simulation.

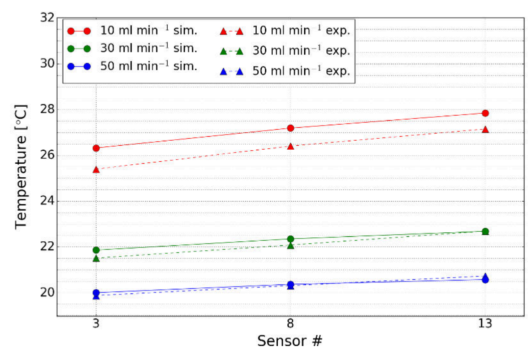

(f) Line 5 on the eutectic bonded sample and in the simulation.

Figure 12.14: Temperature along line 3 a) and b), line 4 c) and d) and line 5 e) and f) for a heat flux of 30.8 mW cm^{-2} on the anodic and eutectic bonded prototype, respectively, for the simulation and the experiment.

the results of the simulation from the experiment, a further optimization of the simulation was not considered necessary. In the experimental setup, the temperature of the coolant was varying with different flow rates, whereas the inlet temperature in the simulation was fixed. The results of the experimental setup were corrected for these differences measured at the inlet.

A comparison of the lines 1 to 5 on the eutectic bonded prototype is shown in figure 12.13 b) and

d) and in figure 12.14 b), d) and f). The previously observed discrepancy between the experimental results of the temperature measurements with the anodic and the eutectic prototype is also visible in the comparison of the experimentally gained results with the eutectic sample with the simulation. Another difference which becomes apparent by comparing the plots in figure 12.14 a), c) and e) to the plots b), d) and f) is the increasing discrepancy towards lower flow rates between the simulation and the eutectic bonded prototype results. This discrepancy is not observable in such a great extent in the comparison of the simulated and the experimental results of the anodic bonded prototype.
The higher thermal conductivity has a larger effect on the temperature rise of the device at lower flow rates. In principle the missing heat transfer via free convection or radiation to the ambient air in the simulation leads to a higher temperature of the sample in the simulation, but this is not visible due to the overall small discrepancy between the simulation and the experimental results. The plot with the best agreement is the one showing line 5 in figure 12.14 f).

12.2.2.3 Measurements with a thermal camera

An overview of the temperature distribution was obtained with a thermal camera. This method is not as accurate as the measurements with the Pt100 resistors in terms of absolute temperatures, because the relation of the thermal radiation emitted by silicon to its temperature represented by the emission factor (see equation 8.19) was not known for the anodic and eutectic bonded prototype. The performed measurements were not used for precision measurements, but for a qualitative comparison with the results of the thermal simulation.
Figure 12.15 shows the results of the measurements with the thermal camera on the anodic bonded sample A and the simulation side by side for flow rates of $10\,\mathrm{ml\,min^{-1}}$, $30\,\mathrm{ml\,min^{-1}}$ and $50\,\mathrm{ml\,min^{-1}}$ and a heat dissipation of $30.8\,\mathrm{mW\,cm^{-2}}$. The NanoPort connectors and the pipes block the sight of some parts of the wafer surface. The big advantage of the contour plots shown in figure 12.15 is the possibility to visualize the isotherms. Dividing the wafer surface into regions with the same temperature range makes the flow distribution and thus the heat transport visible. Both results of the experiment and the simulation are in a good agreement regarding the shape of the isotherms and the temperature range on the wafer surface, as expected from previous comparisons of the Pt100 measurements.

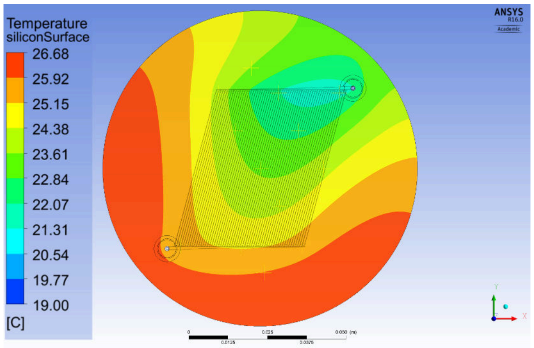

(a) Simulation with the anodic bonded sample with a flow rate of 10 ml min^{-1}.

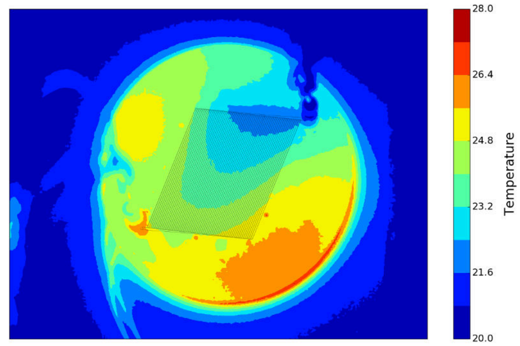

(b) Experiment with the anodic bonded sample with a flow rate of 10 ml min^{-1}.

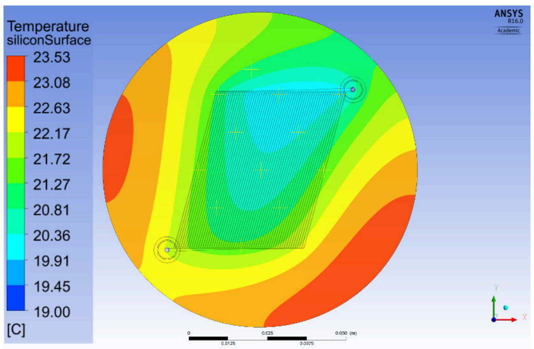

(c) Simulation with the anodic bonded sample with a flow rate of 30 ml min^{-1}.

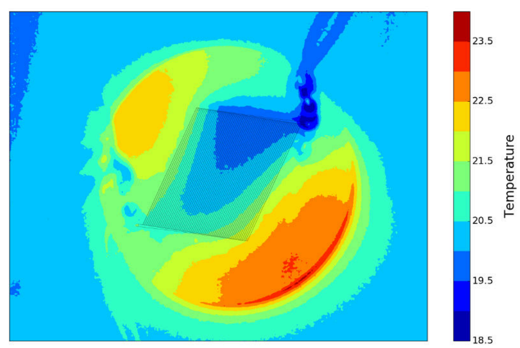

(d) Experiment with the anodic bonded sample with a flow rate of 30 ml min^{-1}.

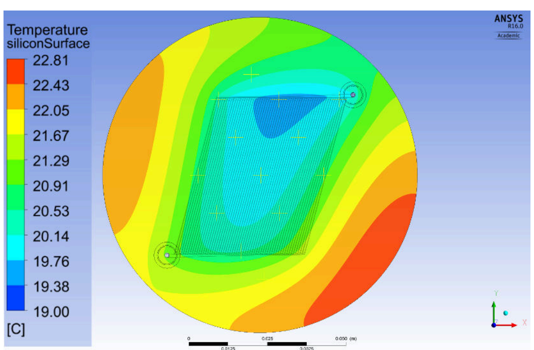

(e) Simulation with the anodic bonded sample with a flow rate of 50 ml min^{-1}.

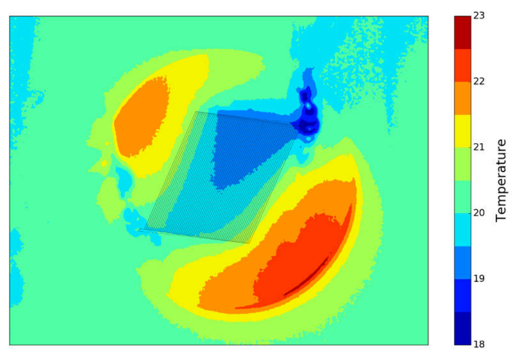

(f) Experiment with the anodic bonded sample with a flow rate of 50 ml min^{-1}.

Figure 12.15: The simulated results in a), c) and e) and the experimental results in b), d) and f) of the measurements of the anodic bonded prototype obtained with a heat flux of 30.8 mW cm^{-2} and a flow rate of 10 ml min^{-1}, 30 ml min^{-1} and 50 ml min^{-1}.

Figure 12.16 shows the results of the measurements of the eutectic bonded sample C performed with the IR camera. The higher conductivity of the silicon layer used in the eutectic bonding process leads to a different temperature distribution on the wafer surface. The heat dissipated by the heater is distributed more effectively through the wafer and is absorbed by the coolant to a greater fraction compared to the anodic bonded prototype with the Pyrex layer. The discrepancies that were

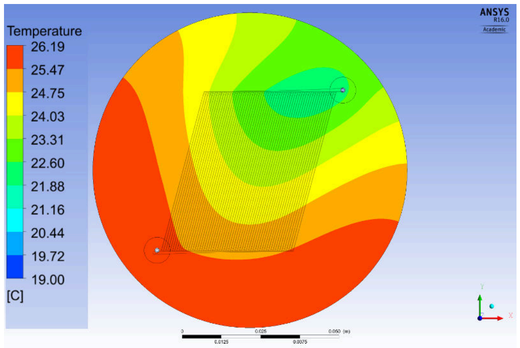

(a) Simulation with the eutectic bonded sample with a flow rate of 10 ml min^{-1}.

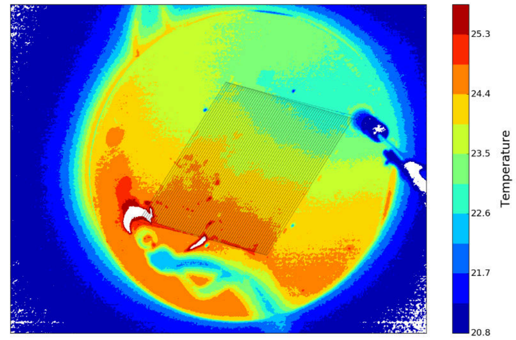

(b) Experiment with the eutectic bonded sample with a flow rate of 10 ml min^{-1}.

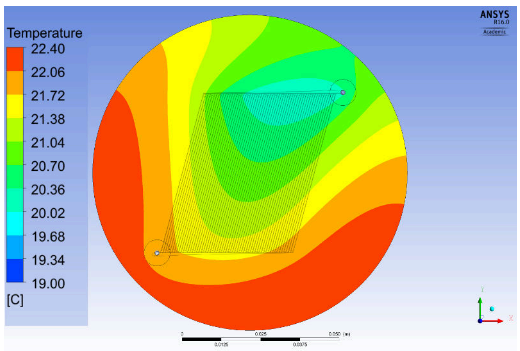

(c) Simulation with the eutectic bonded sample with a flow rate of 30 ml min^{-1}.

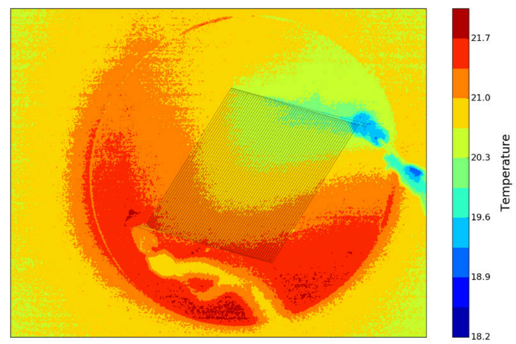

(d) Experiment with the eutectic bonded sample with a flow rate of 30 ml min^{-1}.

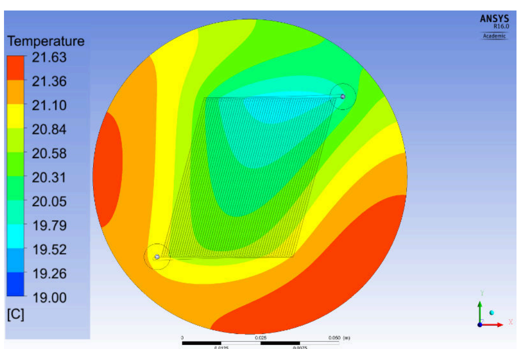

(e) Simulation with the eutectic bonded sample with a flow rate of 50 ml min^{-1}.

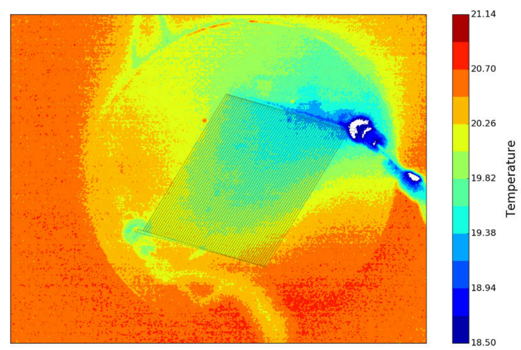

(f) Experiment with the eutectic bonded sample with a flow rate of 50 ml min^{-1}.

Figure 12.16: The simulated results in a), c) and e) and the experimental results in b), d) and f) of the measurements of the eutectic bonded wafer obtained with a heat flux of 30.8 mW cm^{-2} and a flow rate of 10 ml min^{-1}, 30 ml min^{-1} and 50 ml min^{-1}.

observed during the hydrodynamic measurements and the thermal measurements with the Pt100 resistors are not noticeable in the pictures taken with the thermal camera.

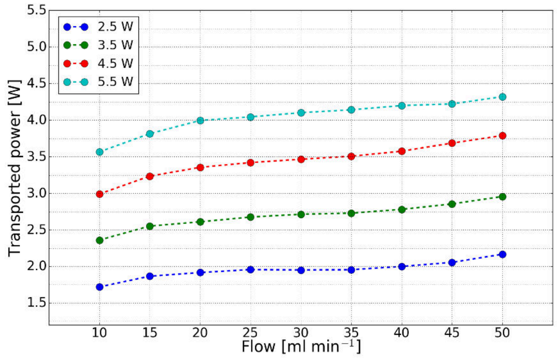

(a) Anodic bonded prototype

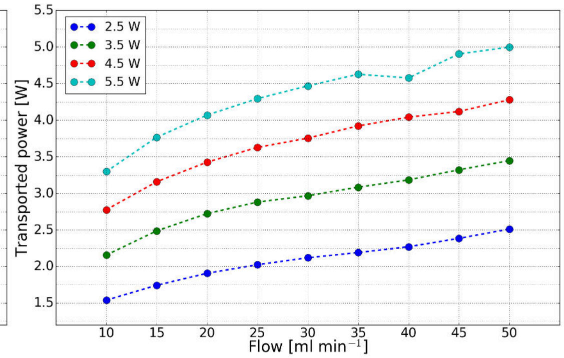

(b) Eutectic bonded prototype (the data point for 5.5 W and 40 ml min^{-1} is an outlier due to a faulty temperature measurement)

Figure 12.17: Heat transported by the coolant for flow rates ranging from 10 ml min^{-1} to 50 ml min^{-1} and heat fluxes from 30.8 mW cm^{-2} to 67.8 mW cm^{-2} for the anodic a) and the eutectic bonded prototype b).

12.2.2.4 Transported heat and thermal resistance

A way to determine the heat transported by the coolant out of the sample is by measuring the difference of the fluid temperature at the outlet and the inlet. The power set to the heater is not the actual power removed by the fluid, because the heater and the wafer also transfer heat to the environment through free convection and radiation, as well as conduction into the power supply cables, the Pt100 resistors and the NanoPort connectors. The losses are influenced by the thermal properties of the materials, especially the layer sealing the micro-channels, which is made of Pyrex or silicon. The measurement of the temperature difference of the coolant between the inlet and the outlet and the coolant specifications can be used to calculate the heat q_r transported by the fluid

$$q_r = f \cdot \rho \cdot C_p \cdot \Delta T, \tag{12.1}$$

with f the volumetric flow, ρ the density of the fluid, C_p its specific heat capacity and ΔT the difference between the temperature of the coolant at the inlet and at the outlet. For HFE at approximately 20 °C the density is ρ=1580 kg m^{-3}, C_p=1170 J kg^{-1} K^{-1}.

The cooling power based on formula 12.1 for different flow rates for the anodic bonded prototype is shown in figure 12.17 a) and for the eutectic bonded prototype in figure 12.17 b). The power removed by the coolant is not increasing linearly with the flow rate using the anodic bonded sample A. All curves have a plateau at around 30 ml min^{-1} and a small rise again at a flow rate of around 45 ml min^{-1}, indicating a change of the heat transfer in that flow rate region. The temperature of the prototype using flow rates around 20 °C to 40 °C is matching the temperature of the environment, whereas the temperature of the prototype using flow rates above and below is either lower or higher than the environmental temperature. If the temperature of the sample is higher than the ambient temperature, free convection plays a bigger role. When the temperature of the sample reaches temperatures below the ambient temperature heat from the environment can be transfered into the fluid. This effect is reflected in the start and end of the curves in figure 12.17 a).

Although the eutectic prototype showed a different flow distribution and pressure drop, the tested flow rates are the same for both prototypes. The shape of the curves in figure 12.17 b) is steeper than in a) due to the much higher thermal conductivity of the silicon top of sample C. Another contributing factor is the gold layer between the silicon wafers in the eutectic bonded sample, however, this effect should be negligible and q_r should be a comparable property. The plateau is visible in 12.17 b), but because of the steepness in a much smaller extend.

The difference between the transported heat q_r out of the anodic bonded prototype and the preset heat load of the heater shown in figure 12.17 a) is increasing with the heat load of the heater. At the maximal flow rate of 50 ml min^{-1} the difference grows from 0.33 W with the heater set to 2.5 W (13.2 %), 0.54 W with the heater set to 3.5 W (15.43 %), 0.71 W with the heater set to 4.5 W (15.78 %) to 1.17 W with the heater set to 5.5 W (21.27 %). Higher heat loads are leading to higher temperatures of the wafer and the heater and hence higher losses due to heat transfer to the surrounding air and to other materials. At the same time, the Pyrex is acting as a thermal boundary damping the heat transfer into the coolant. Accordingly, the difference between the heat transported by the fluid and the preset heat load for the eutectic prototype is smaller than those of the anodic bonded one. It changes from –0.01 W with the heater set to 2.5 W (-0.4 %), 0.05 W with the heater set to 3.5 W (1.43 %), 0.22 W with the heater set to 4.5 W (4.89 %) to 0.50 W with the heater set to 5.5 W (9.09 %).

This comparison of the plots in figure 12.17 shows that the losses caused by the low thermal conductivity of the Pyrex layer are higher. The Pyrex acts as a thermal bridge hindering the heat transport into the fluid and silicon. In addition, the heat deposited in the outer regions of the wafer surrounding the micro-channel layout is not conducted into the actively cooled regions as efficiently as for a device made fully out of silicon.

The measurements of the transported heat with the eutectic bonded sample C at a preset heater power of 2.5 W (–0.01 W) indicate that additional heat is transfered to the fluid. This becomes possible when the wafer reaches a temperature below the ambient temperature, which was measured to be inside a range of 20 °C to 22 °C, and heat is transferred from the ambient into the wafer.

The difference of the mean temperature of the wafer surface in the area of the channel structure $\overline{T_s}$ and the mean fluid temperature $\overline{T_f}$ for a heat flow q_r can be utilized to characterize the heat sink by its thermal resistance

$$R = \frac{\overline{T_s} - \overline{T_f}}{q_r}. \tag{12.2}$$

The thermal resistance is understandable as the reciprocal of the thermal conductivity and describes the ability of the device to maintain a certain temperature in contact with a certain heat load.

To suppress the effect of surplus material surrounding the micro-channel structure apparent in measurements with the Pt100 resistors at the outer borders of the channel structure, only the sensors in the middle of the channel structure were taken into account (Pt100 resistors 5, 6, 7, 10 and 12 in

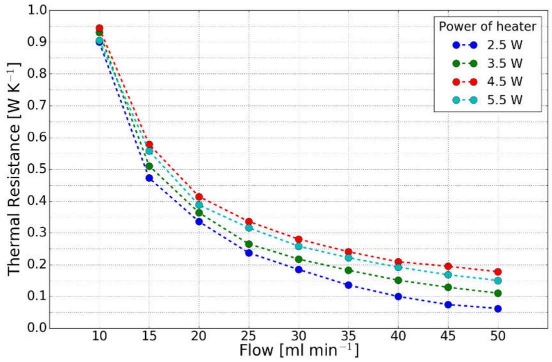

(a) Anodic bonded prototype

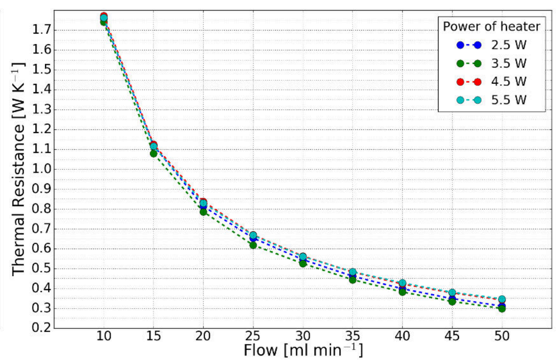

(b) Eutectic bonded prototype

Figure 12.18: Thermal resistance R for a heat load of 30.8 mW cm^{-2} to 67.8 mW cm^{-2} for the anodic and the eutectic bonded prototype.

figure 12.10).

The thermal resistance for different flow rates and heat loads is shown in figure 12.18. The inlet temperatures of all thermal resistance measurements were adjusted to the one during the measurements with a heat load of 30.8 mW cm^{-2}. A saturation effect is visible towards higher flow rates, indicating that the gain in cooling can not be increased much.

In figure 12.18 a) showing the measurements of the anodic bonded prototype the difference between the thermal resistance for different heat loads is increasing with higher flow rates, which is caused by the low thermal conductivity of the Pyrex causing a large uncertainty in the measurement of the thermal resistance. Thus it is not due to a real effect but due to an increasing error in the measurement.

How the difference between the measurements for different heat loads is related to the effect of free convection to the environment will be further discussed in the next chapter, where the measurements are performed in a vacuum.

12.2.3 Adhesive heater on eutectic bonded prototype in a vacuum

The same measurements with Pt100 resistors as described in section 12.2.2 were repeated with the eutectic bonded sample C in a vacuum. The measurements were performed in a vacuum and in air to unveil the effect caused by free convection to the environment. The measurements were performed without the knowledge of the malfunction.

12.2.3.1 Measurements with Pt100 resistors

Figure 12.19 a) and 12.19 b) show the temperature development along the two previously defined lines 1 and 2 across the wafer. It is visible that the surface temperature of the wafer measured in

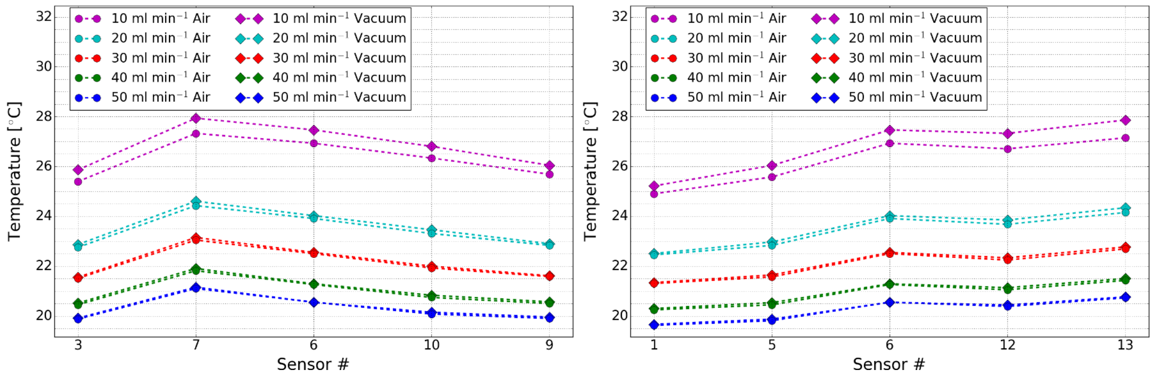

(a) Line 1 (b) Line 2

Figure 12.19: Temperature along line 1 and 2 measured in air and in a vacuum at a heat flux of 30.8 mW cm^{-2}.

a vacuum is higher than the one in contact with air for low flow rates around 10 ml min^{-1}. Instead of partially being transferred to the surrounding air by free convection, the heat can only be transferred to the NanoPort connectors, the Pt100 resistors and the coolant or via thermal radiation. The difference is becoming smaller for increasing flow rates, and is negligible from flow rates starting at 30 ml min^{-1}. The more the prototype is cooled to lower temperatures the smaller is the effect of free convection to the surrounding, as the driving force is the temperature difference between the prototype and the environment. The disturbed flow distribution has already been discussed in the previous section.

Figure 12.20 shows the three lines 3 in a), 4 in b) and 5 in c). Again, the discrepancy between the measurement in a vacuum and air is clearly visible and is decreasing towards higher flow rates. The effect of the free convection to the environment depends on the ambient temperature, which was around 21 °C. The closer the temperature of the prototype gets to the ambient temperature, the smaller is the effect of the heat transferred from the prototype to the environment. In particle detectors the sensors are usually cooled below 0 °C and in some experiments to −25 °C. When the micro-channel device reaches such low temperatures the influence of the ambient on the measurements is much bigger. Sensors in detectors are usually not operated in a vacuum thus other effects occurring in low temperature ranges must be taken into account like moisture due to condensation. The difference between the ambient temperature will be much higher and with increasing difference, cooling will become harder.

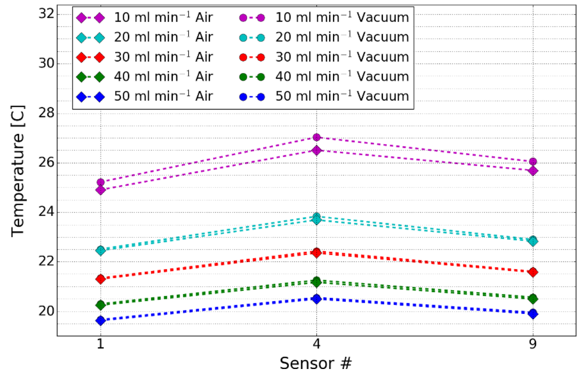

(a)

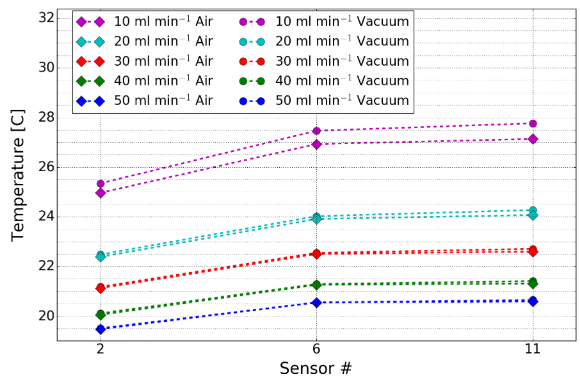

(b)

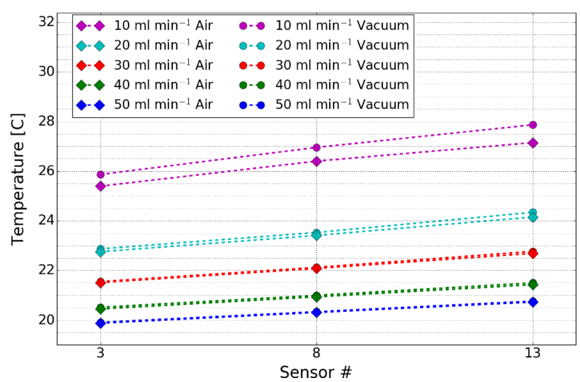

(c)

Figure 12.20: Temperature along line 3 in a), the temperature along line 4 in b) and the temperature along line 5 in c) for a heat flux of 30.8 $\mathrm{mW\,cm^{-2}}$.

The heat transported by the fluid, based on equation 12.1, is shown in figure 12.21 for flow rates of 10 $\mathrm{ml\,min^{-1}}$ to 50 $\mathrm{ml\,min^{-1}}$. The heat transported out of the device in the measurements performed in a vacuum are higher throughout all flow rates. The differences between the measurements are decreasing with higher flow rates. With increasing flow rates and decreasing temperature difference between the prototype and the ambient temperature, the contribution of the free convection to the slope in figure 12.21 becomes smaller. The outlier at a flow rate of 40 $\mathrm{ml\,min^{-1}}$ and a heat load of

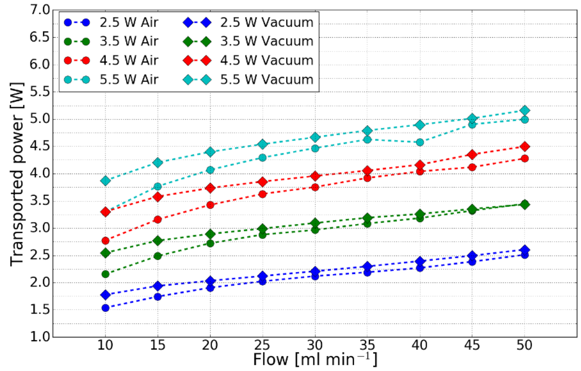

Figure 12.21: Heat transported by the coolant for flow rates ranging from 10 ml min^{-1} to 50 ml min^{-1} and heat fluxes from 30.8 mW cm^{-2} to 67.8 mW cm^{-2} measured in air and a vacuum.

5.5 W is due to a faulty measurement - caused by a temporary sensor defect - of the temperature of the coolant at the inlet and the outlet. Again, the difference between the measurements in air and vacuum becomes negligible at flow rates exceeding 30 ml min^{-1}. This means that the heat that is not transported by the fluid in the measurements shown in figure 12.17 b) with a flow rate above 30 ml min^{-1} is not lost via free convection but solely through heat conduction to the NanoPort connectors, Pt100 resistors and through thermal radiation.

The transported heat q_r can be used to calculate the thermal resistance R. The thermal resistance R (see equation 12.2) helps to make the differences between measurements with and without heat transfer to the ambient visible. The measurements are shown in figure 12.22. The measurements performed in air and the measurements performed in a vacuum are separated. The losses during both measurements differ by the heat transfer to the surrounding air. All other losses due to radiation or heat flow through the NanoPort connectors and Pt100 resistors are the same. The amount of heat transferred to the surrounding air depends on the temperature difference between the device and the ambient air, but in this case it can be said that the effect is very small. The maximum temperature measured by the Pt100 resistors was 34.52 °C and the ambient air temperature approximately 21 °C.

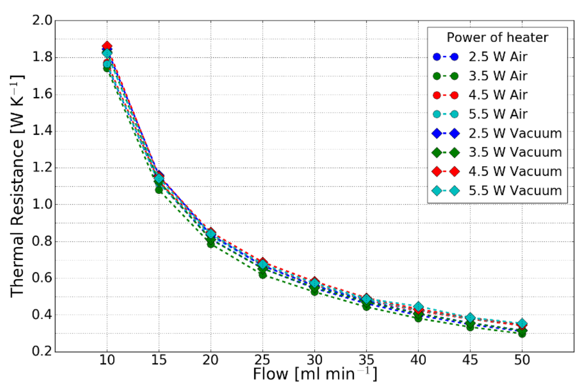

Figure 12.22: Thermal resistance R for heat fluxes of 30.8 mW cm^{-2} to 67.8 mW cm^{-2}, measured in air and in a vacuum.

The presented measurements show that the decision whether measurements should be performed in a vacuum or not to eliminate the effect of free convection to the environment depends on the possibility to adapt the ambient temperature to the one of the device under test.

12.2.4 Custom heater on a cut wafer

To investigate the influence of a surplus of not actively cooled material surrounding the micro-channel structure an eutectic bonded prototype (sample D) was prepared with the wafer cut to the dimensions of the micro-channel array as shown in figure 12.23.

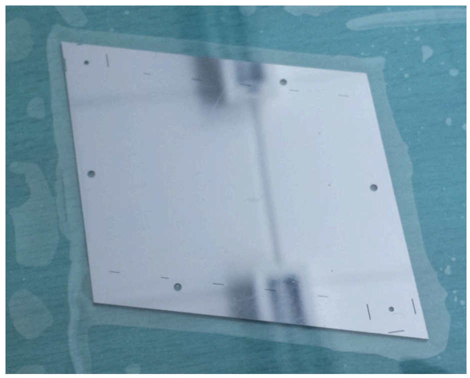

Figure 12.23: Picture of the micro-channel embedded wafer cut to the dimensions of the channel structure.

A custom heater was build with the same dimensions as the cut wafer based on a frame which was produced by additive manufacturing [99] to hold a Cu-Ni resistance wire [100] in place. Two opposite sides of the frame were equipped with holders to tauten the wire between opposite pins. After the wire was wrapped around each holder, the frame was filled with a liquid rubber [101]. The rubber was cured and the borders of the frame designed to capture the liquid rubber were cut off. A picture of the completed heater is shown in figure 12.24.
The heater was glued to the cut wafer with the same instant adhesive used for the Pt100 resistors. The total resistance of the wire embedded in the heater was 24.4 Ω. Measurements to see the overall temperature distribution with the thermal camera were performed to compare with the simulation.

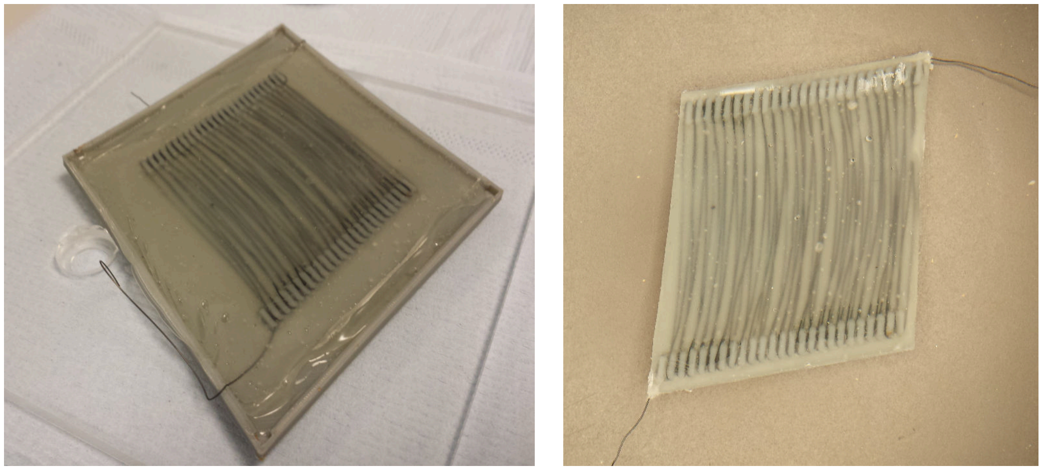

(a) (b)

Figure 12.24: Picture of the custom heater before a) and after cutting b) to the dimensions of the prototype.

An infrared picture of the eutectic bonded cut sample D with the custom heater set to 2.5 W is shown in figure 12.25 side by side with the results of the simulation. In the simulation, the 2.5 W are resulting in a heat flow of around $75.53\,\mathrm{mW\,cm^{-2}}$ for a heater surface area of around $33.1\,\mathrm{cm^2}$. It is visible that without the heat deposited in the surplus of silicon especially on the right and left of the parallel channels, the cooling becomes more efficient at the outer borders of the channel structure.
The pictures taken with the thermal camera can be used to make a qualitative evaluation, but with different heaters and not exactly the same heat flow, a detailed comparison between the full wafer and the cut wafer is not possible.
Trimming the wafer to the size of the micro-channel layout can be seen as a step towards a more realistic setup, in which a layout tailored to a certain sensor must be cut to the channel array dimensions to reduce the material as much as possible.

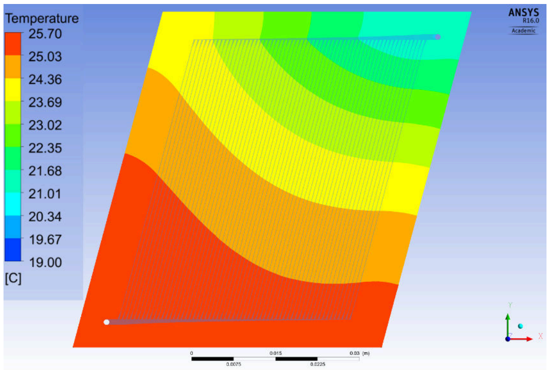

(a) Simulation with a flow rate of 10 ml min^{-1}

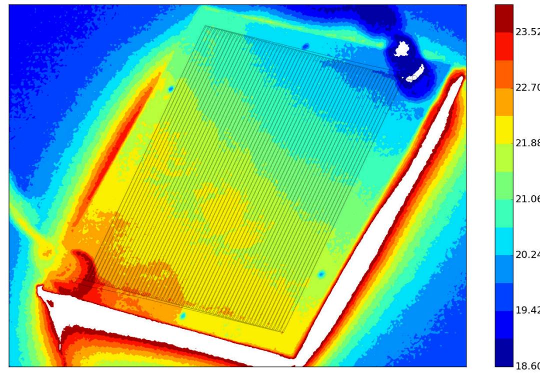

(b) Experiment with a flow rate of 10 ml min^{-1}

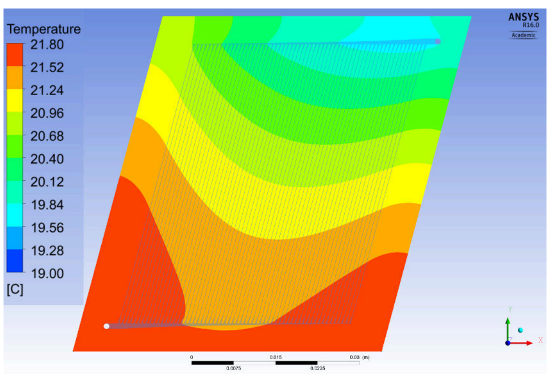

(c) Simulation with a flow rate of 30 ml min^{-1}

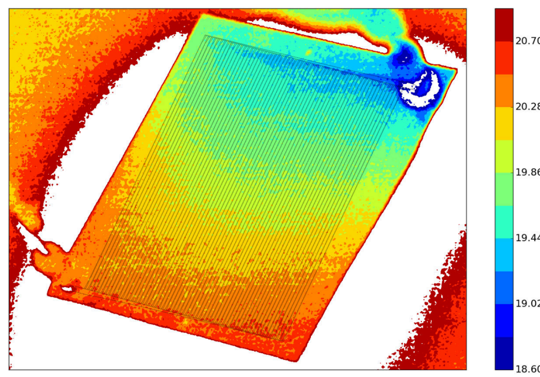

(d) Experiment with a flow rate of 30 ml min^{-1}

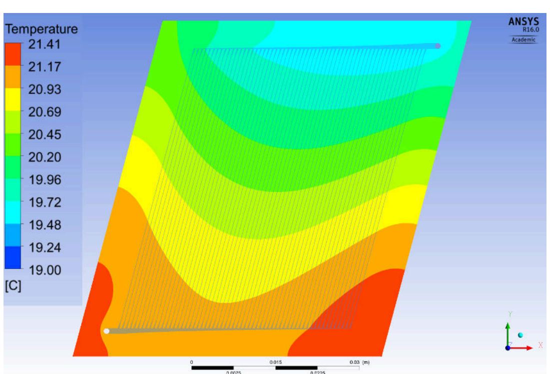

(e) Simulation with a flow rate of 50 ml min^{-1}

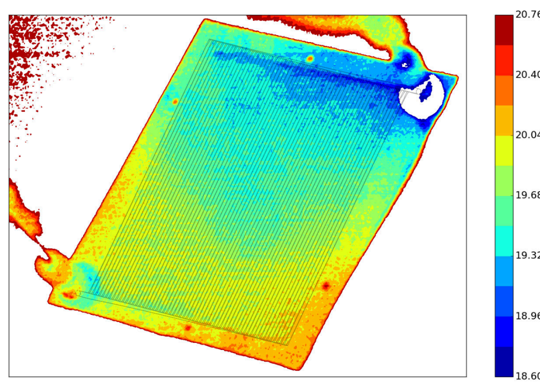

(f) Experiment with a flow rate of 50 ml min^{-1}

Figure 12.25: The results of the simulation a) and the experiment b) obtained with the heater set to 2.5 W and a flow rate of 10 ml min^{-1}.

Chapter 13

Conclusion

This work presents an investigation of micro-channel cooling for silicon sensors at DESY and IMB-CNM. The initial aim was to develop a prototype for large area cooling with small temperature gradients across the actively cooled area. Thus, the work concentrates on a few specific desired characteristics of such a micro-channel device, which is required to feature a homogeneous flow distribution and be able to cool an area comparable to a 4 inch wafer. Moreover, it should be capable of unfolding its full cooling potential, which means that the channel structure must be designed in a way that reaches the necessary cooling power without putting the device at risk of breaking due to excessive pressures.

One big challenge was the design and construction of a test stand. A very flexible and modular test stand was constructed, including devices for precise flow and pressure tests. Depending on the aim of the measurements, a vacuum vessel, a mount for a thermal camera or a confocal microscope was integrated. The different setups showed a very robust and stable performance during the various measurements.

The behavior of the prototype had to be estimated before manufacturing started, thus the design of the channel structure was fixed after first singlephase and multiphase simulations with OpenFoam showed a homogeneous velocity distribution across the channel array. The first prototype samples were silicon-Pyrex fabricated by anodic bonding and proved to be very practical to investigate the flow through the Pyrex cover.

Detailed flow studies were performed with fluorescent tracer beads, observed via a confocal microscope. The previous tilting of the layout by 15° was not enough to prevent a flow separation that triggered a recirculating flow. This behavior was also investigated in a detailed simulation with CFX, which showed a very good agreement with the experimentally obtained results.

The thermal studies revealed the prototype unfolding cooling potential at a satisfactory flow rate of $50\,\mathrm{ml\,min^{-1}}$ with a pressure drop of 15 bar without putting it at risk of breaking due to excessive pressure. The good performance was confirmed by measurements with thermal cameras and with thermal resistors glued across the channel layout with a heater attached to the wafer with the same

diameter.
Tests were performed with anodic bonded samples and eutectic bonded silicon-silicon samples, uncovering different cooling behavior due to different material properties but also due to malfunctioning prototypes. The maximum temperature difference across the channel array on a 4 inch anodic bonded sample wafer was kept below 4 °C at a flow rate of 50 ml min^{-1}.
Characteristic properties such as the heat removed by the coolant and the thermal resistance were obtained with the latter one reaching values around 0.1 °C W^{-1} through measuring the coolant temperature at the inlet and outlet of the micro-channel structure. Utilizing Pt100 thermal resistors made measurements in air and in a vacuum possible to unveil the difference caused by free convection, which is increasing with the power rate of the heater and decreasing with the flow rate. The results clearly show that the effect of free convection is increasing with the absolute temperature of the sample and the resulting difference between ambient and prototype temperature.
To avoid the influence of surplus silicon on the cooling performance, a wafer was cut to the channel structure and was subsequently inspected using a thermal camera. A partly 3d printed heater was manufactured in-house to maintain a homogeneous heat flow through the trimmed micro-channel sample. The successful development of a custom heater helped to provide a homogeneous heat dissipation across a prototype with non-standardized dimensions. A good the agreement between the experimentally obtained temperature distribution with a thermal camera and the simulation was observed.
Once tuned with the experimental results the simulation could be used to classify if a sample is malfunctioning, as it was the case in this work for the eutectic bonded sample C that was compared to the anodic bonded sample A. The simulation can be modified to make predictions about the behavior or prototypes operated with different coolants, other channel geometries or different channel array layouts. In this way the design of the prototype can be optimized in the simulation before being produced to save time and money compared to the process of producing many different test design proposals.

It has been shown that the prototype used here is capable of homogeneously cooling a large area of 25 cm^2. However a number of requirements for the usage in a real detector still have to be considered. The pressure drop of the micro-channel device of around 15 bar at a flow rate of 50 ml min^{-1} is too high to operate the device in series with a critical destructive pressure limit of 30 bar. A parallel connection in detectors with many modules would add a significant amount of material due to tubings, although it could be minimized by using a light radiation hard material.
Moreover, the regions of the detector where silicon sensors are used are typically not very spacious, which makes a connection from the top or bottom of the sensor like in this work hard to realize. Saving material also means using as little silicon as possible for constructing a micro-channel embedded sensor, as this represents the main mass contribution to a silicon based detector. A way to do so would be the direct bonding of the silicon with etched channels to the sensor, which makes the production a lot more challenging than bonding a closed micro-channel device to the sensor.

Bibliography

[1] D.B. Tuckerman and R.F.W. Pease. High-performance heat sinking for VLSI. *IEEE Electron Device Letters*, 2(5):126–129, 1981.

[2] G. Romagnoli, D.A. Feito, B. Brunel, A. Catinaccio, J. Degrange, A. Mapelli, M. Morel, J. Noel, and P. Petagna. Silicon micro-fluidic cooling for NA62 GTK pixel detectors. *Microelectronic Engineering*, 145:133–137, 2015.

[3] A. Francescon, G. Romagnoli, A. Mapelli, P. Petagna, C. Gargiulo, L. Musa, J.R. Thome, and D. Del Col. Development of interconnected silicon micro-evaporators for the on-detector electronics cooling of the future ITS detector in the ALICE experiment at LHC. *Applied Thermal Engineering*, 93:1367–1376, 2015.

[4] A. Nomerotski, J. Buytart, P. Collins, R. Dumps, E. Greening, M. John, A. Mapelli, A. Leflat, Y. Li, G. Romagnoli, and B. Verlaat. Evaporative CO_2 cooling using microchannels etched in silicon for the future LHCb vertex detector module prototype with microchannel cooling. *Journal of Instrumentation*, 8:1–12, 2013.

[5] C.P. Burgess and G.D. Moore. *The Standard Model: A Primer*. Cambridge University Press, 2007.

[6] D.J. Griffiths. *Introduction to Elementary Particles*. Wiley, 2008.

[7] W.N. Cottingham and D.A. Greenwood. *An introduction to the standard model of particle physics*, volume 1. Cambridge Univ. Press, 2 edition, 2007.

[8] K.A. Olive and (Particle Data Group). Review of Particle Physics. *Chinese Physics C*, 38(9):090001, 2014.

[9] P.W. Higgs. Broken symmetries, massless particles and gauge fields. *Physical Letters*, 12(2):132–133, 1964.

[10] F. Englert and R. Brout. Broken Symmetry and the Mass of Gauge Vector Mesons. *Physical Review Letters*, 13(9):321–323, 1964.

[11] J.W. Rohlf. *Modern Physics from alpha to Z0*. Wiley, 1994.

[12] T. Schörner-Sadenius. *The Large Hadron Collider: Harvest of Run 1*. Springer, 2015.

[13] ATLAS Collaboration and CMS Collaboration. Measurements of the Higgs boson production and decay rates and constraints on its couplings from a combined ATLAS and CMS analysis of the LHC pp collision data at $\sqrt{s} = 7$ and 8 TeV. *Journal of High Energy Physics*, 2016(8):45, 2016.

[14] K. Garrett and G. Duda. Dark Matter: A Primer. *Advances in Astronomy*, 6:1–27, 2011.

[15] L. Canetti, M. Drewes, and M. Shaposhnikov. Matter and Antimatter in the Universe. *New Journal of Physics*, 14:1–20, 2012.

[16] S.M. Sze and K.K. Ng. *Physics of Semiconductor Devices*. Springer, 3 edition, 2006.

[17] M. Moll. *Radiation Damage in Silicon Particle Detectors - microscopic defects and macroscopic properties*. PhD thesis, Hamburg University, 1999.

[18] L. Evans and P. Bryant. LHC Machine. *Journal of Instrumentation*, 3(08):S08001, 2008.

[19] O.S. Brüning, P. Collier, P. Lebrun, S. Myers, R. Ostojic, J. Poole, and P. Proudlock. *LHC Design Report*. CERN Yellow Reports: Monographs. CERN, 2004.

[20] D. Froidevaux and P. Sphicas. General-Purpose Detectors for the Large Hadron Collider. *Annual Review of Nuclear and Particle Science*, 56(1):375–440, 2006.

[21] ATLAS Collaboration. *ATLAS inner detector: Technical Design Report, 1*. Technical Design Report ATLAS. CERN, 1997.

[22] ATLAS Collaboration. The ATLAS Experiment at the CERN Large Hadron Collider. *Journal Of Instrumentation*, 3(08):S08003, 2008.

[23] The ATLAS Collaboration. The ATLAS experiment at the CERN Large Hadron Collider. *JINST 3 S08003*, 2008.

[24] S.M. Gibson. Monitoring radiation damage in the ATLAS Silicon Tracker. *ATL-INDET-PROC-2011-014, ATL-COM-INDET-2011-073*, 2011.

[25] G. Gagliardi. The ATLAS Pixel Detector: A hundred million channels vertex detector for LHC. *Nuclear Instruments and Methods in Physics Research Section A: Accelerators, Spectrometers, Detectors and Associated Equipment*, 546(1-2):67–71, 2005.

[26] B. Mandelli. The Pixel Detector of the ATLAS Experiment for the Run 2 at the Large Hadron Collider. *Nuclear and Particle Physics Proceedings*, 273-275:1166–1172, 2016.

[27] F. Guescini. The Insertable B-Layer of the ATLAS experiment for the Run-2 at the Large Hadron Collider. *Nuclear Instruments and Methods in Physics Research Section A: Accelerators, Spectrometers, Detectors and Associated Equipment*, 796:60–63, 2015.

[28] ATLAS Collaboration. The barrel modules of the ATLAS semiconductor tracker. *Nuclear Instruments and Methods in Physics Research Section A: Accelerators, Spectrometers, Detectors and Associated Equipment*, 568(2):642–671, 2006.

[29] L. Feld. Detector modules for the ATLAS SCT endcaps. *Nuclear Instruments and Methods in Physics Research Section A: Accelerators, Spectrometers, Detectors and Associated Equipment*, 511(1-2):183–186, 2003.

[30] ATLAS SCT Community. The barrel modules of the ATLAS semiconductor tracker. *Nuclear Instruments and Methods in Physics Research Section A: Accelerators, Spectrometers, Detectors and Associated Equipment*, pages 1–41, 2006.

[31] B. Mindur. ATLAS Transition Radiation Tracker (TRT): Straw tubes for tracking and particle identification at the Large Hadron Collider. *Nuclear Instruments and Methods in Physics Research, Section A: Accelerators, Spectrometers, Detectors and Associated Equipment*, 845:257–261, 2017.

[32] ATLAS Electromagnetic Liquid-Argon Calorimeter Group. Construction, assembly and test of the ATLAS electromagnetic barrel calorimeter. *Nuclear Instruments and Methods in Physics Research, Section A: Accelerators, Spectrometers, Detectors and Associated Equipment*, 558:388–418, 2006.

[33] ATLAS Electromagnetic Liquid-Argon Calorimeter Group. Construction, assembly and tests of the ATLAS electromagnetic end-cap calorimeters. *Journal of Instrumentation*, 3(06):P06002, 2008.

[34] T. Barillari. The ATLAS liquid argon hadronic end-cap calorimeter: construction and selected beam test results. *Nuclear Physics B - Proceedings Supplements*, 145:102–105, 2006.

[35] L. Heelan. Performance of the ATLAS forward calorimeter. *Journal of Physics: Conference Series*, 160:012058, 2009.

[36] ATLAS Hadronic Tile Calorimeter Group. Mechanical construction and installation of the ATLAS tile calorimeter. *Journal of Instrumentation*, 8(11):P01005, 2013.

[37] S. Palestini. The muon spectrometer of the ATLAS experiment. *Nuclear Physics B - Proceedings Supplements*, 125:337–345, 2003.

[38] G. Cattani and the RPC group. The Resistive Plate Chambers of the ATLAS experiment: performance studies. *Journal of Physics: Conference Series*, 280(1):12001, 2011.

[39] Y. Nakahama. The ATLAS Trigger System: Ready for Run-2. *Journal of Physics: Conference Series*, 664(8):082037, 2015.

[40] L. Rossi and O. Brüning. High Luminosity Large Hadron Collider A description for the European Strategy Preparatory Group. *CERN-ATS-2012-236*, 2012.

[41] ATLAS Collaboration. Letter of Intent for the Phase-II Upgrade of the ATLAS Experiment. *CERN-LHCC 2012-022*, 2012.

[42] ATLAS Collaboration. Technical Design Report for the ATLAS ITK - Strips Detector. 145, 2016.

[43] The Geant4 Collaboration (S. Agostinelli et al.). Geant4 - A Simulation Toolkit. *Nuclear Instruments and Methods in Physics Research*, pages 250–303, 2003.

[44] ATLAS Collaboration. Operation and performance of the ATLAS semiconductor tracker. *JINST 9 P08009*, pages 1–74, 2014.

[45] ATLAS Collaboration. The ATLAS Simulation Infrastructure. *arXiv:1005.4568v1*, pages 1–53, 2010.

[46] ATLAS Computing Group. ATLAS Computing Technical Design Report. *CERN-LHCC-2005-022*, 2005.

[47] M. Filipuzzi. *Measurements of fiducial differential cross sections for Higgs boson production in the diphoton decay channel at $\sqrt{s}$ = 8 TeV with ATLAS*. PhD thesis, Hamburg University, 2016.

[48] T. Lari. Lorentz angle variation with electric field for ATLAS silicon detectors. *ATL-INDET-2001-004*, pages 1–6, 2001.

[49] M. Filipuzzi, K. Tackmann, P. Vankov. Study of charge trapping in the ATLAS SCT Digitization. *ATL-COM-INDET-2014-004*, pages 1–15, 2014.

[50] P. Dervan, J. Vosenbeld, T. Kondo. Evolution of V_d and I_{leak} of the ATLAS barrel SCT. SCT Digitization Task Force, 2009.

[51] T. Kondo. Study of crosstalk in the SCT digitization: Effects on <cluster size>min. SCT Digitization Task Force, 2010.

[52] Szymon G. Model of the SCT detectors and electronics for the ATLAS simulation using Geant4. *ATL-SOFT-2001-005*, pages 1–21, 2001.

[53] I. Antcheva, M. Ballintijn, B. Bellenot, M. Biskup, R. Brun, N. Buncic, Ph. Canal, D. Casadei, O. Couet, V. Fine, L. Franco, G. Ganis, A. Gheata, D. Gonzalez Maline, M. Goto, J. Iwaszkiewicz, A. Kreshuk, D. Marcos Segura, R. Maunder, L. Moneta, A. Naumann, E. Offermann, V. Onuchin, S. Panacek, F. Rademakers, P. Russo, and M. Tadel. ROOT - A C++ framework for petabyte data storage, statistical analysis and visualization. *Computer Physics Communications*, 180(12):2499–2512, 2009.

[54] B.R. Munson, D.F. Young, and T.H. Okiishi. *Fundamentals of fluid mechanics*, volume 16. Wiley, 4 edition, 2001.

[55] H. Bruus. *Theoretical microfluidics*, volume 18 of *Oxford Master Series in Condensed Matter Physics*. Oxford University Press, 2008.

[56] F.P. Incropera, D.P. DeWitt, T.L. Bergman, and A.S. Lavine. *Fundamentals of Heat and Mass Transfer*. Wiley, 2007.

[57] Alcatel 601-E DRIE (Deep Reactive Ion Etcher). `http://research.engineering.ucdavis.edu/cnm2/wp-content/uploads/sites/11/2013/08/AlcatelDRIE.pdf`, 2017.

[58] Bosh process: method of anisotropically etching silicon). `http://www.freepatentsonline.com/5501893.html`, 2017.

[59] F. Laermer and A. Schilp. Method of anisotropically etching silicon, March 26 1996. US Patent 5,501,893.

[60] A.A. Ayon, R. Braff, C.C. Lin, H. Sawin, and M.A. Schmidt. Characterization of a time multiplexed inductively coupled plasma etcher. *J. Electrochem. Soc.*, 146:pp 339, 1999.

[61] W. Kern. The Evolution of Silicon Wafer Cleaning Technology. *Journal of The Electrochemical Society*, 137(6):1887 – 1892, 1990.

[62] M.J. Madou. *Fundamentals of microfabrication: the science of miniaturization*. CRC Press, 2 edition, 2002.

[63] K.M. Knowles and A.T.J. Van Helvoort. Anodic bonding. *International Materials Reviews*, 51:pp. 273–311, 2006.

[64] OpenCFD. *OpenFOAM - The Open Source CFD Toolbox - User's Guide*. OpenCFD Ltd., 3.0 edition, 2015.

[65] CFX high-performance computational fluid dynamics software tool. `http://www.ansys.com/products/Fluids/ANSYS-CFX`, 2016.

[66] ANSYS FEA software. `http://www.ansys.com`, 2016.

[67] ANSYS Inc. ANSYS CFX-Solver Theory Guide. *ANSYS CFX 15.0*, 2013.

[68] F.R. Menter. Turbulence Modeling for Engineering Flows. *A Technical Paper from ANSYS, Inc*, 2011.

[69] D.C. Wilcox. *Turbulence Modeling for CFD*. DCW Industries, 3 edition, 2006.

[70] C. Rumsey and T. Beutner. Introduction: Computational Fluid Dynamics Validation for Synthetic Jets. *AIAA Journal*, 44(2):193–193, 2006.

[71] C.W. Hirt and B.D. Nichols. Volume of fluid (VOF) method for the dynamics of free boundaries. *Journal of Computational Physics*, 39(1):201–225, 1981.

[72] C. Geuzaine and J.-F. Remacle. Gmsh: a three-dimensional finite element mesh generator with built-in pre- and post-processing facilities. *International Journal for Numerical Methods in Engineering*, 79(11):1309–1331, 2016.

[73] H.M. Wyss, D.L. Blair, J.F. Morris, H. Stone, and D. Weitz. Mechanism for clogging of microchannels. *Physical Review E - Statistical, Nonlinear, and Soft Matter Physics*, 74(6):061402, 2006.

[74] Y. Cagnon. Vortex Simulation of Laminar Recirculating Flow. *Journal of Computational Physics*, 68:346–377, 1987.

[75] 3M HFE 7100. http://solutions.3mdeutschland.de/wps/portal/3M/de_DE/Novec/Home/Product_Information/Products/?PC_Z7_RJH9U5230OLLB0I4HB8HRT3OC0000000_nid=H50MQNF12BbeQQBXSJ1LVVgl, 2016.

[76] ECOM Iota 300 HPLC pump. http://www.ecomsro.com/FS/0001-Ecom/files/products/Info-Iota50-100-300-pump-en.pdf, 2016.

[77] Alfa Laval Heat Exchanger. http://www.alfalaval.com, 2016.

[78] Huber Petite Fleur w. http://www.huber-online.com/de/product_datasheet.aspx?no=1030.0003.01, 2016.

[79] Bronkhorst miniCori Flow. http://www.bronkhorst-nord.de/de/produkte/coriolis_messer_und_-regler/mini_cori-flow/massendurchflussmesser/, 2016.

[80] Swagelok pressure transducer. https://www.swagelok.com/en/product/Measurement-Devices/Pressure-Transducers, 2016.

[81] Swagelok filter. https://www.swagelok.de/de-DE/product/Filters/Particulate-Filters-Inline-and-Tee-Type, 2016.

[82] Swagelok valve. https://www.swagelok.com/en/product/Valves, 2016.

[83] Infrared VarioCAM HD. http://www.infratec.de/de/thermografie/waermebildkameras.html, 2016.

[84] Vacom vacuum components. http://www.vacom.de, 2016.

[85] Platinum Sensing Resistors - Thin Film Pt100. http://www.farnell.com/datasheets/49129.pdf, 2016.

[86] Arduino UNO board. http://www.arduino.cc, 2016.

[87] Keithley 2700 multimeter. http://docs-europe.electrocomponents.com/webdocs/10ec/0900766b810ec7e7.pdf, 2016.

[88] Keithley 7700 Dual 1X10 Multiplexer. http://www.tek.com/sites/tek.com/files/media/media/resources/IntegraModules.pdf, 2016.

[89] Hameg HM8143 programmable power supply. https://www.rohde-schwarz.com/de/produkt/hm8143-produkt-startseite_63493-43458.html, 2016.

[90] ISO. *ISO/IEC 14882:2011 Information technology — Programming languages — C++*. International Organization for Standardization, 2012.

[91] QT cross-platform application framework. https://www.qt.io/, 2016.

[92] NanoPort Assemblies. https://www.idex-hs.com/fluidics/fluidic-connections.html, 2016.

[93] Hydraulic hand test pump Type P 700.2. https://www.sika.net/services/downloads/send/5-kataloge-test-und-kalibriertechnik/20-kapitel-pr%C3%BCfpumpen-und-digitalmanometer.html, 2017.

[94] Weicon Contact VA 100. http://www.weicon.de/einsatzgebiete/elektroinstallation/kleben-und-abdichten/144/contact-va-100?c=10149, 2009.

[95] Self adhesive heatermat, 8W 12V 100mm dia. http://docs-europe.electrocomponents.com/webdocs/1502/0900766b81502465.pdf, 2016.

[96] G. Cox. Biological confocal microscopy. *Materials Today*, 5(3):34 – 41, 2002.

[97] Fluoro-Max Dyed Green Aqueous Fluorescent Particles. https://www.thermofisher.com/order/catalog/product/G0100, 2016.

[98] Inverted research microscope Nikon eclipse Ti. https://www.nikoninstruments.com/en_DE/Products/Inverted-Microscopes/Eclipse-Ti-E, 2016.

[99] Zortrax M200 - 3d LPD Printer. https://zortrax.com/printers/zortrax-m200/, 2016.

[100] Resistance Wire - RD 100/0.3. http://www.block.eu/de_DE/products/720977.htm, 2016.

[101] Mibenco liquid rubber - pure. http://mibenco.com/fin/liquid-rubber-pure, 2016.